GCA-TR-67-15-N

NASA CR-65993

EARTH-BASED LUNAR ATMOSPHERE INVESTIGATION

F. F. MARMO A. ENGELMAN H. A. MIRANDA, JR. E. MANRING

Bedford, Massachusetts

FINAL REPORT
NAS9-5589

PREPARED FOR
NATIONAL AERONAUTICS AND SPACE ADMINISTRATION
MANNED SPACECRAFT CENTER
HOUSTON, TEXAS

AUGUST 1967

GCA-TR-67-15-N

EARTH-BASED LUNAR ATMOSPHERE INVESTIGATION

F.F. Marmo
A. Engelman
H.A. Miranda, Jr.
E. Manring

GCA CORPORATION
GCA TECHNOLOGY DIVISION
Bedford, Massachusetts

FINAL REPORT

Contract No. NAS9-5589

August 1967

Prepared for

NATIONAL AERONAUTICS AND SPACE ADMINISTRATION
Manned Spacecraft Center
Houston, Texas

TABLE OF CONTENTS

I. INTRODUCTION

This document represents the Final Report under Contract No. NAS9-5589, and includes a discussion of the instrumentation designed and fabricated under the program as well as the results obtained from the experimental measurement effort conducted at the Sacramento Peak Observatory. The major purpose of the program was the spectrometric detection and identification of atomic and/or ionic lunar atmospheric constituents in the visible spectral region. The extremely sensitive technique employed in the experimental program involved observation of signature resonance radiations emitted from solar-illuminated atomic and/or ionic constituents in the lunar atmosphere. To accomplish these aims, the specially designed Fastie-Ebert type spectrometer was coupled to the Sacramento Peak coronagraph so that the observations of the pertinent sector of the lunar atmosphere residing above the occulted Coude lunar image could be performed. On this basis, new and meaningful upper limit surface number density values were established for the constituents Na, Ca, and Ca^+. The subject matter of the present report has been subdivided into four convenient discussion categories as outlined below.

The general scientific rationale involved in establishing the feasibility of performing the field experimental investigation is discussed in Section II. In this context, a careful theoretical analysis is presented upon which were predicated the major pertinent instrumental parametric design features of the Fastie-Ebert type spectrometer. The complex instrumentation design, development, fabrication, and calibration aspects of the program are described in detail in Section III including discussions of the major auxiliary electronic and optical subsystems. Sections IV and V of the present report are concerned specifically with the performance of the field experimental program. In the former section, there are included descriptions of the instrumentation field reassembly procedure, coupling of the Fastie-Ebert type spectrometer to the coronagraph, and the development and execution of a suitable guidance scheme. Additionally, the experimental measurement parameters are identified and employed in the definition of the field data acquisition procedure. Finally, the data analysis interpretation is discussed in Section V where it is demonstrated that reliable upper limit surface number density values of less than $100/cm^3$ were established for the three species cases investigated.

II. THEORETICAL SIGNAL AND BACKGROUND CONSIDERATIONS

The present section discusses the analytical results derived from detailed examinations of expected signal and background levels pertinent to the design, performance, and evaluation of feasibility of the field experiment. In the signal level analysis, reliable estimates are derived for the solar resonance scattering probability per atom (or ion), P, for seventeen selected species whose first resonance scattering levels reside in the visible portion of the spectrum. Two sets of expected signal brightness values, Φ, were calculated predicated on the validity of two independent lunar atmosphere models. Estimated background brightness values, B_i, were calculated for contributions due to zodiacal, stellar, and air glow sources. Additionally, estimates were obtained for the background contribution due to the scattering of lunar radiation by the earth's atmosphere combined with instrumental scatter due to the optical instrumentation involved. It is demonstrated that this latter source is, in general, the dominant source encountered in the performance of the field experiment described in Section IV.

Calculations of Estimated Signal Brightness Values, Φ

The present section discusses the calculations performed to obtain estimates of the expected signal brightness levels for seventeen specific species selected on the basis of a previous analysis [1].* The calculations are straightforward although a number of parameters are involved in the analysis. Basically, the signal brightness is due to resonance scattering of solar radiation by a given species so that two of the fundamental parameters involved are: (1) the individual resonance scattering efficiency per atom (or ion), α, and (2) the incident solar flux, $F_s(\lambda)$, appropriate to the particular species resonance wavelength. The product of these parameters, then, represents the solar resonance scattering probability per atom (or ion), P. The derived P-values are subsequently convolved with lunar atmospheric models which define the abundance, constituency, and distribution of several gaseous species resident in the lunar atmosphere. The results are given in terms of Φ-values which pertain to solar illuminated species resident at a mean altitude of 100 kilometers above the lunar surface.

Resonance Scattering Efficiencies. Resonance scattering efficiencies, α, can be calculated from the following equation:

$$\alpha = \frac{\pi e^2}{mc^2} \frac{gf}{g_1} \lambda_r^2 \qquad (1)$$

* Numbers in [ ] denote reference numbers.

where

e = unit charge
m = electron mass
λ_r = wavelength of the resonance transition
g_1 = statistical weight of the ground level
gf = oscillator strength of the particular transition in which the weight of the upper state is incorporated.

A literature survey [2,3] has shown that the gf-values for the selected constituents had not been accurately determined and, additionally, no critical evaluation of the pertinent experimental and theoretical data had been performed. Accurate knowledge of the individual α-values is a basic requirement for the quantitative interpretation of the results obtained in the experimental program. For this reason the required critical analysis was performed on the basis of a detailed evaluation of the data given from the large number of sources involved. For each of the selected species the pertinent transition is first defined and then the determination of its oscillator strength is discussed. On the basis of the evaluation technique involved, a recommended value is selected for each transition which is employed in the present analysis. Of the seventeen selected transitions no reliable data were available in three cases so that the results are given for fourteen species. Finally, it is important to point out that one of the major aims of this study phase was to attach meaningful error estimates to the individual gf-values quoted. A brief survey of the analysis involved is given below along with final tabulated results for the fourteen species involved. A complete detailed discussion of the evaluation technique employed is given in Appendix A.

Na I λ5890Å. The value presented by Kvater [4] has been revised by Penkin [5] on the basis of new vapor-pressure data obtained by Nesmeyanov [6]. Kvater's value of 1.65 thus becomes 1.39, a reduction of 16 percent, indicative of the magnitude of systematic errors which may occur in the reduction of experimental data. This result is within 10 percent of the result of Penkin [5] using the Hook method with total absorption. Stephenson [7] employed the magnetic rotation method of Weingeroff [8] to measure the lifetime although the accuracy to be expected from the theory behind this technique is difficult to assess. A number of Hartree-Fock results are also available, yielding a variety of results. The value of Chapman, Clarke and Aller [9] is obtained by the standard method, but differs by 14 percent from the value of Bersuker [10] who allowed for the time-dependent perturbation due to the polarization of the core during the transition. The Bates-Damgaard result of Griem [11] is slightly smaller than that listed by Bates and Damgaard [12] due to the use of more recent ionization potential data while the work of Houziaux and Sadoine [13] appears to be in error.

Author	gf-Value	Method	Ref.
Kvater	1.39	Hook	[4]
Penkin (Revised)			
Penkin	1.53*	Hook with Total Absorption	[5]
Stephenson	1.30	Lifetime by Magnetic Rotation	[7]
Fock	1.38	Hartree-Fock (Length)	[14]
Biermann	1.32	Hartree-Fock (Length)	[15]
Chapman, et al.	1.41	Hartree-Fock (Length)	[9]
Bersuker	1.62	Hartree-Fock (Length) with Core Polarization	[10]
Griem	1.25	Bates-Damgaard	[11]
Anderson and Zilitis	1.30	Petrashen-Abarenkov	[16]
Stewart and Rotenberg	1.30	Scaled Thomas-Fermi	[17]

*Recommended Value

Ca II λ3934Å. This is one of the few lines of an ion specie spectrum for which an accurate experimental determination is available although the accuracy depends on the applicability of the Saha equation. The initial value of Ostrovskii and Penkin [18] was later revised by Penkin [5] presumably on the basis of new vapor-pressure data. Similar Hartree-Fock calculations have been performed by both Trefftz and Biermann [19] and Douglas and Garstang [20] who included the effect of static core polarization [21]. Douglas and Garstang list a variety of values from different versions of the Hartree-Fock scheme, which are reproduced below.

Author	gf-Value	Method	Ref.
Ostrovskii and Penkin	1.66*	Hook	[18]
Penkin (Revised)			[5]
Trefftz and Biermann	1.44	Hartree-Fock (Length); Polarization	[19]
	1.36	Hartree-Fock (Velocity); Polarization	
Douglas and Garstang	1.44	Hartree-Fock (Length); Polarization	[20]
	1.35	Hartree-Fock (Velocity); Polarization	
	1.56	Hartree-Fock (Length)	
	1.20	Hartree-Fock (Velocity)	
	1.85	Hartree (Length)	
Zwaan	1.46	WKB	[22]
Griem	1.33	Bates-Damgaard	[11]

*Recommended Value

Sc I λ3907Å. No reliable data available.

V I λ3855Å. No reliable data available; the transition is forbidden (two-electron jump).

Sr I λ4607Å. The most accurate measurement is that of Ostrovskii and Penkin [23] by the Hook method with total absorption. The lifetime measurement of Lurio, de Zafra and Goshen [24] should constitute an upper bound, since the possibility of decay from the upper level to the 5s 4d ($^1D_2$) level (an allowed transition) is opened. Strontium is too complicated an atom for the Bates-Damgaard method to yield reliable results.

Author	gf-Value	Method	Ref.
Ostrovskii and Penkin	1.54*	Hook-Total Absorption	[23]
Lurio, et al.	< 1.92	Lifetime (Level-Crossing)	[24]
Bates and Damgaard	1.82	Bates-Damgaard	[12]
Garstang	1.90	Bates-Damgaard in Intermediate Coupling	[25]

*Recommended Value

Ti I λ5014Å. No reliable data available.

Ca I λ4227Å. The most accurate measurement is that of Ostrovskii and Penkin [23]. The lifetime measurement of Lurio, et al. [24] yields an upper bound, due to neglect of the 4s 4p ($^1P_1^o$) - 4s 3d ($^1D_2$) transition. The Hartree-Fock calculations of Trefftz [26] which allow for configuration interaction and polarization reveal the importance of these effects (especially the former) on comparison with the straight Hartree-Fock calculation of Hartree and Hartree [27]; however, the length and velocity forms are in disappointingly poor agreement. The Bates-Damgaard result [11] is rather large, probably due to insufficient allowance for configuration interaction.

Author	gf-Value	Method	Ref.
Ostrovskii and Penkin	1.49*	Hook-Total Absorption	[23]
Lurio, et al.	< 1.80	Lifetime (Level-Crossing)	[24]
Hartree and Hartree	2.24	Hartree-Fock (Length)	[27]
Trefftz	1.63	Hartree-Fock (Length) with C I and Polarization; Exp. Energy	[26]
	1.31	Hartree-Fock (Velocity)	
Griem	1.83	Bates-Damgaard	[11]

*Recommended Value

Al I λ3944Å. The most accurate measurement is the lifetime determination of Brehm, Demtroder and Osberghaus [28]. The value of Penkin and Shabanova [29] was obtained by placing relative values into an absolute scale by means of a measurement for the λ3961Å line (the other line of the resonance doublet) by Penkin [30]; although the Hook method with total absorption was used, the accuracy claimed is very low (f = 0.15 ± 0.04). The low accuracy is probably due to the use of photography rather than photoelectric techniques in the absorption measurement. The result of Brehm, et al. [28] lies within the limits claimed by Penkin. Configuration interaction is presumably responsible for the surprisingly low Bates-Damgaard value [11]; however, the single configuration Hartree-Fock calculation of Biermann and Lubeck [31] is in good agreement with the experimental results.

Author	gf-Value	Method	Ref.
Penkin and Shabanova	0.30*	Hook	[29]
Brehm, et al.	0.24	Lifetime, Optical Excitation	[28]
Biermann and Lubeck	0.27	Hartree-Fock (Length) with Polarization	[31]
Griem	0.10	Bates-Damgaard	[11]

*Recommended Value

Cr I λ3593Å. Chromium is well known for yielding widely divergent gf-values. The revised value of Penkin [5] is accepted as derived from the Ostrovskii and Penkin [32] value, presumably on the basis of new vapor pressure data.

Author	gf-Value	Method	Ref.
Ostrovskii and Penkin			[32]
Penkin (Revised)	1.89*	Hook	[5]
Lawrence, et al.	1.68	Atomic Beam Absorption	[33]

*Recommended Value

K I λ7665Å. This line is isoelectronic with Ca II λ3934Å. The most reliable result is that of Penkin [5] which is in excellent agreement with the several other values tabulated below.

Author	gf-Value	Method	Ref.
Penkin	1.37*	Hook-Total Absorption	[5]
Stephenson	1.31	Lifetime (Magnetic Rotation)	[7]
Biermann and Lubeck	1.43	Hartree-Fock (Length) with Polarization	[31]
Griem	1.31	Bates-Damgaard	[11]
Anderson and Zilitis	1.39	Petrashen'-Abarenkov	[16]
Stewart and Rotenberg	1.40	Scaled Thomas-Fermi	[17]

*Recommended Value

Y I λ4143Å. The only available result, which is not very accurate, is that due to Goldberg, et al. [34]

Author	gf-Value	Method	Ref.
Goldberg, et al.	2.09*	Bates-Damgaard	[34]

*Recommended Value

Zr I λ6135Å. The only available, and probably inaccurate, result is that due to Manring [35].

Author	gf-Value	Method	Ref.
Manring	1.41*	Bates-Damgaard (extrapolated)	[35]

*Recommended Value

Ba I λ5535Å. The recommended result of Penkin [5] is in excellent agreement with the lifetime measurement of Bucka and Schussler [36] while the Bates-Damgaard [35] result is rather large.

Author	gf-Value	Method	Ref.
Penkin	1.40*	Hook-Total Absorption	[5]
Bucka and Schussler	1.32	Lifetime (Double Resonance)	[36]
Manring	1.92	Bates-Damgaard	[35]

*Recommended Value

Rb I λ7800Å. Penkin [5] has revised the result of Gol'dberg [37], who employed the Hook method, on the basis of the vapor pressure data of Nesmeyanov [6]. The resulting figure is somewhat larger than other available values.

Author	gf-Value	Method	Ref.
Gol'dberg	1.60*	Hook	[37]
Penkin (Revised)			[5]
Stephenson	1.32	Lifetime (Magnetic Rotation)	[7]
Goldberg, et al.	1.35	Bates-Damgaard	[34]
Gol'dberg	1.47	Petrashen-Abarenkov	[37]

*Recommended Value

Mn I λ4031Å. As shown by Allen [38] and Morozova and Startsev [39], gf-values for Mn are in unusually good agreement. Penkin [5] quotes absolute values from Ostrovskii and Penkin [32], q.v. for a discussion of the vapor pressure equation used. Apparently, unlike the gf-values for Cr I as discussed previously, these values have not been revised presumably because no new vapor pressure data has become available. This suggests a rather larger-than-usual uncertainty about this result.

Author	gf-Value	Method	Ref.
Ostrovskii and Penkin	0.34*	Hook	[32]
Bell, et al.	0.36	Atomic Beam Absorption	[40]

*Recommended Value

Co I λ3527Å. The only reliable result is that due to Lawrence, et al. [33]

Author	gf-Value	Method	Ref.
Lawrence, et al.	0.20*	Atomic Beam Absorption	[33]

*Recommended Value

Li I λ6707Å. The two lines of the resonance doublet of lithium are too close together to be resolved in the present experiment. Results for the stronger lines are presented here; gf-values for the two lines are in the ratio 2:1. The various calculated values are in good agreement with each other and with the lifetime measurement of Stephenson [7].

Author	gf-Value	Method	Ref.
Stephenson	0.96*	Lifetime (Magnetic Rotation)	[7]
Ivanova and Ivanova	1.03	Hartree-Fock (Length)	[41]
	1.05	Hartree-Fock (Velocity)	
Weiss	1.02	Hartree-Fock (Length)	[42]
	1.05	Hartree-Fock (Velocity)	
	1.00	Configuration Interaction Calculation (Length)	
	1.03	Configuration Interaction Calculation (Velocity)	
Griem	1.00	Bates-Damgaard	[11]
Stewart and Rotenberg	0.97	Scaled Thomas-Fermi	[17]

*Recommended Value

On the basis of the above discussions, the recommended gf-values and corresponding error estimates are tabulated in Column 4 of Table 1 in order of decreasing values. The resultant resonance scattering efficiencies for the selected individual species are given in Table 2, Column 4.

Solar Flux Estimates. The general features of the solar spectrum as applied to the present problem are illustrated in Figure 1 which includes both the solar continuum and the strong Fraunhofer absorption features for the spectral region λλ3500-8000Å. Marmo, et al. [43] have demonstrated previously that the appropriate solar flux incident on a potential resonance scattering species must necessarily include the role of Fraunhofer absorption

TABLE 1

RECOMMENDED OSCILLATOR STRENGTHS FOR SEVENTEEN IMPORTANT TRANSITIONS

Atom or Ion Species	Transition	Wavelength (Å)	gf-Values
Y I	$4d5s^2a^2D_{3/2} - 4d5s(^1D)5py\,^2D^o_{3/2}$	4143	2.09 ± 25%
Cr I	$3d^5(^6S)4sa^7S_3 - 3d^4 4s(^6D)4py\,^7P^o_3$	3593	1.89 ± 10%
Ca II	$4s^2S_{1/2} - 4p^2P^o_{3/2}$	3934	1.66 ± 15%
Rb I	$5s^2S_{1/2} - 5p^2P^o_{3/2}$	7800	1.60 ± 15%
Sr I	$5s^2\,^1S_o - 5s5p\,^1P^o_1$	4607	1.54 ± 10%
Na I	$3s^2S_{1/2} - 3p^2P^o_{3/2}$	5890	1.53 ± 10%
Ca I	$4s^2\,^1S_o - 4s4p\,^1P^o_1$	4227	1.49 ± 10%
Zr I	$4d^2(^3F)5s^2a^3F_2 - 4d^25s(^4F)5pz\,^3F^o_2$	6135	1.41 ± 25%
Ba I	$6s^2\,^1S_o - 6s6p\,^1P^o_1$	5535	1.40 ± 5%
K I	$4s^2S_{1/2} - 4p^2P^o_{3/2}$	7665	1.37 ± 5%
Li I	$2s^2S_{1/2} - 2p^2P^o_{3/2}$	6707.74	1.03 ± 5%
	$2s^2S_{1/2} - 2p^2P^o_{1/2}$	6707.89	0.51 ± 5%
Mn I	$3d^54s^2a^6S_{5/2} - 3d^54s(^7S)4pz\,^6P^o_{7/2}$	4031	0.34 ± 15%
Aℓ I	$3p^2P^o_{1/2} - 4s^2S_{1/2}$	3944	0.24 ± 10%
Co I	$3d^74s^2a^4F_{9/2} - 3d^74s(^5F)4pz\,^4F^o_{9/2}$	3527	0.20 ± 15%
Ti I	$3d^24s^2a^3F_2 - 3d^24s(^2F)4pz\,^3D^o_1$	5014	No data
V I	$3d^34s^2a^4F_{3/2} - 3d^4(^5D)4py\,^4F^o_{3/2}$	3855	No data
Sc I	$3d4s^2a^2D_{3/2} - 3d4s(^3D)4py\,^2F^o_{3/2}$	3907	No data

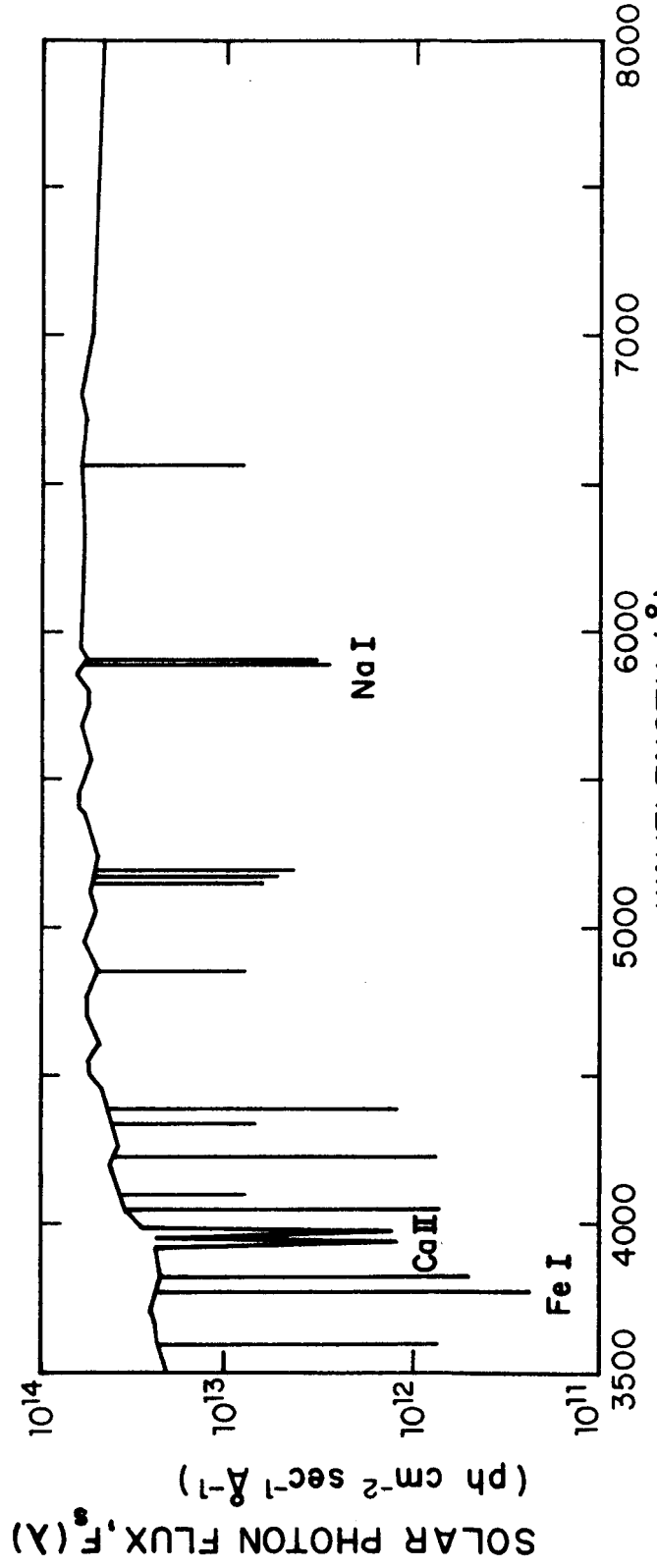

Figure 1. The solar spectrum (3500-8000Å) showing the continuum and prominent Fraunhofer absorption lines.

where appropriate. The detailed fine structure of Fraunhofer line data as applied to the present problem was obtained from the compilation due to Minnaert, et al. [44] while the continuum data have been extracted from the published results of Johnson [45]. The specific F_s-values employed in the present study are tabulated in Column 5 of Table 2; in Column 7 of that table, the nature of the solar flux data is indicated by a "c" or "f" for the cases of continuum and Fraunhofer, respectively.

Resonance Scattering Probabilities for the Selected Transitions. In addition to the F_s-values, Table 2 includes a number of other pertinent parameters for calculating the appropriate P-values. For example, Column 3 of Table 2 lists gf/g_1-values derived from the results given in Table 1 wherein the statistical weight of the ground level, g_1, has been incorporated. Additionally, in Column 4 the resultant α-values are given (see Equation (1)). Finally, in Column 6 the required P-values are listed in order of decreasing probabilities. It should be noted that the estimated error values attached to these P-values have been directly transposed from the error analysis performed in obtaining the gf/g_1-values. In other words, it is felt that in all cases the error in the solar flux values is small compared to the suggested error estimates.

Composition, Abundance and Distribution of Lunar Atmosphere Constituents. The calculation of expected signal brightness-values involves not only the appropriate P-value but also the composition, abundance, and distribution of the specific constituents investigated. Accordingly, it is necessary at this point to invoke a model of the lunar atmosphere which can be employed to define the required parameters. However, it is important to stress that the performance of the field experiment does not depend directly on the validity of any of the proposed models. In general, two models have been discussed previously in some detail by Marmo, et al. [43] so that only a summary of the salient features is required herein for completeness. These models involved two separate source functions: (1) the solar wind and (2) accretion of meteoric debris. The solar wind model employed was based on the published results of Michel [46] who has shown that the total mass, M, of any constituent (whose atomic weight exceeds four) in the lunar atmosphere due to the solar wind source can be calculated from

$$M = 1.6 \times 10^8 \, m \, f(m)/P_e \qquad (2)$$

where

m = atomic weight
$f(m)$ = numerical fraction of solar wind species (see Table 3)
P_e = escape probability (in accordance with Michel = $1.15m^{1/2}$)

The solar wind abundancies (f(m)-values) for selected materials (after Aller [47]) are given in Table 3. M-values for the individual constituents were calculated from Equation (2).

TABLE 2

SCATTERING CROSS SECTIONS, APPROPRIATE SOLAR FLUXES,
AND SOLAR RESONANCE SCATTERING PROBABILITIES FOR THE SELECTED TRANSITIONS

Element	λ(Å)	$\frac{gf}{g_l}$	$10^{22}\alpha(cm^3)$	$F_s(\lambda)\left(\frac{photons}{cm^2\ sec\ Å}\right)$ (1)	$P\left(\frac{photons}{sec\ atom}\right)$	Notes
Rb	7800.23	0.80 ± 15%	43.03 ± 15%	4.4(13)	18.9 ± 15%	c (2)
Ba	5535.48	1.40 ± 5%	37.92 ± 5%	2.9(13)	11.0 ± 5%	f (3)
Li	6707.74	0.515 ± 5%	20.48 ± 5%	5.2(13)	10.6 ± 5%	c
	6707.89	0.265 ± 5%	10.54 ± 5%	5.2(13)	5.5 ± 5%	c
Sr	4607.33	1.54 ± 10%	28.90 ± 10%	3.1(13)	9.0 ± 10%	f
Zr	6134.58	0.282 ± 25%	9.38 ± 25%	5.4(13)	5.1 ± 25%	c
Y	4142.85	0.5225 ± 25%	7.93 ± 25%	3.6(13)	2.9 ± 25%	f
Na	5889.95	0.765 ± 10%	23.46 ± 10%	7.6(12)	1.8 ± 10%	f
K	7664.91	0.685 ± 5%	35.58 ± 5%	3.8(12)	1.4 ± 5%	f
Ca II	3933.66	0.83 ± 15%	11.35 ± 15%	3.6(12)	0.41 ± 15%	f
Cr	3593.49	0.27 ± 10%	3.08 ± 10%	9.4(12)	0.29 ± 10%	f
Ca	4226.73	1.49 ± 10%	23.53 ± 10%	1.0(12)	0.24 ± 10%	f
Aℓ	3944.01	0.12 ± 10%	1.65 ± 10%	3.7(12)	0.061 ± 10%	f
Mn	4030.76	0.0567 ± 15%	0.81 ± 15%	5.8(12)	0.047 ± 15%	f
Co	3526.85	0.02 ± 15%	0.22 ± 15%	8.3(12)	0.018 ± 15%	f

Notes: (1) The number in parenthesis is the power to which 10 is raised.

(2) "c" signifies continuum.

(3) "f" signifies Fraunhofer absorption

TABLE 3

METEORIC AND SOLAR WIND ABUNDANCES
FOR SELECTED MATERIALS (AFTER ALLER [47])

Element	Relative Solar Wind Abundance,* f(m)	Relative Meteoric Abundance **
Rb	3.0(-10)	6.5(-6)
Ba	1.3(-10)	8.8(-6)
Li	9.1(-12)	1.0(-4)
Sr	4.0(-10)	1.89(-5)
Zr	1.7(-10)	5.45(-5)
Y	1.8(-10)	8.9(-6)
Na	2.0(-6)	4.4(-2)
K	5.0(-8)	3.16(-3)
Cr	2.3(-7)	7.8(-3)
Ca	1.4(-6)	4.9(-2)
Al	1.6(-6)	9.48(-2)
Mn	7.9(-8)	6.85(-3)
Co	4.4(-8)	1.8(-3)

*Based on hydrogen solar wind abundance of unity.

**Based on silicon meteor debris abundance of unity.

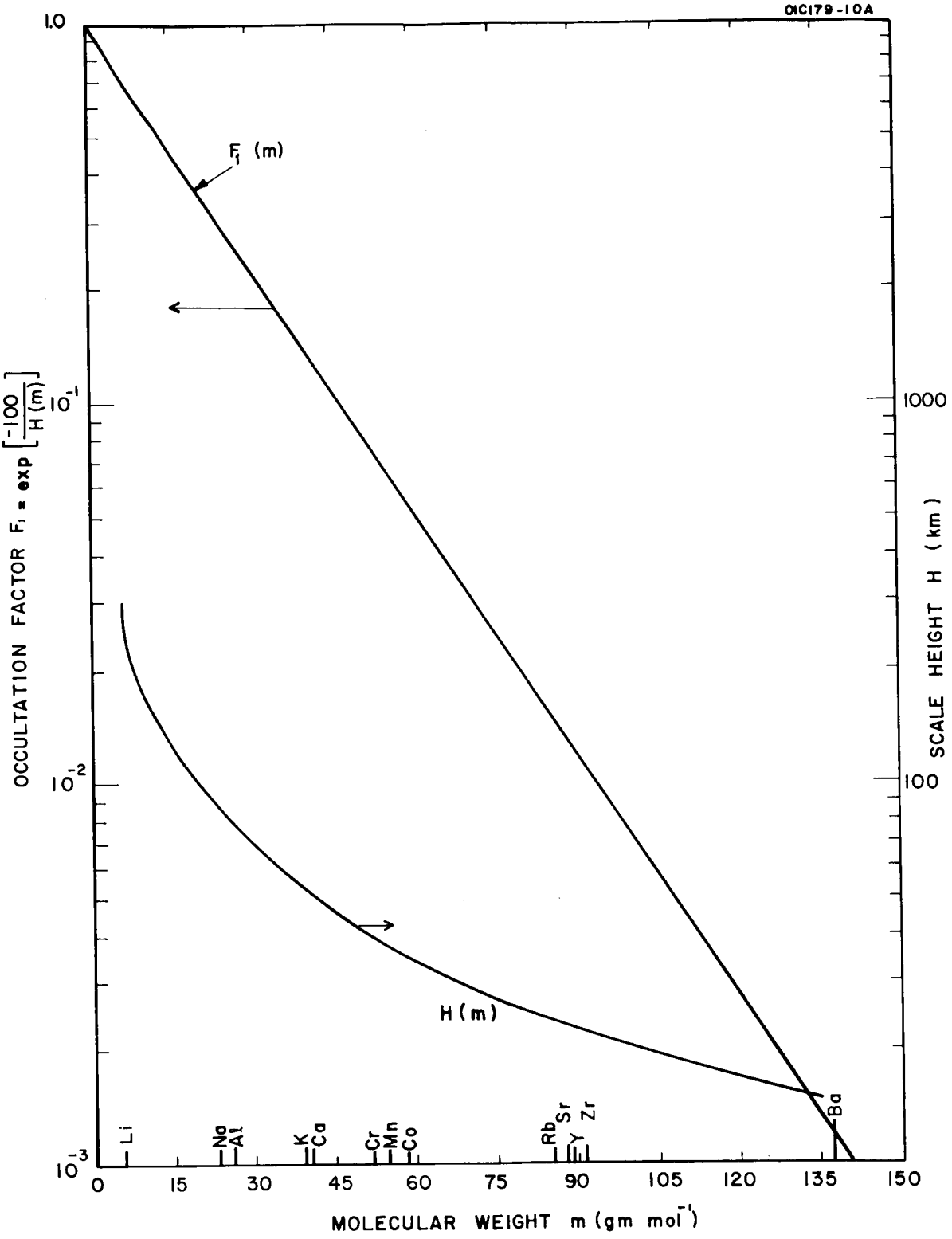

Figure 2. Derived scale heights, H(m), for several constituents and their corresponding occultation factors, F_1(m).

The other model employed a source function predicated on meteoric lunar surface impact and subsequent volatilization. This is admittedly an oversimplified model in which it is assumed that the resultant atmospheric species constituencies are in direct proportion to the meteoric abundances shown in Table 3. In calculating the expected signal brightness-values, the results were normalized for a total surface number density of 10^4 cm^{-3}. Specifically then, since silicone is the most abundant material of meteoric debris, it is assumed that it contributes about 10^4 cm^{-3} to the surface number density.

Finally, for both models an estimate was required for the contribution due to ionic species. For this purpose, it was assumed that their contribution amounts to no more than 10^{-3} of the corresponding neutral species. Specifically then, the ion density due to Si^+ amounts to no more than 10^1 cm^{-3}. The applications of an ionization factor of 10^{-3} is in accordance with the calculated estimates due to Bernstein, et al.[48].

The above two models yield estimates for the constituency and abundancy of the specified atmospheric constituents. It is now necessary to define the distribution of these species in the lunar atmosphere before the final signal brightness-values can be calculated. For this purpose, a planetary exospheric, i.e., lunar atmosphere, has been employed wherein it has been previously demonstrated [43] that the individual altitude-number density distributions for each material corresponds to their individual scale heights, H(n). For the present calculations, a mean lunar atmospheric temperature of 400^oK was applied; the corresponding scale heights for the selected constituents are presented in Figure 2 by the curve marked H(m). The required calculations also involve the cm^2-column count of atmospheric species tangent to but 100 km above the lunar surface, $N(h_1)$. This latter requirement is due to the occultation technique to be employed in the field; its role will be described later. In any case, Marmo, et al.[43] have shown that this horizontal column count can be calculated by

$$N(h_1) = n_o \, H(2\pi X)^{1/2} \left(1 + \frac{3}{8X}\right) F_1 \qquad (3)$$

where

$$X = \frac{R + h_1}{H}$$

n_o = surface number density (derived from models)

H = scale height

R = lunar radius

h_1 = occultation altitude (100 km)

F_1 = occultation factor = $\exp-(h_1/H)$

It is evident that the F_1-value can be defined as an occultation factor which accounts for the reduction in signal as a function of that lunar altitude along which the cm^2-column count is derived. The F_1-values corresponding to the several constituents considered are also given in Figure 2 by the solid line so designated. Finally, Tables 4 and 5 contain the calculated values of the integrated column counts and resultant resonance scattered signal brightness-values based on the solar wind and meteoric debris models, respectively. The values are given in order of decreasing signal brightness for observing along altitude, h_1 = 100 km. The overall variation in signal brightness-values is considerable; they range from tens of kiloRayleighs to a fraction of one Rayleigh. Reference will be made later to these values on the discussions of instrumentation capability in Section III.

Extended Background Brightness Values

The total background brightness B_t, pertinent to the present experiment, involves a complex sum of a number of sources which are in turn functions of several independent variables. For convenience, the total background can be expressed symbolically as:

$$B_t(\lambda,\alpha,\psi,\epsilon,S) = B_d(\lambda,\epsilon) + B_a(\lambda) + B_s(\lambda,\alpha,\psi) + B_z(\lambda,\epsilon) + B_{sc}(\lambda,\epsilon,S) \quad (4)$$

where B_d = lunar disc component
B_a = night airglow component
B_s = stellar component
B_z = zodiacal component
B_{sc} = scattered moonlight component

The variables involved are defined as follows:

α = galactic latitude
ψ = galactic longitude
λ = wavelength in the visible
ϵ = elongation angle in the ecliptic plane
S = field experimental conditions (this factor includes prevailing seeing conditions, coronagraph scattering, spectrometer scattering, etc.)

The component, $B_d(\lambda,\epsilon)$ representing the background contribution due to reflection of solar radiation by the lunar disc is essentially eliminated as a result of the use of the Sacramento Peak coronagraph occultation disc (it is noted subsequently that, as a precautionary measure, the lunar disc has been experimentally "over occulted"by 100 km). In the following discussions, the background contributions due to the stellar and night airglow components are shown to be insignificant. Additionally, the variations of

TABLE 4

CALCULATIONS OF INTEGRATED COLUMN COUNT AND RESONANCE SCATTERED SIGNAL BRIGHTNESS-VALUES BASED ON THE SOLAR WIND MODEL

Element	Integrated Column Count $N(h_1)(cm^{-2})$	Signal Brightness* $\Phi(h_1)\left(\frac{\text{photons}}{cm^2\ sec}\right)$
Na	2.5×10^{10}	1.5×10^{10}
Ca	3.0×10^{10}	1.0×10^{9}
Aℓ	2.3×10^{10}	3.8×10^{8}
K	1.0×10^{9}	2.1×10^{8}
Cr	6.3×10^{9}	1.4×10^{8}
Mn	2.3×10^{9}	7.6×10^{6}
Rb	1.3×10^{7}	3.7×10^{6}
Sr	1.8×10^{7}	2.2×10^{6}
Ca II	3.0×10^{7}	1.7×10^{6}
Co	1.4×10^{9}	1.4×10^{6}
Zr	8.2×10^{6}	5.0×10^{5}
Li	3.5×10^{4}	4.0×10^{5}
Y	8.4×10^{6}	3.1×10^{5}
Ba	9.4×10^{6}	1.2×10^{5}

*One Rayleigh equals a brightness of 10^6 photons/cm^2 sec.

TABLE 5

CALCULATIONS OF INTEGRATED COLUMN COUNT AND RESONANCE SCATTERED SIGNAL BRIGHTNESS-VALUES BASED ON METEORIC DEBRIS MODEL

Element	Integrated Column Count $N(h_1)(cm^{-2})$	Signal Brightness* $\Phi(h_1)\left(\frac{photons}{cm^2\ sec}\right)$
Na	4.5×10^{10}	2.6×10^{10}
Li	2.0×10^{8}	2.3×10^{9}
Aℓ	9.0×10^{10}	1.5×10^{9}
Ca	3.8×10^{10}	1.3×10^{9}
K	2.5×10^{9}	5.3×10^{8}
Cr	5.3×10^{9}	1.2×10^{8}
Mn	4.5×10^{9}	1.4×10^{7}
Ca II	3.8×10^{7}	2.3×10^{6}
Zr	2.8×10^{7}	1.7×10^{6}
Sr	9.9×10^{6}	1.2×10^{6}
Co	1.1×10^{9}	1.1×10^{6}
Rb	3.4×10^{6}	9.6×10^{5}
Y	4.6×10^{6}	1.7×10^{5}
Ba	3.7×10^{6}	4.9×10^{4}

*One Rayleigh equals a brightness of 10^6 photons/cm^2 sec.

these components with both wavelength and experimental conditions are relatively minor so that only limited discussions are presented for these cases. Furthermore, under the selected experimental conditions, the zodiacal light component intensity was a minimum and, as such, contributed negligibly to the total background. Thus, it is concluded that the most important background contribution involves the combined effects of scattering of lunar radiation by the earth's atmosphere and scattering by the various optical components of the overall system.

Airglow Component. The night airglow background continuum component is believed to originate in the earth's upper atmosphere; the two most widely quoted excitation mechanisms are the influx of fast particles into the atmosphere and the delayed effects of solar radiation. According to Chamberlain [49]. the absolute continuum intensity amounts to about 4×10^4 photons/cm^2-sec-ster-Å for the spectral region $\lambda\lambda$ 3900 to 4800 Å. Roach and co-workers [50-51] have shown that in the 5300Å region the absolute intensity can vary between 1.8×10^4 and 5.3×10^4 photons/cm^2-sec-ster-Å. In any case,it appears that the night airglow background continuum is less than 1 Rayleigh/Å (where 1 Rayleigh = 10^6 photons/cm^2-sec) throughout the visible region. For the present purpose, a constant value of 0.68 Rayleigh per Å has been adopted as representative as indicated in Figure 3 by the appropriately marked curve.

In addition to the continuum contribution, it is known that the Na-D lines are prominent features of the night airglow. For example, according to Chamberlain [49] the night airglow intensity at 5890Å varies between 30 Rayleighs (summer value) and 200 Rayleighs (winter value) in the northern hemisphere. In the present investigation this factor has been considered in determining the absolute content of sodium in the lunar atmosphere. However, on the basis of the field measurements reported in the following section, it is evident that the source of Na-D emission can be neglected. Additionally, for the H and K lines of Ca^+, Broadfoot [52] has shown that the night airglow intensities are less than several Rayleighs. Finally, a general survey of the literature has indicated that no other significant discrete background radiations of interest in the present experiment have been observed in the night airglow.

Stellar Component. The background contribution due to the stellar component is calculated by combining the spectral distribution of radiation from the predominant stellar classes [53-57] with the observed number of stars of given magnitudes in these classes [58,59]. A parametric analysis was performed which indicated that the largest background level variations attributable to galactic longitude are about a factor of five within the galactic equatorial plane and about a factor of two at a galactic latitude of 20°. Russell, et al. [58] have shown that the stellar population at $\alpha = 20^\circ$ is essentially equivalent to that of the average sky. Additionally, the maximum background occurs in the galactic equatorial plane. A previous analysis [43] indicated that the stellar component is essentially invariant with wavelength in the visible region of the spectrum so that a constant value was employed for the present

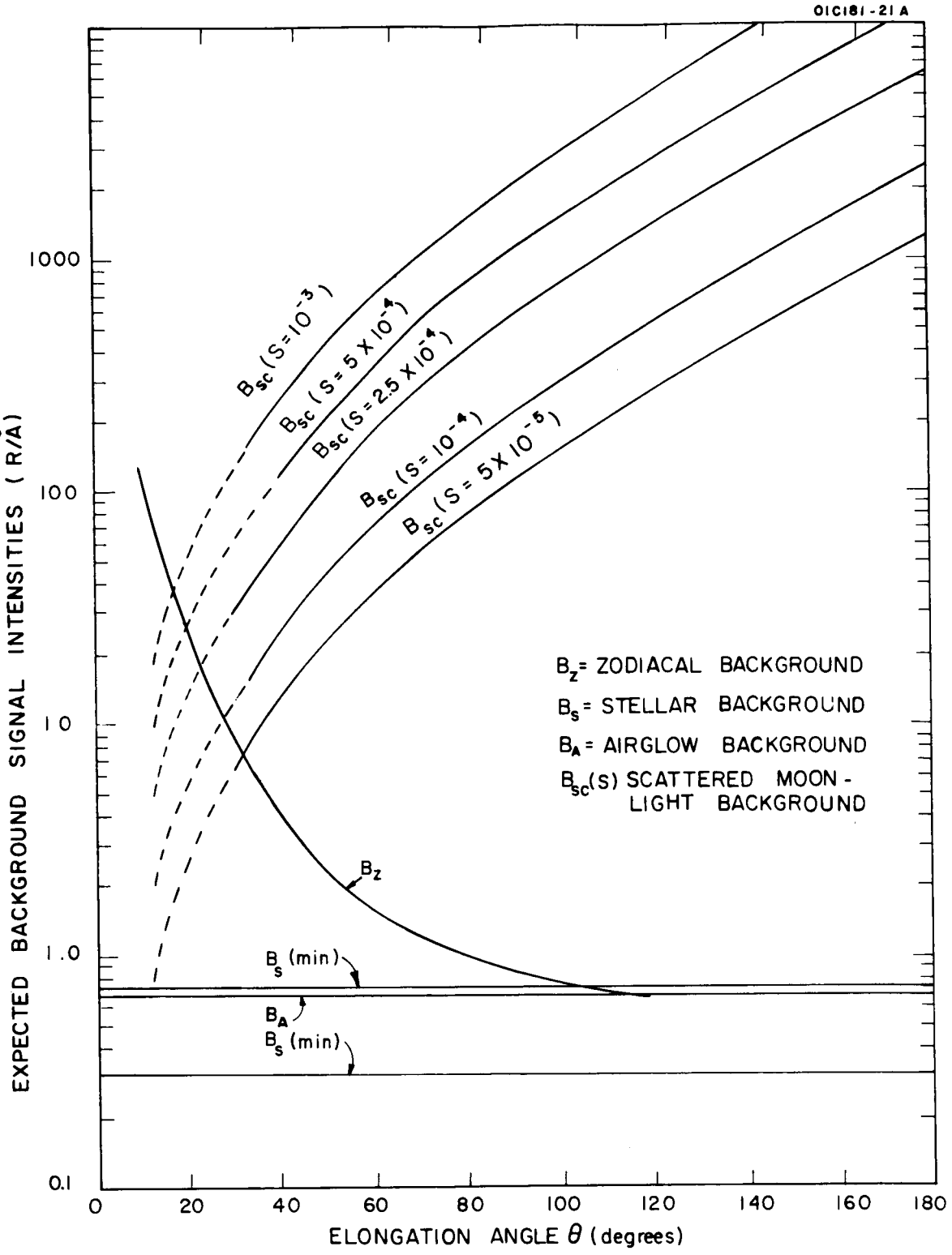

Figure 3. Expected background signal intensities for various sources.

purpose. This simplification presents no serious difficulties since it can be shown that the entire stellar component is indeed negligible. For completeness, however, two values are shown in Figure 3: $B_s(max)$ and $B_s(min)$ corresponding to galactic latitudes of 0° and 20°, respectively. In either case, however, the contribution to total background is less than 1 Rayleigh per Å.

Zodiacal Component. It is generally accepted [53,60] that the source of zodiacal light is due to the Mie scattering of solar-illuminated dust particles centered principally within the plane of the ecliptic. As a consequence, the zodiacal light intensity varies markedly with elongation angle, θ; i.e.

$$\cos \theta = \cos (\epsilon - \epsilon_\odot) \cos \beta \qquad (5)$$

where $\epsilon - \epsilon_\odot$ = differential ecliptic longitude

β = ecliptic latitude

In the present experimental configuration, an ecliptic latitude of $\beta = 0^\circ$ is appropriate so that the elongation angle may be used interchangeably with the differential ecliptic longitude. The zodiacal light intensity increase at low elongation angles has been verified experimentally [60-62]. Furthermore, these data indicate a minimum value at about 90° and an essentially constant value for larger elongation angles up to 180°. As expected, the spectral variation of zodiacal light closely approximates that of the solar spectrum. In Figure 3, the over-all intensity variation of zodiacal light is plotted as a function of elongation angle for a representative wavelength in the visible spectral region. This curve clearly indicates the difficulties involved in performing the experimental observations at small elongation angles.

Earth Atmospheric and Instrumental Scattering of Lunar Radiation. It has been shown in the preceding discussions that the several pertinent background sources are either negligible or can be minimized. However, scattering of the lunar radiation in the earth's atmosphere as well as scattering by the optical components of the system represents a significant source of background.

Since neither theoretical nor observational data were available from which this background contribution could be assessed for measurements performed along and tangent to the lunar disc limb, a directly applicable experimental solution to the problem was sought. Although an occulting disc was employed in the measurement program, the above background source still remained. Thus, during the initial stages of the program, photometric measurements were performed at Sacramento Peak under full moon conditions to determine the brightness ratio from areas on the lunar disc and within the lunar atmosphere at an altitude of 100 km above and tangent to the lunar limb. In a detailed account of these measurements, presented elsewhere [63], it was shown that for the field conditions which

prevailed, the measured ratio (off-the-disc/on-the-disc) was 2.5×10^{-4} for $\lambda\lambda$ 4558, 5540, and 6714Å [63]. Thus, with this representative value for the visible region it is now appropriate to estimate an absolute value for the background contribution when observing lunar atmospheric constituents along a line of sight 100 km above and tangent to the lunar limb. For example, it has been established that for $\lambda = 5540$Å, the lunar mean spectral radiance is about 2.1×10^{12} photons/cm^2-sec-ster-Å [63]. Thus, application of the measured ratio of 2.5×10^{-4} results in a background brightness value of 5.2×10^{8} photons/cm^2-sec-ster-Å for off-the-disc observations which are equivalent to 6.5×10^{3} Rayleigh/Å.

The seeing conditions under which the 2.5×10^{-4} value was measured were described by resident Sacramento Peak personnel as "good but not excellent." According to their estimates, a ratio of 5×10^{-5} could prevail under optimum seeing conditions. Alternatively, observations could probably be performed under less than ideal conditions where the ratio could be as high as 1×10^{-3}. Accordingly, for the present task, a range of seeing conditions between 5×10^{-5} and 1×10^{-3} was considered representative.

These calculations employed the relative magnitudes of lunar radiation as a function of lunar phase from Chorvinsky [53], as shown in Table 6.

Calculations of B_{sc} were performed in the visible region as a function of elongation angle for ratio values of 1×10^{-3}, 5×10^{-4}, 2.5×10^{-4}, 1×10^{-4}, and 5×10^{-5}; the resultant curves are shown in Figure 3.

The Variation of the Background Contribution with Season and Lunar Age

The major feature shown by the data of Figure 3 is that the B_{sc} contribution clearly dominates (especially for elongation angles greater than 20-40°) depending on the prevalent seeing conditions. In addition, the background estimates of Figure 3 were obtained for a zenith look angle which represents an optimum experimental situation since at lower elevation angles, the background contributions tend to increase whereas the signal intensities would remain constant or decrease. A more realistic appraisal of this aspect of the problem is presented in Figure 4 where the lunar elevation angle is shown as a function of season and lunar age as derived from the Nautical Almanac [64] for the period June 1966-June 1967. The curves clearly indicate that maximum elevation angles obtain during late fall, winter, and early spring. Additionally, Sacramento Peak personnel have indicated that optimum seeing conditions at Sacramento Peak occur during middle October to late November. For these reasons it was decided to perform the field experiment during the late fall time period.

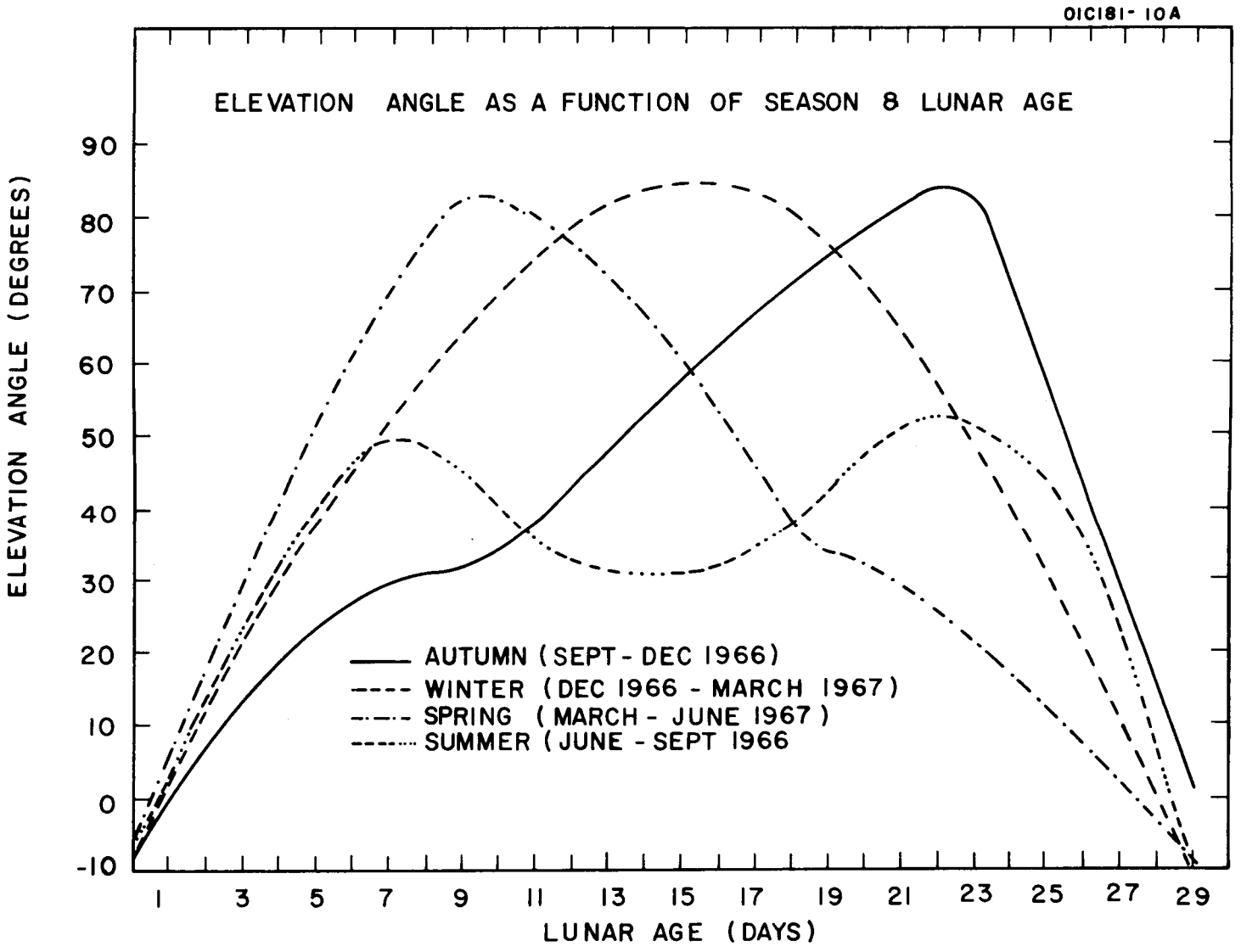

Figure 4. Local lunar elevation angle as a function of season and lunar age.

TABLE 6

LUNAR INTENSITY REDUCTION FACTORS AS A FUNCTION OF LUNAR PHASE OR ELONGATION ANGLE (after Chorvinsky [53])

Elongation Angle (θ, deg)	Lunar Phase	Intensity Reduction Factor
10	Crescent	0.003
30	Crescent	0.007
40	Crescent	0.010
50	Crescent	0.015
60	Crescent	0.025
70	Crescent	0.040
80	Crescent	0.058
90	Quadrature	0.082
100	Gibbous	0.116
110	Gibbous	0.159
120	Gibbous	0.210
130	Gibbous	0.273
140	Gibbous	0.355
150	Gibbous	0.460
160	Gibbous	0.600
170	Gibbous	0.800
180	Opposition	1

III. EXPERIMENTAL INSTRUMENTATION

In this section the major optical and electronic components of the GCA designed and fabricated instrumentation system are described. This system was coupled to the Sacramento Peak coronagraph to perform the experimental observations discussed in the next section. Although a major portion of this discussion has been presented previously in a limited distribution project report [63], the material is also reproduced herein for report completeness.

The section is subdivided into two major discussion areas: (1) optical components including the pre-optic system and the Fastie-Ebert type spectrometer and (2) electronic components including the photon detection subsystem and the spectral scanning device.

Optical System Design

As noted previously, successful performance of the experiment requires the efficient coupling of the GCA instrumentation configuration to the Sacramento Peak coronagraph. This requirement intrinsically imposes a number of physical constraints upon the final optical design of the Fastie-Ebert type spectrometer. As such, the following discussion will first involve specification of the physical and optical constraints imposed on the system design. As a consequence of the above, the parametric design features of the major optical components of the system will be specified.

Physical and Optical Constraints. A basic tenet governing the performance of the field experiment at Sacramento Peak was noninterference with the routine scientific activity of the observatory. On the basis of a series of discussions between key GCA and observatory personnel in this regard, it was mutually decided to accommodate the overall GCA instrumentation configuration in the space designated in Figure 5. In this scaled schematic, it should be noted that all components in the observing room represent permanent installations except for the plane mirror, lens, and GCA spectrometer. Although this arrangement was spatially generous, it introduced a number of physical and optical constraints on the systems design. The scientific requirements also introduce constraints, the sum total of which are listed below as boundary conditions to the system design phase of the optical system.

(1) The dimensions of the over-all system could not exceed 2 meters in length and 1 meter in width according to the space allocation of Figure 5.

(2) Variations in lunar image size (owing to the variable Earth-moon distance) must be accommodated by the pre-optics system.

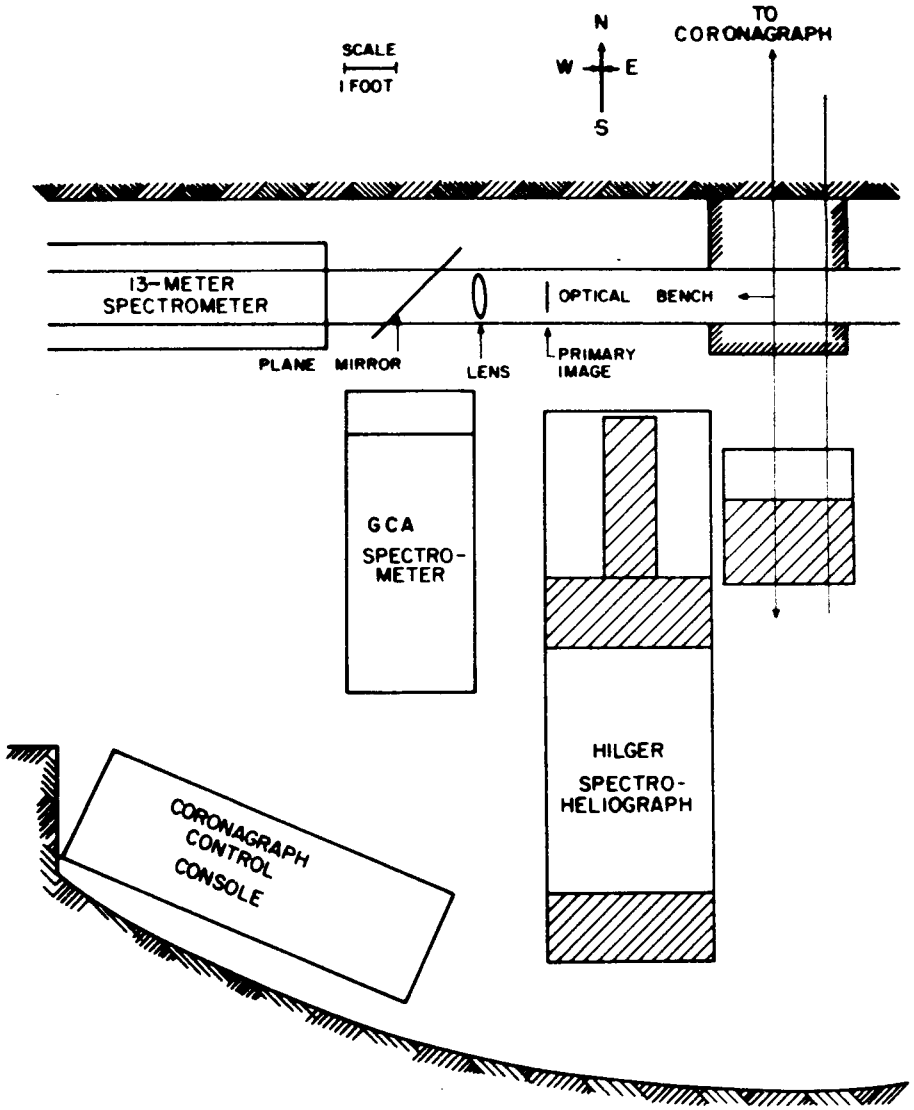

Figure 5. Observing room showing position of spectrometer (in scale).

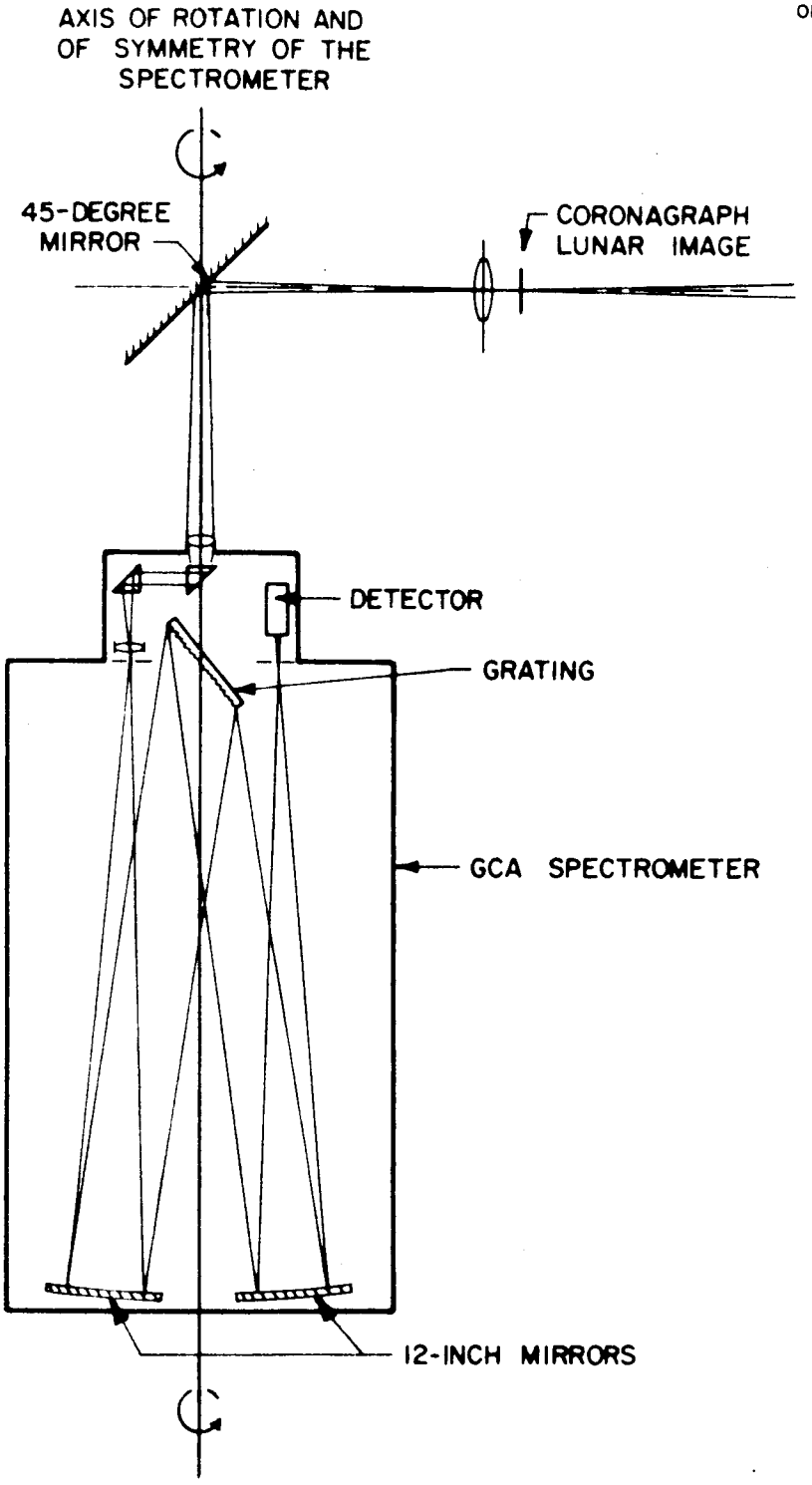

Figure 6. Scaled optical configuration of pre-optic and spectrometer systems.

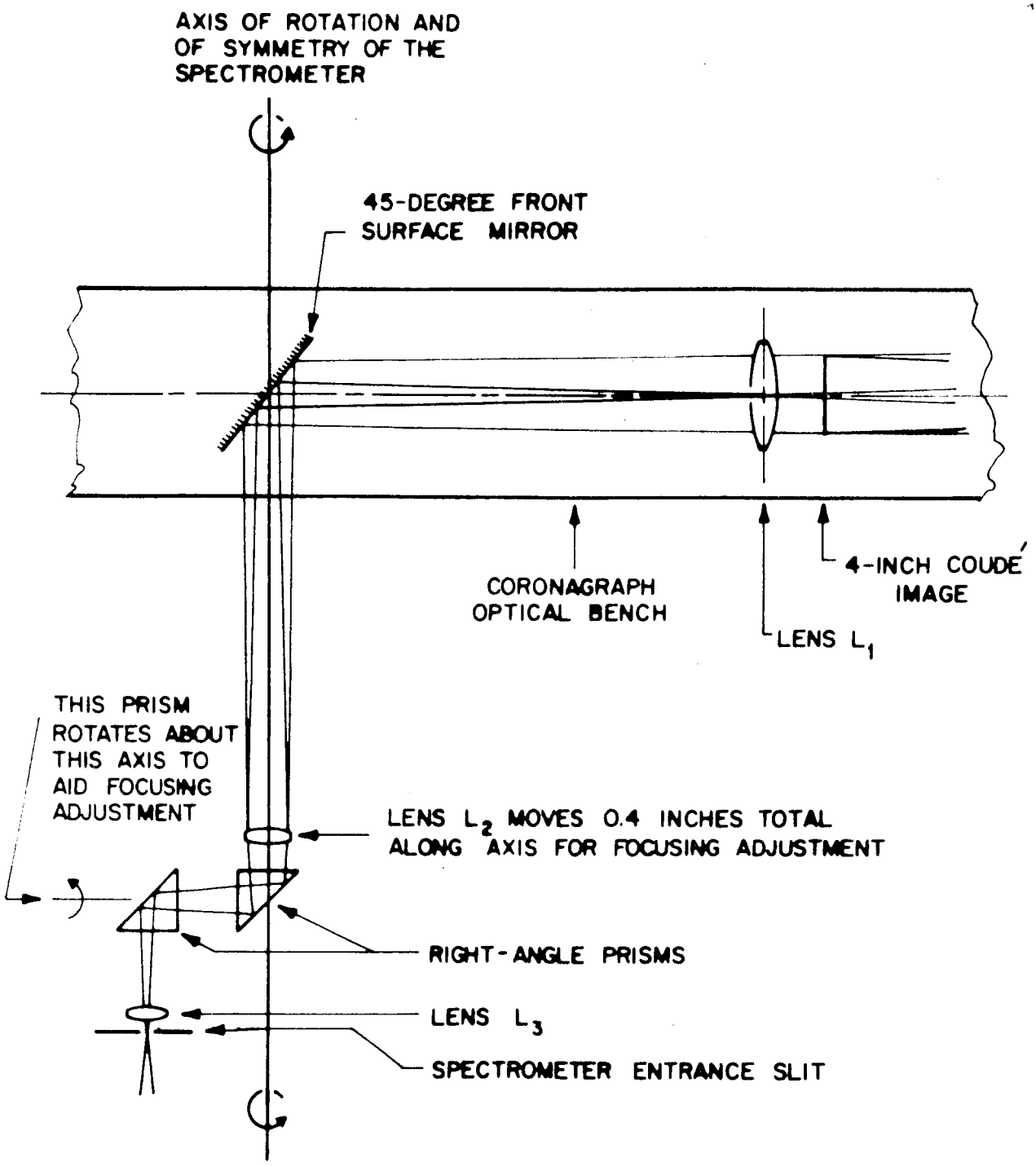

Figure 7. Scaled schematic diagram of pre-optic system.

(3) The AΩ-product of the pre-optics system should be compatible with that of the coronagraph (that is, f/35, with the 4-inch Coudé image).

(4) The pre-optic and spectrometer systems should subtend a sector of the lunar image which corresponds to an atmospheric sector (above the lunar limb) of about one scale height and which at the same time yields a spectral resolution of about one Angstrom.

(5) Both systems should possess cylindrical symmetry to accommodate the rotation of the lunar image as it traverses the sky during a given observation night.

(6) The spectrometer should employ curved entrance and exit slits to both maximize system throughput and match the curvature of the lunar image after focussing onto the entrance slit.

(7) In satisfying the above requirements, the optical throughput should not be reduced significantly.

Design of Pre-Optic and Fastie-Ebert Type Spectrometer Components. The number of constraints stipulated above must be accommodated by both major optical components, i.e., the pre-optic subsystem and Fastie-Ebert type spectrometer. As noted above, design of the optical components must be achieved under the constraint of optical throughput conservation, which is accomplished by simply preserving the AΩ (area-solid angle)-product at each successive focal plane. Predicated on this and the other constraint factors, a scaled drawing of the final optical configuration is presented in Figure 6. The following discussions include the detailed analytical and theoretical considerations employed in the design of both the pre-optic subsystem and the Fastie-Ebert type spectrometer.

With respect to the former, the selected pre-optic subsystem satisfied the constraint criteria (1) through (5) above. The general design features are specified in detail in the scaled schematic diagram of Figure 7. It can be seen that three lenses and two prisms, employed as indicated in the figure, essentially comprise the pre-optic subsystem. Lens L_1 focusses the 4-inch Coudé image onto lens L_2 via the 45-degree front surface mirror. This lens then reimages the Coudé image onto the spectrometer entrance slit via the lens, L_3. The axis of L_2 is concentric with the cylindrical rotation axis of the spectrometer as required. In practice, lenses L_2 and L_3 and the two right-angle prisms are mounted physically to the spectrometer. Since the positions of both the first prism and lens L_2 (along its own axis) are adjustable, proper focussing can be achieved at the entrance slit of the spectrometer for a variable size Coudé image. It can be seen from Figure 7 that the pre-optic subsystem arrangement can accommodate the lunar image rotation so that a constant sector of the lunar atmosphere can be maintained in focus (onto the entrance slit) throughout an entire evening of investigation. This is accomplished by displacing the beam laterally to the entrance slit by

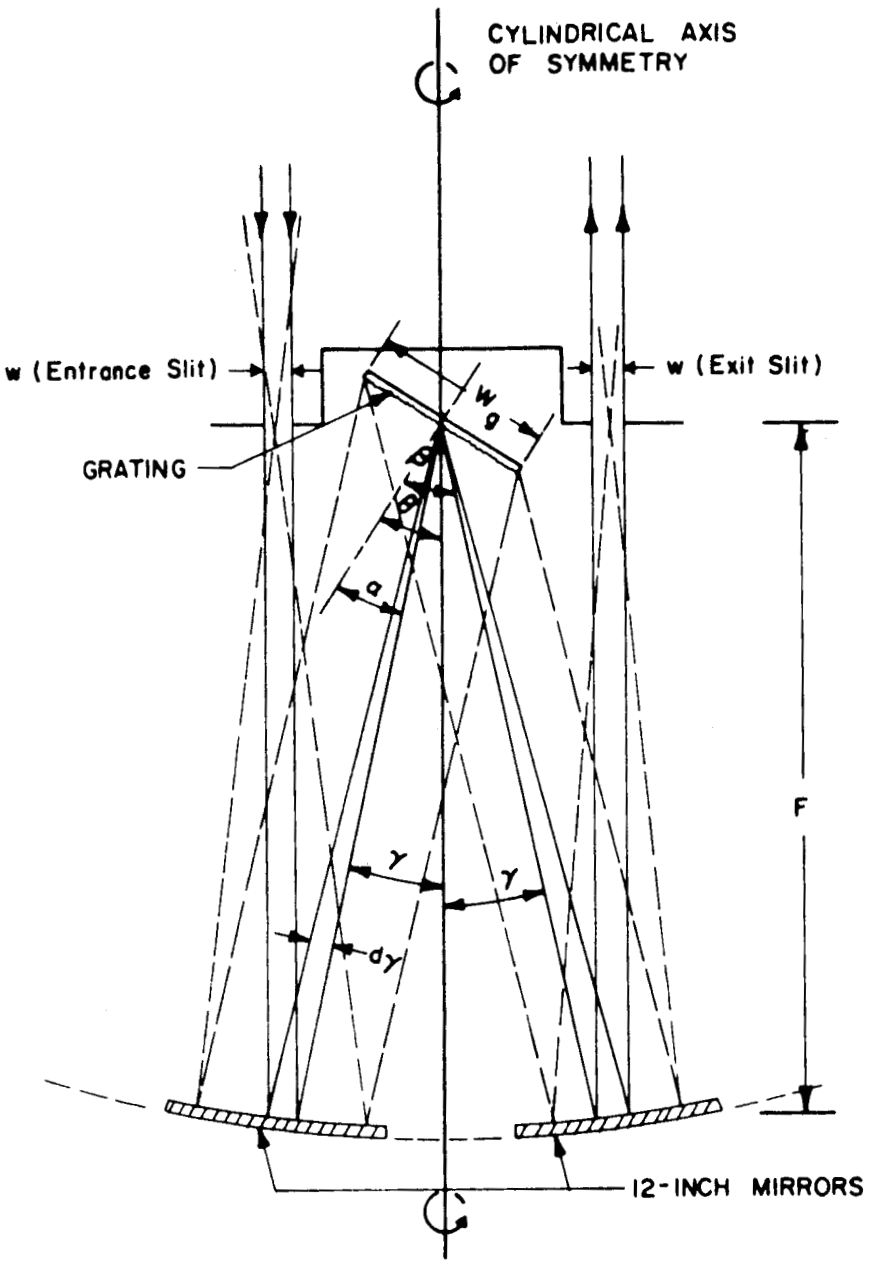

Figure 8. Detailed scaled schematic of Fastie-Ebert type spectrometer.

the set of prisms and by establishment of the geometrical situation wherein the cylindrical axis of symmetry of the spectrometer is concentric to the axis of the undeflected beam as shown in Figure 7. With this arrangement the spectrometer can be rotated about its cylindrical axis so that an accurate track can be maintained of the lunar image. This function was performed manually in the field since the rotation rate requirement is sufficiently modest. It may also be noted from Figure 7 that provisions were made to accommodate an interference filter in front of lens L_2 for either gross order sorting or narrow spectral discrimination.

The major items employed in the design of the pre-optic subsystem were available commercially as off-the-shelf components. Assembly and test of these components were performed at the GCA laboratories to assure compliance with the experimental design objectives. In addition, special holders were machined at GCA to attach the indicated pre-optic system components to the existing optical bench in the observing room.

A scaled schematic diagram of the Fastie-Ebert type spectrometer is presented in Figure 8. The indicated design satisfied constraint requirements (3) through (6) above. In Figure 8 it can be seen that this design configuration satisfies the requirement of cylindrical symmetry discussed previously. The design was also predicated on optimization of several additional parameters associated with the scientific requirements discussed in the previous section. These parameters include: (a) size, w, of the entrance and exit slits (these are equal in the present application), (b) the radius of slit curvature to match the lunar limb, (c) the grating constant, d, (d) the spectrometer focal length, F, (e) the grating width, W, (f) the f-number of the coronagraph, f_c (in this case, f/35), and (g) the spectral resolution, $d\lambda$.

Since representation of the above number of pertinent factors into appropriate analytical expressions suitable for parameter optimization was not deemed practicable in the present applications, an alternate philosophy was adopted in which specific parameters were isolated and evaluated in terms of a number of possible alternative combinations. This iterative technique produced progressively better design characteristics until a final acceptable compromise design was achieved. It will be shown that the final design demonstrates a capability which is sufficient to achieve the specified scientific objectives, albeit not necessarily optimized. This is to be expected in view of the fact that reasonable compromises and trade-offs were applied to the design problem including such considerations as component cost and delivery (that is, off-the-shelf availability), desirable PM tube and grating characteristics, in addition to the ensemble of physical and optical constraints on the system stated previously. It is clearly difficult to discuss in detail the iterative design analysis described above, although the highlights of the procedure employed are briefly described below.

First, it is appropriate to specify those parameters which are relatively defined due to the list of constraints cited. For example, in coupling the spectrometer to the coronagraph, the pre-optics subsystem must possess a nominal linear magnification of about one-third. Thus, since the size of the lunar Coudé image is fixed, this specification dictates that the spectrometer entrance and exit slits have a radius of curvature of 17.1 mm, which matches the configuration of the 4-inch lunar limb image when focussed upon the entrance slit. It also turns out that the simultaneous achievement of a resolution of about one Angstrom and subtending a 35-km increment of lunar atmosphere (less than one scale height) requires a slit width of about 0.33 mm for operation in the second order. In addition, since the angular divergence of the coronagraph beam is defined by its f-number, the iterative analysis involving selection of the remaining design parameters can now be performed. At this point, constraint (7) was invoked wherein the optical throughput of the spectrometer was not reduced significantly.

In accordance with Figure 8 and the requirement that the AΩ-product be conserved, it can be shown that

$$w_c/f_c = w/f \tag{6}$$

where w_c = the annular width at the Coudé focus (for this case, this width subtends a 35-km altitude increment of the lunar atmosphere). This expression involves a pre-optic system with a magnification, $M = w/w_c$. Furthermore, from Figure 8, it can be seen that

$$f = \frac{F}{W_g \cos \alpha} \tag{7}$$

where α is defined in the figure. Combining these equations results in

$$\frac{w}{F} = \frac{w_c}{f_c} \frac{1}{W_g \cos \alpha} . \tag{8}$$

Differentiation of the well-known grating equation yields

$$d\lambda = \frac{d}{n} (\cos \alpha + \cos \beta) \frac{w}{F} \tag{9}$$

where d is the grating constant, n is the order of operation, and $d\alpha = d\beta = d\gamma = w/F$ (see Figure 8). Substitution of Equation (9) into Equation (8) yields

$$d\lambda = \frac{d}{n} \left(\frac{\cos \alpha + \cos \beta}{\cos \alpha} \right) \frac{w_c}{f_c} \cdot \frac{1}{W_g} . \tag{10}$$

The basic relationships between both the spectral resolution of the system and the grating parameters as well as the variety of parameters associated with proper coupling to the f/35 coronagraph 4-inch Coudé image are expressed in Equation (10). In this regard it is instructive to insert specific values into Equation (10). As will be demonstrated subsequently, a grating suitably blazed in the visible spectral region with 1200 grooves per mm which operates in the second order represents a realistic selection. Additionally, if a focal length of 1.5 meters is selected and convolved with a pre-optic system magnification of 1/3, it turns out that a spectral resolution of better than one Angstrom can be easily achieved with a grating width dimension of approximately 10 inches. Indeed, since a grating having 1200 grooves per mm has an inherent resolving power much greater than 1Å, it may be argued that the grating is being employed inefficiently. However, the requirement for a grating of this rather large size results from satisfying the constraints imposed by Equations (6) through (10). Briefly, then, it is evident that this grating choice involved a trade-off between the grating size and the minimum usable resolving power compatible with the overall system configuration in order to achieve the objectives of the field program.

The above arguments involve another important parameter; namely, the slit function and the associated system throughput. For the case involving a Fastie-Ebert type configuration, geometric optic considerations show that its slit function is generally trapezoidal wherein the lengths of the top and base are $\cos \alpha - \cos \beta$ and $\cos \alpha + \cos \beta$, respectively. It can be shown that the maximum internal throughput is preserved when the total wavelength increment, $d\lambda$, is divided equally between contributions from the entrance and exit slits respectively for any grating setting. In this case, $\cos \alpha = \cos \beta$ so that the resultant slit function is triangular. However, α and β vary individually with wavelength; this requires the use of variable slit widths to preserve maximum internal throughput over the entire spectral region investigated. In order to avoid this instrumental complication, it was decided to examine the throughput problem in terms of a compromise design employing fixed slit widths. In this case for a given λ, $\cos \alpha \neq \cos \beta$ so that a trapezoidal slit function results since, for a given slit width, w, there is a corresponding loss in effective resolution. A detailed analysis has been performed to define α- and β-values which would result in minimum throughput loss over the entire spectral range. For the specified design, the predicted behavior was confirmed in the laboratory during the performance of required calibration measurements using a number of light sources (these results are discussed later in the text where they are illustrated in Figure 12).

With respect to the presently designed mirror configuration, theoretical considerations indicate that the optimum focal length is 147 cm. Having specified a 10-inch grating, the conventional Fastie-Ebert type

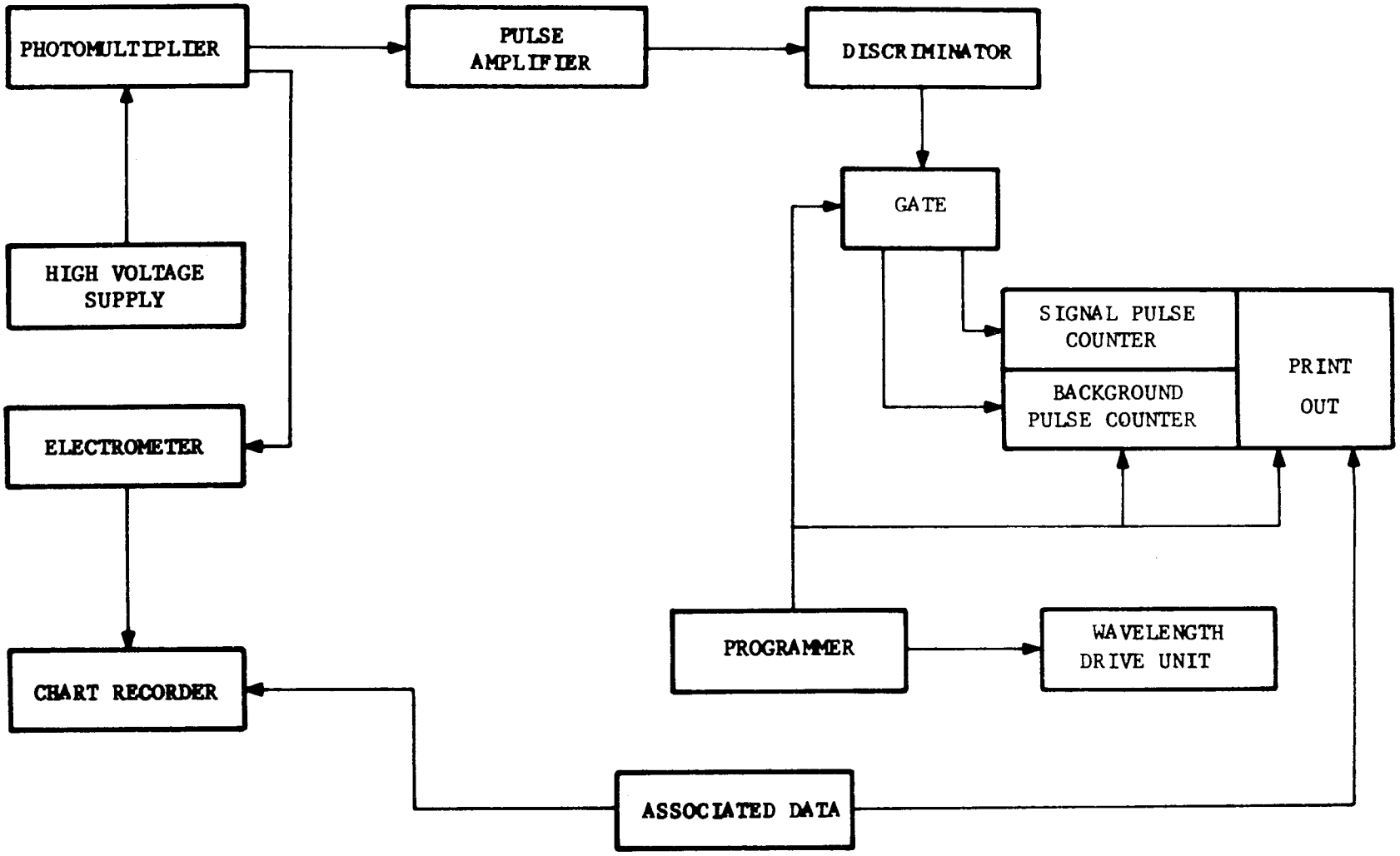

Figure 9. Block diagram of overall photon detection-spectral scanning subsystems.

spectrometer design requires a single mirror with about a 24-inch diameter. However, a survey of commercially available products indicated that this size mirror would be too costly, require a long delivery time, be at least 4 inches thick, and have a weight in excess of 150 pounds. Finally, the single large size mirror would represent an inefficient choice since only about one-half of the total surface area would be utilized effectively. Accordingly, it was decided to employ two mirrors, each 12 inches in diameter with equivalent radii of curvature. In the fabrication, by Diffraction Limited, the radii of curvature were matched to within ±0.020 inch so that they could be installed with a common focus.

Finally, the choice of grating was predicated on both practical and theoretical considerations. The detailed analysis and rationale employed in this selection is not discussed herein, although a brief commentary on the more salient factors are appropriate. For example, a large grating results in maximum throughput but finite size limitations do exist on the basis of commercial availability and cost. In addition, a geometric size limit is also imposed by the constraint that for this design the entrance and exit slits must be located beyond the extremities of the grating dimensions. Such additional factors as spectral resolution, viewing angle, focal length, cost, and availability were considered in the final selection decision. Furthermore, theoretical considerations indicate that as the width of the grating is increased, off-axis aberrations become increasingly important in limiting spectral resolution. It can also be demonstrated that since it is required to preserve the f-numbers, a further increase in grating width would necessitate a concomitant increase in focal length. To do otherwise, simply results in less efficient illumination of the grating with a resultant sacrifice in system throughput.

In summary, the pertinent optical characteristics of the major components of the pre-optic subsystem and Fastie-Ebert type spectrometer are presented in Table 7 for ready reference.

Electronic System Design

The electronic system consists of the photon detection and spectral scanning subsystems. These subsystems perform distinctly independent functions and as such, are discussed separately below. Since the photon detection and spectral scanning subsystems are spectrometer components they are included in block diagramatic form in Figure 9.

Photon Detection Subsystem. The design of the photon detection subsystem were predicated on the following representative requirements:

(1) A representative system integration time of 10 seconds was established in order to fix the performance requirements of the guidance subsystem.

TABLE 7

SPECIFICATIONS OF OPTICAL PARAMETERS FOR SPECTROMETER

GRATING: - Bausch and Lomb Plane Grating

Blank Size:	16.5 x 26.5 cm
Ruled Area:	15.4 x 25.6 cm (1200 grooves/mm)
Blaze Wavelength:	1st order blaze at 1.35μ
Blaze Angle:	54^{o}
Order of Operation:	2nd or 3rd order, depending on the spectral region

SLIT:

Radius of Curvature:	17.1 mm
Slit Width:	0.33 mm
Separation of Entrance and Exit Slits:	34 cm

SPECTROMETER MIRRORS:

Focal Length:	147 cm
Diameter:	12 inches

OPTICAL FEED SYSTEM:

Linear Magnification: 1/3

Lens Parameters:

	Focal Length	Diameter	Remarks
L_1	122 cm	15.5 cm	air spaced doublet
L_2	33 cm	5.4 cm	coated, corrected objective lens
L_3	33 cm	5.4 cm	same as above

Lens Spacing:

L_1 to L_2: 137 cm (mean)

L_2 to L_3: 40 cm effective optical path (mean)

Prisms: Right angle, internal reflecting

(2) The experimental measurements will be performed under background-limited conditions wherein the estimated background level is on the order of several kiloRayleigh Å^{-1} as shown in Figure 4 and discussed in greater detail in the following section.

(3) A system spectral resolution of about one Angstrom is desirable.

The photon detection subsystem employed a thermoelectrically cooled (to -20°C with a Products of Research, Inc. housing) EMI 9558-QA PM tube whose response was coupled to a Baird pulse height analyzer (Model No. 530A, Series II). The latter included a suitable PM tube high voltage supply, counting circuits, timing circuits, and a counting discriminator. The unit was capable of counting the output pulses of the PM tube within a preset time interval. These data were then presented in digital form using a Baird Model 620-2 printer. The pulse height analyzer included a discriminator circuit which was capable of rejecting signal pulses which were less than a predetermined amplitude level. By proper calibration, a level could be established whereby the dynode thermal electron pulses could be selectively rejected so that the recorded counting rates are due only to the cathode emission of thermal and signal photoelectrons. This capability was applied to the problem of tube selection in the following manner. First, an appropriate discriminator level setting was established by operating a given PM tube in a completely dark environment. Observations of the counting rate versus the pulse height discriminator level were plotted; the resultant data were then employed to isolate the contribution from cathode thermal electrons. After obtaining similar data for a number of tubes, the lowest background count and highest quantum efficiency criteria were employed in the selection of the specific EMI 9558-QA.

A representative plot of the dark current integral counting rate as a function of discriminator level is presented in Figure 10 for the selected photomultiplier tube operating at -20°C. It should be noted that a significant slope variation is present at a discriminator level of about 7. Thus, operation at a slightly higher discriminator level results in dark current counting rates which are still less than ten per second along with minimum sacrifice of signal counting rate.

Spectral Scanning System. In the previous spectrometer system design discussion, spectral scanning was achieved by grating rotation through an angle θ (see Figure 8). Since in this system $\alpha = \theta - \gamma$ and $\beta = \theta + \gamma$, a direct proportionality exists between the exit slit wavelength, λ, and $\sin \theta$, which prompted the use of a sine drive mechanism for spectral calibration, readout, and scanning. In addition, a suitable electronic sine drive circuit was designed to provide field operation flexibility as discussed below.

The precision screw employed in the sine drive was custom fabricated by the D. W. Mann Co. It should be noted that the grating drive repeatability exceeded ± 0.05Å, which represents about an order-of-magnitude better performance than required for the purposes of the experiment.

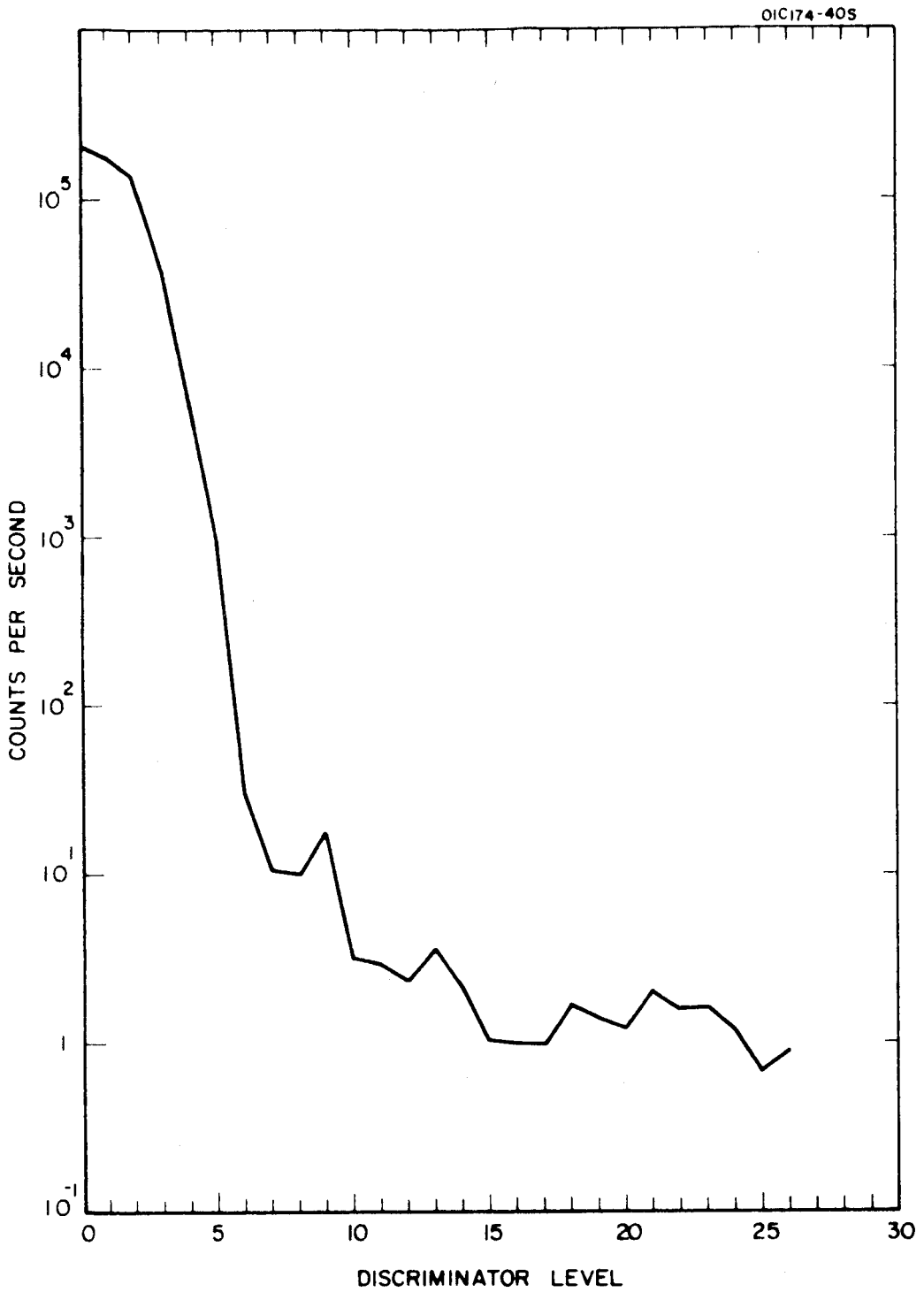

Figure 10. Discriminator level of PMT.

The sine drive mechanism was activated and programmed by means of the rather involved electronic circuit which is shown schematically in Figure 11. The circuit was coupled to a special stepper motor to allow control of the grating drive by two independent switches. The first switch, designed for manual control, has three positions; the first two position increases or decreases the wavelength through the stepper motor, while the third position locks the grating in any particular location. The second switch is intended for automatic operation in four modes, the first of which involves grating position control where the scanning rate is proportional to a manually-determined knob pot setting. In the second mode, the stepper motor operates at one step per second, corresponding to a minimum scan rate of 1Å per 24 seconds in the first order (clearly, a proportionately-reduced rate pertains at the higher orders). In the third mode, the grating is operated by a position switch which allows for a change in one position (1/24Å in the first order) on demand. The final operational mode permits rotation of the grating through a preset number of steps between 1 and 256 so that a careful scan through suspected line positions can be achieved automatically.

In practice, the final sine drive alignment was achieved by performing laboratory runs in which known discrete emission light sources were employed in the appropriate spectral orders. Sine drive counter readings were recorded simultaneously at the corresponding known spectral positions as observed at the exit slit. This spectral calibration technique involves an iterative procedure from which satisfactory sine drive alignment can be deduced when a straight line relationship exists between the counter reading and the exit slit wavelength.

Before shipment to Sacramento Peak, the over-all optical-electronic system configuration was checked in the laboratory in order to evaluate its capability under as closely simulated field conditions as possible. Specifically, the parametric values employed were those listed in Table 7 since these were predicated on actual field requirements. A number of light sources were employed in various orders to check the performance throughout the visible wavelength region of interest. In Figure 12 data are shown on the performance achieved with a Na D lamp. Similar data were observed for several other cases; namely, Ca, Ca^{+}, Hg, and Ne. On the basis of these results, it was established that (1) the photon detection subsystem was operating properly, (2) the sine drive alignment and electronic scan mechanism functioned according to expectations, and (3) the over-all GCA optical-electronic system performed as required under simulated conditions so that one could confidently couple the instrument to the Sacramento Peak coronagraph and expect suitable experimental performance from the complete configuration.

The second order spectrum shown in Figure 12 was obtained using slit widths which measured 0.33 mm. It can be seen that the observed effective resolution (corresponding to the line half-width) is about 2Å which, though less than optimum, adequately fulfills the requirements of the experiment as described previously. Additionally, the above capability will be applied subsequently in the following section with respect to field data analysis.

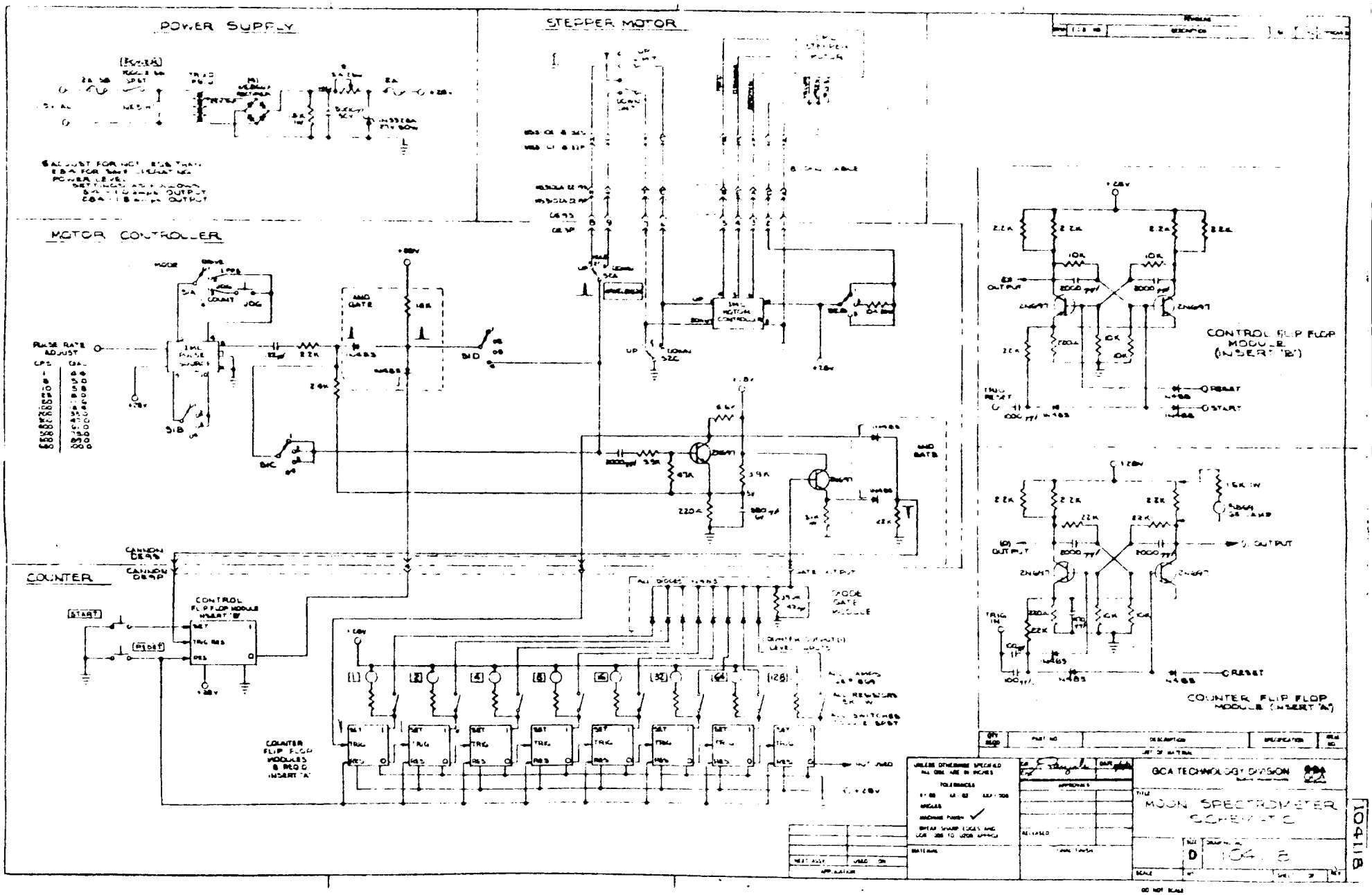

Figure 11. Schematic diagram of wavelength scanning electronics.

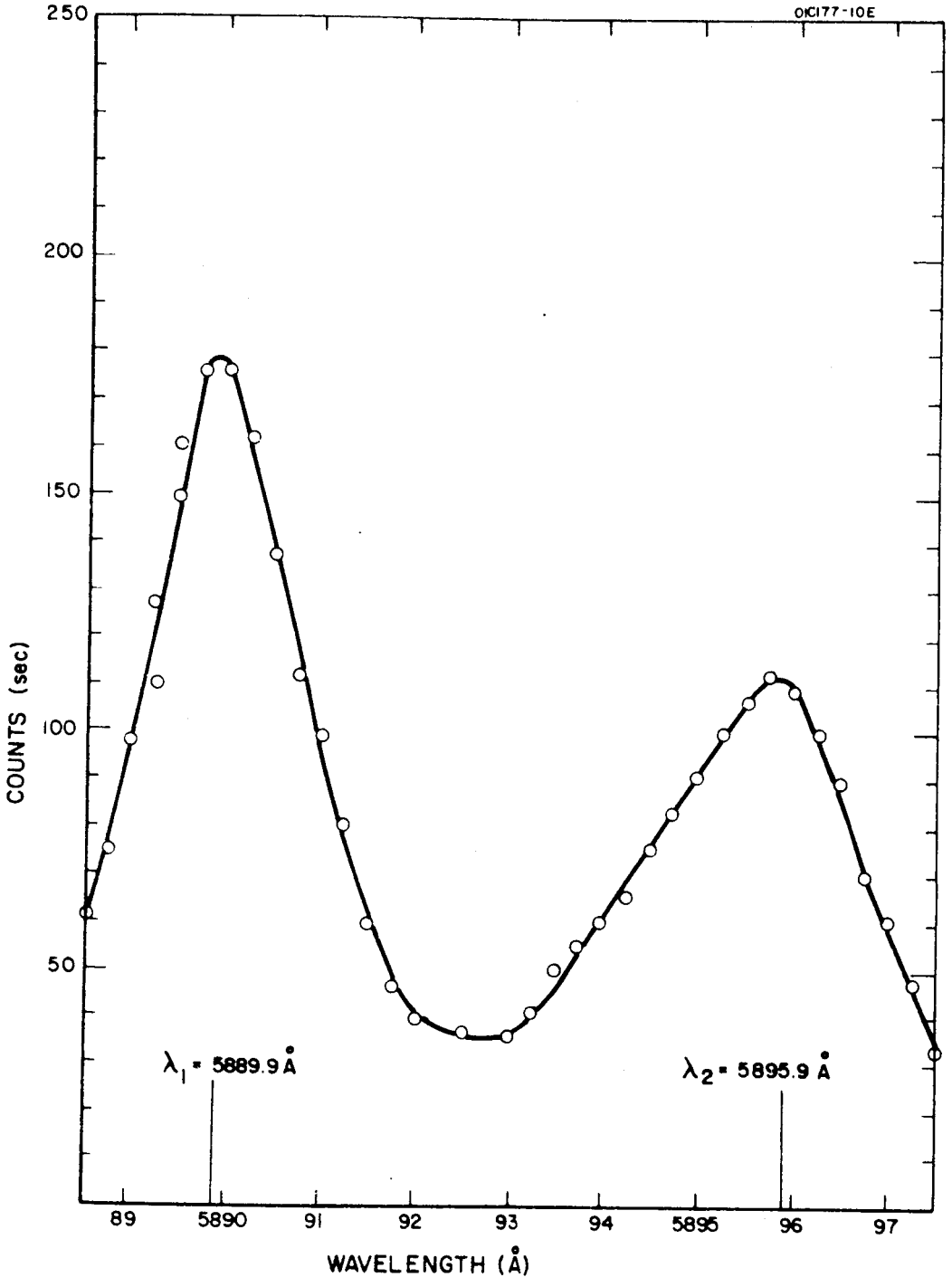

Figure 12. Spectrum of Na I D-lines.

Having completed the above checkout phase, the optical-electronic system was disassembled for shipment to Sacramento Peak. However, prior to disassembly, it was decided to take appropriate measures to facilitate field reassembly of the instrument. For example, several of the instrumental settings and configurations established by complex and tedious trial-and-error procedures were maintained by locking, marking, recording, etc. where appropriate. As a result, a number of subsystems evolved which contained several related components; these were generally packaged for shipping as individual units. For example, the two 12-inch spherical mirrors were attached to the back plate of the spectrometer and this ensemble was considered as a packaging unit for shipment. As such, proper focus adjustment, center commonality, and entrance-exit slit alignment, derived in the laboratory could thus be maintained during the shipment and reassembly phases of the program. Additionally, the calibrated sine drive screw was locked into that unique position at which the line of the grating rotation angle is linearly proportional to the rotation of the drive screw and hence the counter number. Finally, the photon detection subsystem was treated as a single unit to avoid the complex reassembly procedure for this component. After disassembly of the complete instrument, the component and subsystem elements such as described above were packaged and shipped to Sacramento Peak on 5 November 1966. The material arrived in workable condition on 7 November 1966 at which time the reassembly procedure was initiated.

IV. FIELD MEASUREMENT PROGRAM

The complete GCA system was reassembled at Sacramento Peak without notable difficulty owing largely to the precautionary packaging procedures discussed in the previous section. Omitting the reassembly details herein, it can be stated that the instrumentation system performance was essentially equivalent to that achieved in the laboratory so that the descriptive performance data of Figure 12 and Table 7 are applicable and representative of the field performance. Prior to the actual data acquisition phase of the program, a number of necessary preliminary tasks were performed as discussed below in the following order:

(1) Coupling of the GCA System to the Sacramento Peak coronagraph
(2) Guidance Procedure and Capability
(3) Field Program Operational Schedule
(4) Experimental Procedure for Data Acquisition

Coupling of the GCA System to the Sacramento Peak Coronagraph

The first major task involved coupling of the complex GCA instrumentation system to the Sacramento Peak coronagraph as shown in Figure 5. In this regard, it was necessary to first achieve good optical alignment for a given spectrometer – coronagraph configuration and to then maintain alignment for all other rotating and variable lunar image size situations as required. These critical alignment requirements were satisfied by the tedious iterative application of the number of successive adjustments described below.

First, the base screws of the spectrometer were adjusted to insure that the centers of the optical axis of the spectrometer and the 4-inch Coudé lunar image were aligned precisely along a common line-of-sight. The preoptics system was then employed (as discussed in the previous section) to properly focus the Coudé image onto the entrance slit so that its radius of curvature exactly matched the fixed jaw radius of curvature of 1.7 cm at proper magnification. This initial preoptic magnification-focussing procedure was facilitated by utilizing the previously marked adjustment positions established in the laboratory under simulated conditions prior to shipment. Spectrometer-coronagraph optical alignment was accomplished by projecting an extremely narrow pencil of light (located at the center of the 4-inch Coudé image) along the center ray path as indicated in the preoptic configuration of Figure 7. At the L_2 position, a plane front surface mirror was located perpendicular to the optical axis of the spectrometer to reflect the pencil ray precisely back upon itself when the 45-degree mirror was positioned properly. Although this procedure guaranteed spectrometer-coronagraph alignment for a specific configuration, preservation of this alignment for the variable lunar diameter and/or the rotating lunar image involved further adjustments as described below. In this regard, it should be noted that many alignment procedure features are common with those involving system guidance so that a somewhat detailed discussion is appropriate herein.

The primary alignment requirement is the ability to establish, maintain, and periodically verify satisfactory Coudé lunar image-spectrometer slit configuration. With regard to the guidance and alignment mask shown in Figure 13, the 4-inch diameter heavy-lined circular portion (designated as the Coudé image size of the lunar limb) is representative of the actual coronagraph Coudé lunar image size which obtained during the final two weeks of November 1966. The concentric circles on either side of the heavy-lined circle represent 100 km lunar altitude increments. The mask was fabricated of an opaque material so that when placed at the focal plane of the coronagraph, the lunar image could only be observed through the cutout portion which was fitted with a thin translucent material. For the purpose of achieving optimum alignment, the entrance slit image was projected onto the Coudé lunar limb image so that the configuration shown in Figure 14 could be established by employing the following procedure. A high intensity light source was positioned (in the spectrometer) a short distance behind the entrance slit in order to project and superpose the real image of the entrance slit back onto the Coudé lunar image as viewed on the mask at the focal plane of the coronagraph. If the desired configuration did not prevail, several minor adjustments could be employed. For example, the images of the radii of curvatures of the lunar limb and the projected slit could be made coincidental by rolling the entire spectrometer, forward or backward as required, to obtain proper magnification. The resultant magnification variation would then necessitate compensating adjustments to L_2 to recover sharp focus at the new operating magnification. In practice, these several operations were repeated iteratively to achieve the configuration illustrated in Figure 14. Using the above procedure, satisfactory alignment, focus, and magnification were maintained for a variable lunar diameter. Once this tedious phase was completed, it was found that allowance for lunar image rotation presented no serious difficulties since the spectrometer was designed to rotate about its optical axis, and as such, the slit image rotated concentrically with the lunar image. In practice, the required spectrometer rotation was performed manually since the relatively low lunar rotation rate was conducive to such an operation.

Guidance Procedure and Capability

The alignment, magnification, and focussing effort discussed above can be envisioned as the preparatory procedure for guidance operation. For example, once the configuration shown in Figure 14 is achieved, the disk can be occulted for the data acquisition configuration shown in Figure 15. At this point in the procedure, the primary guidance function is to maintain the operating configuration for a statistically significant time period. The guidance procedure developed and successfully employed in the data acquisition procedure is described below.

Intrinsic to the Sacramento Peak facility was the capability of semi-automatic tracking of the sun over prolonged time periods. Direct application of this capability to the present lunar tracking requirement indicated that small corrections were required to the existing right ascension and declination rates. Since the right ascension drift occurred parallel to the slit center, it represented the more sensitive and critical adjustment. However, since this drift was relatively

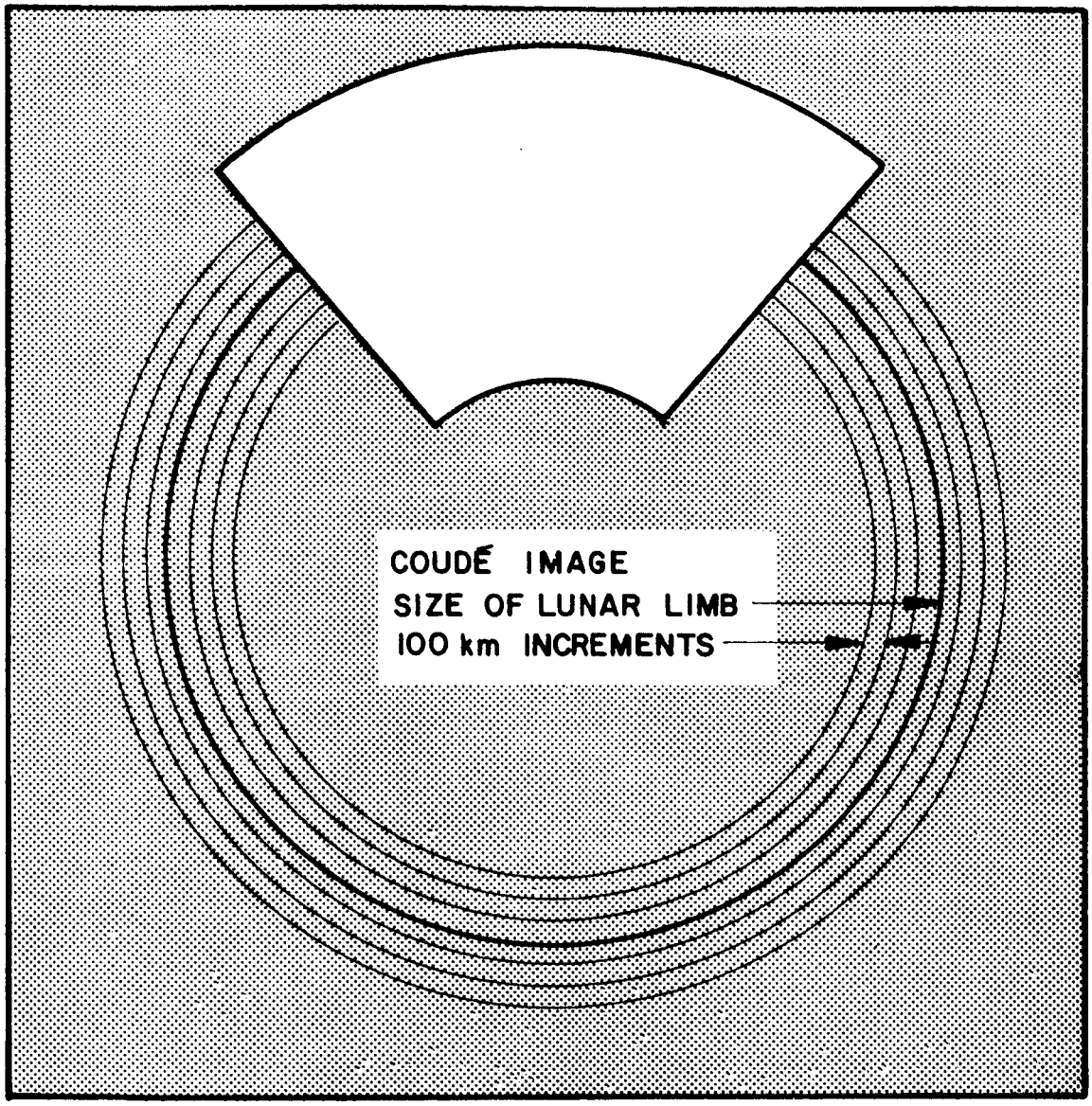

Figure 13. General features of the guidance and alignment mask.

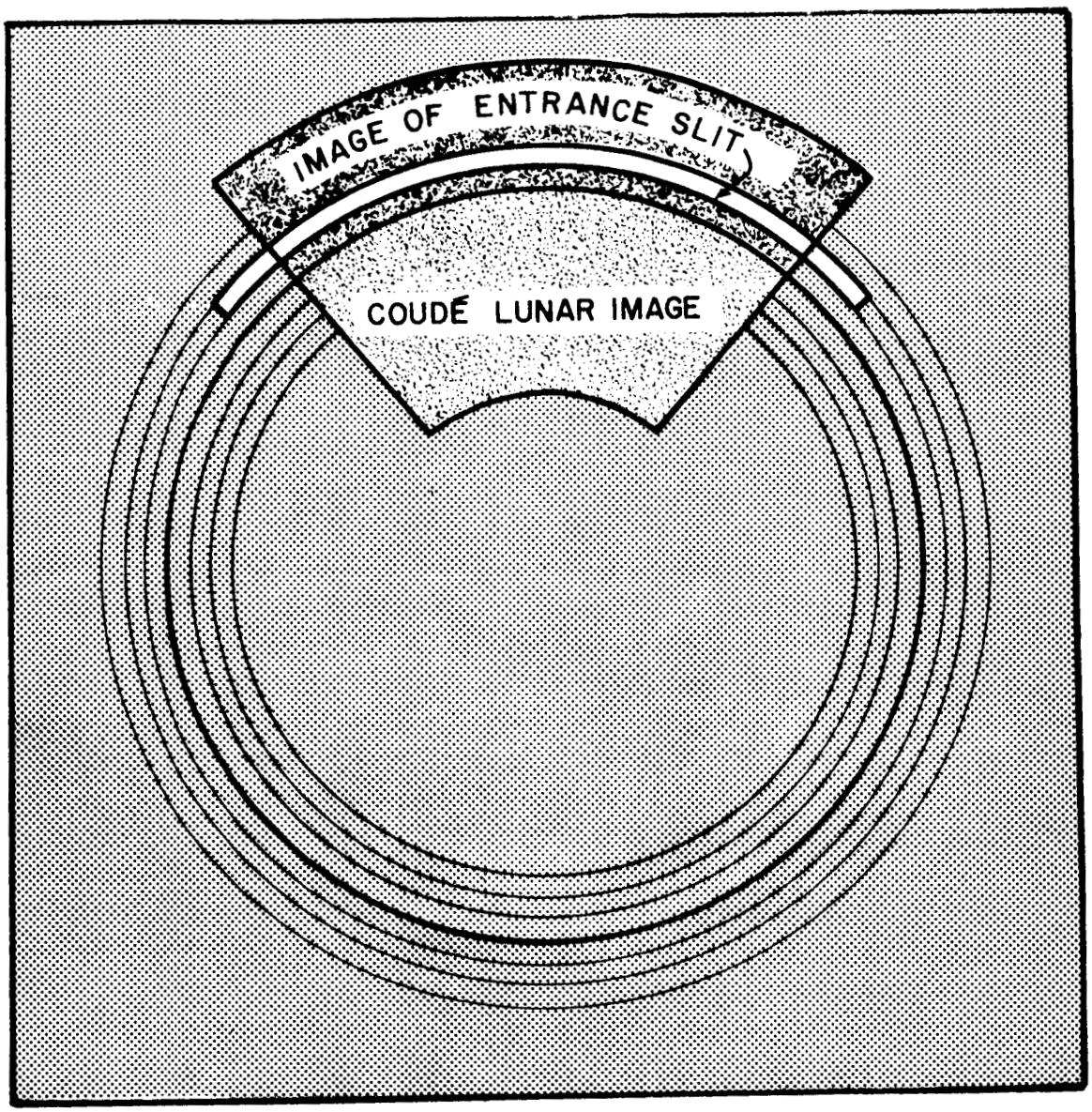

Figure 14. Alignment and guidance mask configuration for focus, magnification and alignment procedure.

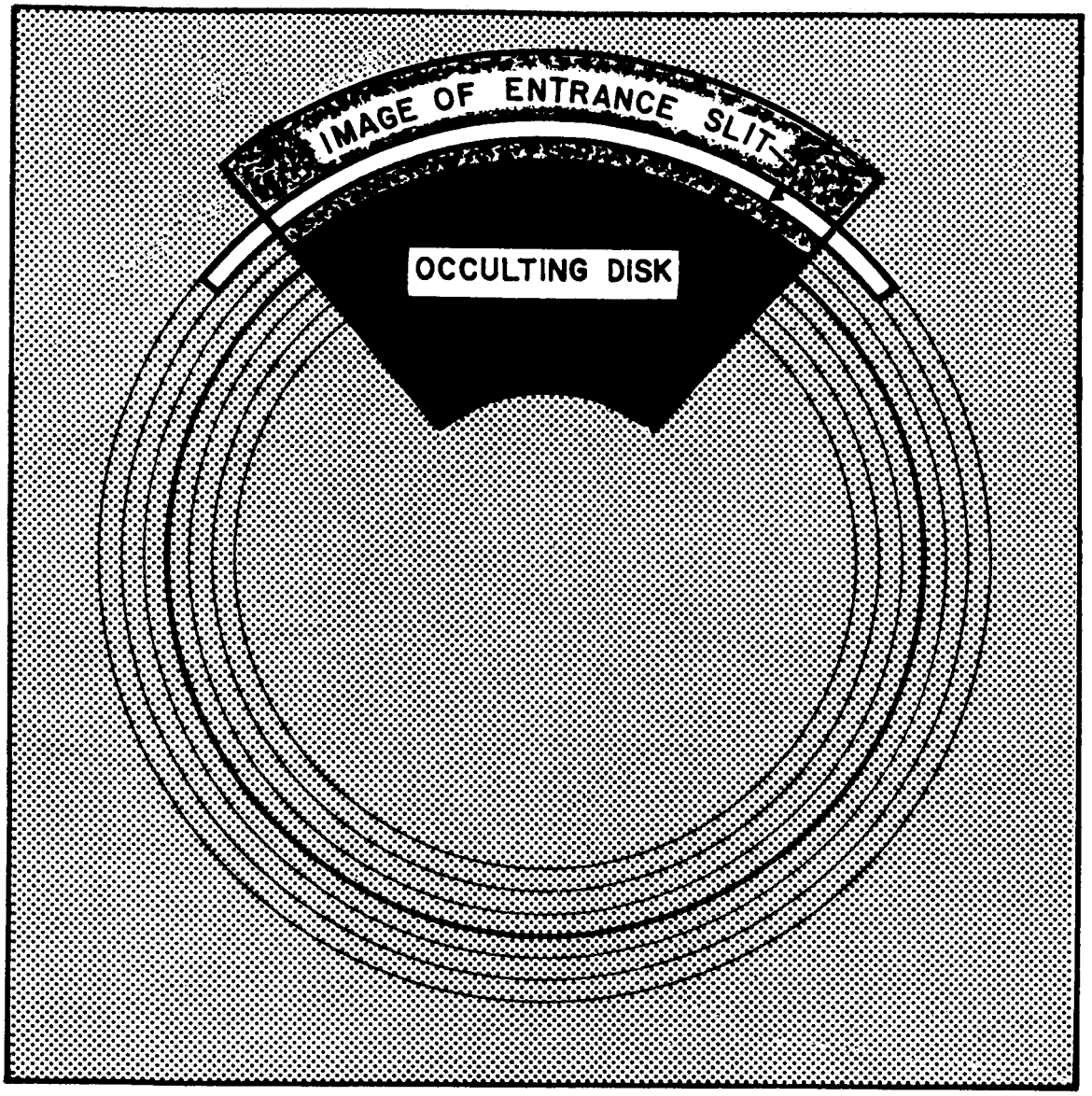

Figure 15. Guidance mask configuration for acquisition of lunar atmosphere data.

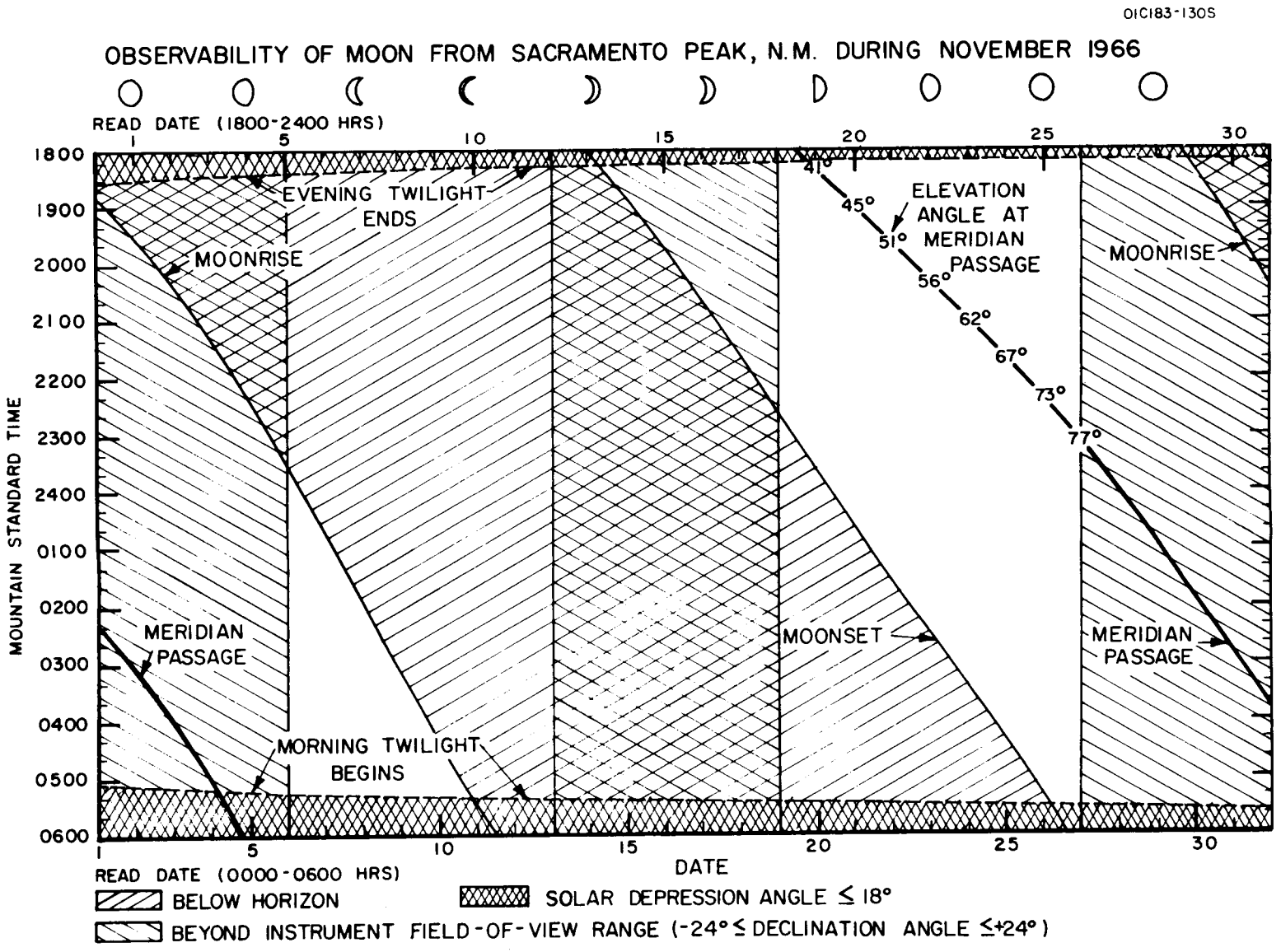

Figure 16. Composite data map of several lunar observation constraints.

moderate, employment of the standard solar rate resulted in a relative drift which amounted to only a 100 km increment (at the moon) in a time period of about 100 seconds. Fortunately, the relative declination drift was even less; additionally, since it occurred in a line perpendicular to the slit center, appropriate corrections were applied more easily.

In order to apply the required corrections, an appropriate electronic device was designed which adjusted the right ascension and/or declination rate of the existing coronagraph servo motors; the degree of adjustment desired was regulated by means of two corresponding Vernier scales. In practice, first the appropriate right ascension rate correction was applied; thereafter, it became a straightforward task to correct for the error in declination.

In the field, the over-all guidance procedure could not be tested adequately except for those few evenings when weather conditions allowed the Coudé lunar image to be observed. However, in spite of this constraint, the guidance procedure employed in the data acquisition phase allowed three to six successive 15-second increment measurements (total observation time of 45 to 90 sec) to be performed before a significant drift was observed. This capability was sufficient for the successful performance of the experimental field program described in Section V.

Field Program Operational Schedule

As noted in Section II, the planned performance of the field experiment was scheduled for the month of November 1966. Figure 16 represents a composite data map which identified the various lunar observation restrictions from the Sacramento Peak facility during the month. First, field measurements could only be performed after astronomical twilight (i.e., the solar depression angle exceeds 18 degrees) which is identified in Figure 16 by the double crosshatched regions. Additionally, the solar coronagraph is operational for declination angles between $\pm 24^{\circ}$; the effect of this restriction is illustrated by the single crosshatched lines of Figure 16. Finally, the opposite sense single-hatched regions indicate those periods during which the moon was located below the horizon. It is evident from the figure that field measurements could be performed only in those regions where no crosshatched lines of any kind appear; on this basis the available operational dates include 18-26 November 1966, inclusively. Note also that in Figure 16 the plot of lunar elevation angle at meridian passage versus individual dates makes it evident that more optimum viewing conditions (i.e., higher lunar elevation angles) prevailed for longer time intervals toward the latter part of the indicated available observation period. However, in the final analysis, the experimental capability was limited by the over-all seeing conditions that prevailed during a given evening as discussed in Section II. In this regard, for any given evening it was, of course, not possible to predict the presence of suitable seeing conditions during some portion of the indicated

observation hours (see Figure 16). Accordingly, each evening between 18 and 26 November 1966, a preparatory procedure described below was followed so that the equipment would be on a ready-to-go standby basis.

Four hours prior to astronomical twilight the PM tube was cooled so that by the time observations could be performed, steady-state conditions would prevail. Histogram analyses were performed to establish representative PM tube voltage discriminator levels and to additionally check the entire photon counting electronic device. Parallel to this operation, an optical alignment check was performed in accordance with previous discussions. Additionally, whenever a lunar image was available, the guidance procedure was performed for familiarization purposes and to establish representative Vernier settings for that evening. Each evening the wavelength calibration settings were rechecked by employing appropriate light sources. In general, this over-all procedure was repeated continually so that the equipment would remain on a ready-to-go standby basis. These procedures were refined for data acquisition on 26 November 1966 as described in the next section.

In practice, it turned out that the prevailing synoptic weather conditions during the period 18-26 November 1966, as shown in Table 8, presented the major restriction on the operation of the field program. The data pertain to Albuquerque for 2300 MST; however, they are generally representative of the evening weather conditions prevalent at Sacramento Peak for the dates cited. It can be seen that suitable weather conditions prevailed for three evenings; namely, 19, 21, and 26 November. Poor seeing conditions prevailed for 19 November, and only marginal seeing conditions prevailed during the evening of 21 November. During the latter evening, a full field operational program procedure was employed; unfortunately, only qualitative data were obtained. However, this opportunity to apply the full operational procedure served to further refine the final data acquisition procedure which was employed throughout the evening of 26 November 1966.

Definition of Experimental Parameters and Procedure for Data Acquisition

Definition of Experimental Parameters. The experimental procedure adopted for the data acquisition phase of the program was predicated on a preliminary analysis to identify the pertinent parameters to be measured. In the final analysis, the raw data consist of total counts registered on the Baird 620-2 Counter. It will be shown [see Equations (11) and (28)] that in order to interpret the field data in terms of specific species content in the lunar atmosphere, the following total count measurements, $T_i(\lambda,h,t_i)$, must be performed:

$T_1(\lambda_r,h,t_1)$ = the total counts measured for the experimental configuration

TABLE 8

WEATHER DATA FOR ALBUQUERQUE, N.M. PREVIOUSLY AT 2300 MST*

Nov. Date	Cloudiness (In 8ths)	Cloud Type	Visibility (Miles)
11/14/66	0	None	> 10
11/15/66	0	None	> 10
11/16/66	0	None	> 10
11/17/66	7	Cirrus	> 10
11/18/66	2	Cirrus	> 10
11/19/66	0	None	> 10
11/20/66	6	Cirrus	> 10
11/21/66	0	None	> 10
11/22/66	8	Altocumulus	> 10
11/23/66	8	Altostratus	> 10
11/24/66	7	Stratocumulus, Altocumulus, Cirrus	> 10
11/25/66	8	Altocumulus	> 10
11/26/66	0	None	> 10
11/27/66	0	None	> 10
11/28/66	1	Cirrus	> 10
11/29/66	0	None	> 10
11/30/66	0	None	> 10

*Data taken from Daily Weather Map published by The Environmental Science Services Administration of the U.S. Department of Commerce.

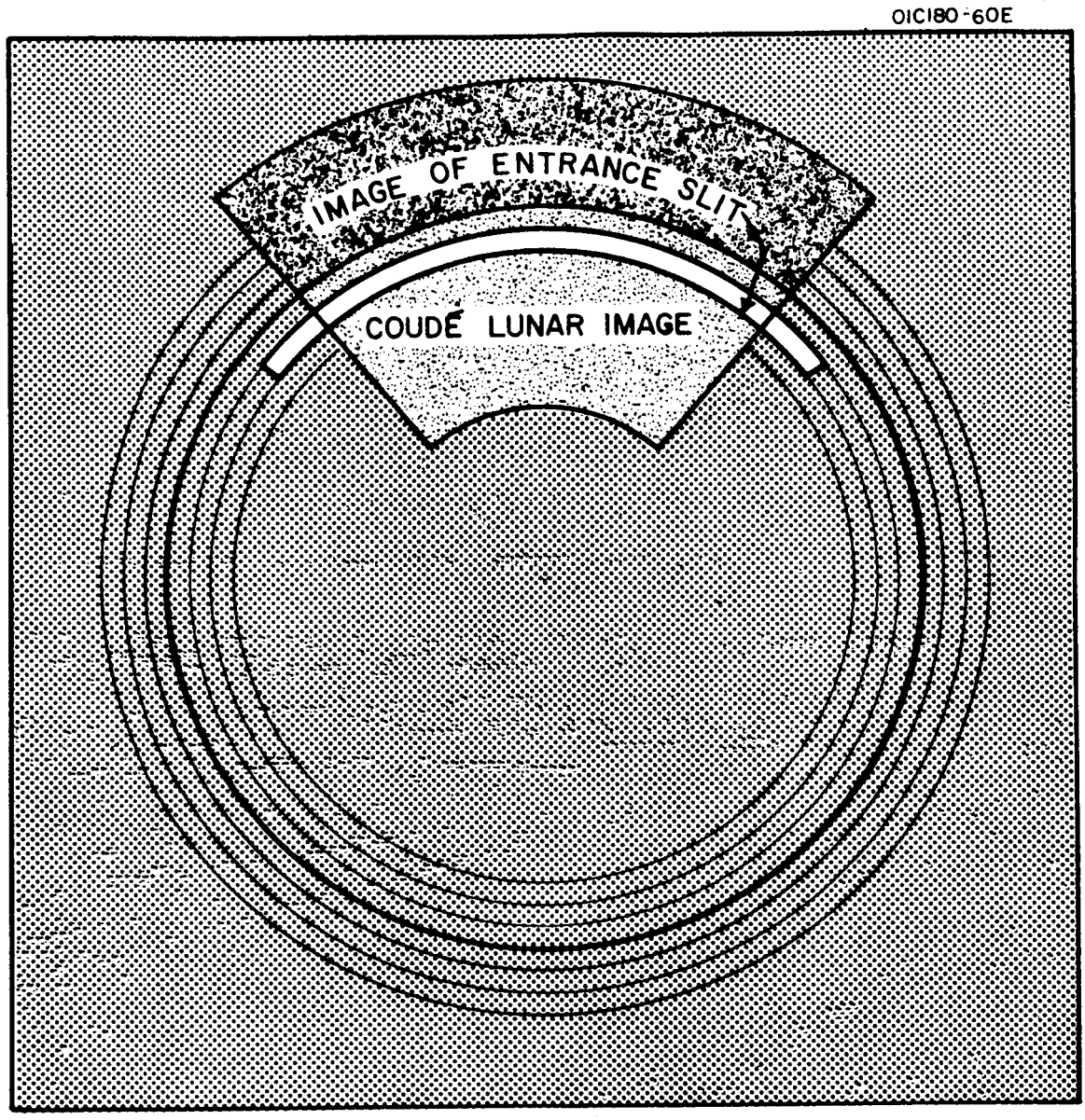

Figure 17. Guidance mask configuration for acquisition of lunar surface brightness data counts.

where:

(a) the spectrometer slit is centered precisely at the species resonance wavelength, λ_r,

(b) the observation is performed above the lunar limb with the disc overocculted by 100 km and with the fixed slit jaw set at a position corresponding to "h" kilometers above the lunar limb (see Figure 15 where h = 200 km)

(c) the time required to obtain the total count measured for this configuration is t_1.

$T_2(\lambda_r,h,t_2)$ = the total counts measured for the experimental configuration

where:

(a) $\lambda = \lambda_r$

(b) the observation is performed below the lunar limb with the occulting disc removed and with the fixed slit jaw set at a position corresponding to "h" kilometers below the lunar limb. For the sake of uniformity, all of the $T_2(\lambda_r,h,t_2)$ measurements reported herein were performed with an h-value of -200 km (see Figure 17 where h = 200 km)

(c) $t = t_2$

$T_3(\lambda_b,h,t_3)$ = the total counts measured for the experimental configuration

where:

(a) the spectrometer slit is centered at the background wavelength, λ_b (which, for all cases, was ±5.0Å removed from λ_r),

(b) the observation is performed in a manner identical to that described for measuring T_1 employing matching h-values,

(c) $t = t_3$

$T_4(\lambda_b,h,t_4)$ = the total counts measured for the experimental configuration

where:

(a) $\lambda = \lambda_b$

(b) the observation is performed in a manner identical to that described for measuring T_2.

(c) $t = t_4$

$T_5(t_5)$ = the total measured counts due to thermal electrons integrated over a time, t_5

For each individual species investigated, the set of five total count measurements defined above was obtained. Additionally, for each species it was desirable to perform the $T_1(\lambda_r,h,t_1)$- and $T_3(\lambda_b,h,t_3)$-measurements at more than one h-value. If positive experimental results were obtained, these additional data would yield information on the distribution of the species in the lunar atmosphere whereas if negative results were obtained, these additional data would serve as a further check on the procedure employed. In the present field program, the T_1 and T_3 measurements were performed at h-values of 200 and 100 km for each species.

Thus, in accordance with the above discussion, each species determination required a set consisting of seven individual total count measurements.

Procedure for Data Acquisition. The instrumentation system was in a standby status at 1900 hours on the evening of 26 November 1966 when acceptable seeing conditions prevailed so that experimental data were obtained for three species: Na, Ca, and Ca^+. It was convenient to perform the required total count measurements for each species in the following order: T_1, T_2, T_3, T_4. For a given species investigation, a representative T_5 value was obtained by integrating the counts measured in several individual determinations performed at convenient intervals.

In the acquisition of the field data, extensive efforts were made to employ uniform procedures for each species determination. As such, the detailed procedural discussion which follows applies equally to all three species determinations. The following general experimental procedure was employed in the performance of the Na, Ca, and Ca^+ measurements reported herein. Since a steady-state condition prevailed for the PM tube, additional histogram analyses were performed to establish final representative discriminator levels and PM tube voltages. The discriminator level was adjusted to a thermal electron count rate of about one count per second to obtain a nominal uniform operational level. Under these conditions, the observation room light level was sufficiently low so that it did not constitute a significant source of interference. Additionally, on the basis of the guidance capability achieved, the total count measurements could be acquired in time sets of 15-second increments. In this manner, it was possible to verify the guidance configuration before and after each 15-second increment and also reject any increment set which was found to be contaminated by environmental variations beyond experimental control.

The entrance and exit slit widths were set at 0.33 mm. Then, a standard Na or Ca lamp was placed at the Coudé image plane in order to obtain an effective slit function and to locate and record the Veeder-Root counter value for λ_r. This function was performed in the manner described in Section III for the specific case of Na (see Figure 12). At this point, the spectrometer-coronagraph optical alignment was re-established and the

alignment and guidance mask (appropriate for the 26 November 1966 lunar image size; see Figure 13) was placed at the Coudé image focal plane. The high intensity light source behind the entrance slit was employed (in the manner previously described) to obtain the slit image-lunar image configuration shown in Figure 14. Minor adjustments were then made to the pre-established guidance Vernier settings on a trial-and-error basis until a final acceptable capability was established which permitted the desired slit image-lunar image configuration to be sustained for a period of minutes without noticeable drift. At this point, the occulting disc was positioned in accordance with the configuration shown in Figure 15 so that the lunar limb was overocculted by 100 km. This precaution minimized instrumental scatter and additionally insured that a small guidance drift would not result in lunar disc radiation spillage into the detector line-of sight which would contaminate the data. Now, the projected entrance slit image was positioned so that its fixed jaw corresponded to an altitude 200 km above the lunar limb while the adjustable jaw position corresponded to an altitude of about 235 km above the lunar limb since a slit width of 0.33 mm was employed (see Figure 15). The high intensity lamp behind the entrance slit was extinguished and moved out of position. At this point, the standard observation coronagraph lens was replaced by the freshly-cleaned 16-inch low-scatter observation coronagraph lens which was observed to produce a significant reduction in instrumental scatter. The prevalent configuration was employed to perform the T_1 measurements at altitudes of 200 and 100 km by appropriately varying the slit jaw position.

During the data acquisition procedure, a trained observer with a dark-adapted eye was employed to view into the coronagraph (with an eyepiece) at a point just beyond the edge of the occulting disc. In this manner, optimum sky conditions could be selected for data acquisition. When suitable sky and proper guidance conditions prevailed, data acquisition commenced in the form of total counts obtained during consecutive 15-second increments. The total measuring time achieved during any specific total count observation was dependent on the results of intermittent guidance checks. In general, the conditions that prevailed permitted three to six consecutive 15-second observation periods to be accumulated (i.e., 45 to 90 seconds total observation time) for the total count observations defined previously.

After performing the T_1 measurements at altitudes of 100 and 200 km, the T_2 measurements were performed as follows. The occulting disc was removed and the entrance slit was back-illuminated to achieve the required slit image-lunar image configuration wherein the fixed slit jaw was now positioned 200 km below the lunar limb as shown in Figure 17. In general, precise guidance was not required for performing these lunar surface measurements. However, when necessary, small adjustments were made to the vernier settings as required. At this point, the T_2 measurements were performed using similar 15-second increments as in the case of the T_1 observations. An additional precautionary measurement was performed as follows. First, while the slit image-lunar image configuration was sustained, the

occulting disc was placed in the position whereby it overocculted the lunar limb by 100 km. Data counts were obtained whereby the spectrometer slit now viewed the back of the occulting disc. In all cases, the resultant signal amounted to about one count per second which was essentially that observed for the thermal electron count. This particular measurement was included in the performance of all T_2 and T_4 data acquisition runs.

The entire procedure described above is directly applicable to the similar cases of T_3 and T_4 except that the spectrometer spectral setting is positioned at the background wavelength, λ_b. The specific λ_b-values employed were 5885.0Å, 4231.8Å, and 3938.7Å for Na, Ca, and Ca^+, respectively.

The application of the above-outlined procedure to the acquisition of the Na, Ca, and Ca^+ data resulted in the various total count observations presented in Tables 9, 10, and 11, respectively.

The data analysis to be described in Section V involves $C_i(\lambda,h)$-values defined as

$$C_i(\lambda,h) = \left[\frac{T_i(\lambda,h,t_i)}{t_i} - \frac{T_5(t_5)}{t_5}\right] \qquad (11)$$

so that $C_i(\lambda,h)$ represents the experimental value for the counts per second as evaluated from the appropriate $T_i(\lambda,h,t_i)$ and $T_5(t_5)$ measurements as indicated in Tables 9, 10, and 11. Thus, the experimental configuration employed to obtain a specific $C_i(\lambda,h)$-value is derived from the description applicable to the corresponding $T_i(\lambda,h,t_i)$ measurement.

The observed experimental data summarized in Tables 9, 10, and 11 were employed to evaluate the corresponding $C_i(\lambda,h)$-values for the constituents Na, Ca, and Ca^+. These values, presented in Tables 12, 13, and 14, respectively, are utilized in the data analysis and interpretation discussions in the following section.

TABLE 9

MEASURED $T_i(\lambda,h,t_i)$- AND $T_5(t_5)$-VALUES FOR SODIUM

Experimental Parameter	Parameter Specification	Measured Total Counts
$T_1(\lambda_r,h,t_1)$	T_1(5890.0Å, 200 km, 90 sec)	238
	T_1(5890.0Å, 100 km, 90 sec)	227
$T_2(\lambda_r,h,t_2)$	T_2(5890.0Å, -200 km, 45 sec)	311,257
$T_3(\lambda_b,h,t_3)$	T_3(5885.0Å, 200 km, 60 sec)	175
	T_3(5885.0Å, 100 km, 60 sec)	169
$T_4(\lambda_b,h,t_4)$	T_4(5885.0Å, -200 km, 45 sec)	426,749
$T_5(t_5)$	T_5(135 sec)	155

TABLE 10

MEASURED $T_i(\lambda, h, t_i)$- AND $T_5(t_5)$-VALUES FOR CALCIUM

Experimental Parameter	Parameter Specification	Measured Total Counts
$T_1(\lambda_r, h, t_1)$	T_1(4226.8Å, 200 km, 60 sec)	144
	T_1(4226.8Å, 100 km, 45 sec)	106
$T_2(\lambda_r, h, t_2)$	T_2(4226.8Å, -200 km, 45 sec)	393,751
$T_3(\lambda_b, h, t_3)$	T_3(4231.8Å, 200 km, 45 sec)	164
	T_3(4231.8Å, 100 km, 45 sec)	168
$T_4(\lambda_b, h, t_4)$	T_4(4231.8Å, -200 km, 45 sec)	846,221
$T_5(t_5)$	T_5(120 sec)	135

TABLE 11

MEASURED $T_i(\lambda,h,t_i)$- AND $T_5(t_5)$-VALUES FOR CALCIUM IONS

Experimental Parameter	Parameter Specification	Measured Total Counts
$T_1(\lambda_r,h,t_1)$	T_1(3933.7Å,200 km,45 sec)	93
	T_1(3933.7Å,100 km,60 sec)	122
$T_2(\lambda_r,h,t_2)$	T_2(3933.7Å,-200 km,45 sec)	287,202
$T_3(\lambda_b,h,t_3)$	T_3(3938.7Å,200 km,45 sec)	169
	T_3(3938.7Å,100 km,45 sec)	176
$T_4(\lambda_b,h,t_4)$	T_4(3938.7Å,-200 km,45 sec)	860,027
$T_5(t_5)$	T_5(120 sec)	131

TABLE 12

DERIVED $C_i(\lambda,h)$-VALUES FOR SODIUM

Experimental Parameter	Parameter Specification	Derived Values of Counts/Sec
$C_1(\lambda_r,h)$	C_1(5890.0Å,200 km)	1.49
	C_1(5890.0Å,100 km)	1.37
$C_2(\lambda_r,h)$	C_2(5890.0Å,-200 km)	6.92(3)*
$C_3(\lambda_b,h)$	C_3(5855.0Å,200 km)	1.77
	C_3(5855.0Å,100 km)	1.67
$C_4(\lambda_b,h)$	C_4(5855.0Å,-200 km)	9.48(3)

*The number in parentheses indicates the power of ten.

TABLE 13

DERIVED $C_i(\lambda,h)$-VALUES FOR CALCIUM

Experimental Parameter	Parameter Specification	Derived Values of Counts/Sec
$C_1(\lambda_r,h)$	C_1(4226.8Å,200 km)	1.27
	C_1(4226.8Å,100 km)	1.23
$C_2(\lambda_r,h)$	C_2(4226.8Å,-200 km)	8.75(3)*
$C_3(\lambda_b,h)$	C_3(4231.8Å,200 km)	2.51
	C_3(4231.8Å,100 km)	2.60
$C_4(\lambda_b,h)$	C_4(4231.8Å,-200 km)	18.8(3)

*The number in parentheses indicates the power of ten.

TABLE 14

DERIVED $C_i(\lambda,h)$-VALUES FOR CALCIUM IONS

Experimental Parameter	Parameter Specification	Derived Values of Counts/Sec
$C_1(\lambda_r,h)$	C_1(3933.7Å,200 km)	0.98
	C_1(3933.7Å,100 km)	0.94
$C_2(\lambda_r,h)$	C_2(3933.7Å,-200 km)	6.38(3)*
$C_3(\lambda_b,h)$	C_3(3938.7Å,200 km)	2.67
	C_3(3938.7Å,100 km)	2.82
$C_4(\lambda_b,h)$	C_4(3938.7Å,-200 km)	19.1(3)

*The number in parentheses indicates the power of ten.

V. DATA ANALYSIS AND INTERPRETATION

The analysis and interpretation of the experimental results presented in Tables 12, 13, and 14 involves an equation of the general form:

$$N(\lambda_r,h) = [X(\lambda_r,h)]\ Y(\lambda_r) \qquad (12)$$

where

$N(\lambda_r,h)$ = the experimentally determined cm^2-column count of a given species with a resonance signature radiation wavelength, λ_r. Additionally, the observation is performed along a line-of-sight which is tangent to the lunar altitude, h*.

$[X(\lambda_r,h)] = \left[\frac{C_1(\lambda_r,h)}{C_2(\lambda_r,h)} - \frac{C_3(\lambda_b,h)}{C_4(\lambda_b,h)}\right]$ where the $C_i(\lambda,h)$-values are defined by Equation (11).

$Y(\lambda_r)$ = a product of various parameters which are not determined experimentally.

Thus, the form of Equation (12) allows the discussion of the $N(\lambda_r,h)$ determination in terms of two major components: $[X(\lambda_r,h)]$ determined on the basis of experimental measurements, and $Y(\lambda_r)$ which is derived from other sources. On the basis of a subsequent experimental error analysis, it is concluded that the random error component is a significant factor in the present data analysis problem. The magnitude of the random error component can be evaluated by first assuming that the photoelectron distribution is Poisson so that $\sigma[X(\lambda_r,h)]$ can be interpreted in terms of the standard deviation which is evaluated by the straightforward application of measurement statistics. On this basis, interpretation of the experimental results involves the more general equation

$$N(\lambda_r,h) = \left(X(\lambda_r,h) \pm \sigma[X(\lambda_r,h)]\right) Y(\lambda_r)\ . \qquad (13)$$

The data interpretation which is predicated upon the above equation yields meaningful, upper limit $[N(\lambda_r,h)]$-values for the three investigated lunar constituents. In the following discussion, the individual parameters

*This interpretation of Equation (12) assumes implicitly that the resonance scattering material is optically thin and that the resultant flux is isotropic. For the cases involved (Na, Ca, and Ca^+), the latter assumption is not strictly true. However, the departures from isotropicity [49,65] can be shown to be negligibly small compared to the random and systematic errors involved in the present measurements.

involved in the $Y(\lambda_r)$ function are identified and evaluated from available data. The magnitude of the random error component, $\sigma[X(\lambda_r,h)]$, associated with the several measured $X(\lambda_r,h)$-values is then evaluated. Finally, the experimental results are interpreted using Equation (13) to derive upper limit $N(\lambda_r,h)$-values.

The individual count rate $C_i(\lambda_r,h)$-values of Tables 12, 13, and 14 can be defined by the following general equations:

$$C_1(\lambda_r,h) = K(\lambda)A_s \left[\Phi_h(\lambda_r) + \int_{\lambda_1}^{\lambda_2} \Phi_1(\lambda_r,h)\, s_i(\lambda_r)\, d\lambda \right] \tag{14}$$

$$C_2(\lambda_r,h) = K(\lambda)A_s \int_{\lambda_1}^{\lambda_2} \Phi_2(\lambda_r,h)\, s_i(\lambda_r)\, d\lambda \tag{15}$$

$$C_3(\lambda_b,h) = K(\lambda)A_s \int_{\lambda_3}^{\lambda_4} \Phi_3(\lambda_b,h)\, s_i(\lambda_b)\, d\lambda \tag{16}$$

$$C_4(\lambda_b,h) = K(\lambda)A_s \int_{\lambda_3}^{\lambda_4} \Phi_4(\lambda_b,h)\, s_i(\lambda_b)\, d\lambda \ . \tag{17}$$

where:

$K(\lambda)A_s$ = an overall instrumentation efficiency factor wherein the $K(\lambda)$-value involves a number of parameters, several of which are variable with wavelength, and the A_s-value which is equivalent to the projected area subtended at the lunar surface by the spectrometer entrance slit (i.e., in the present case a slit width of 0.3 mm subtended about 35 km at the moon). The assumption of a constant A_s-value herein is valid since a homogeneous radiation field was observed throughout the subtended area during full moon conditions. Although the $K(\lambda)A_s$-values are not involved in the data analysis, it is of interest to note here that the following values have been calculated from Equation (17):

$$[K(\lambda)A_s]^{-1}\ (5885.0\text{Å}) = 6.6 \times 10^9 \left(\frac{\text{photons cm}^{-2}\ \text{sec}^{-1}}{\text{counts sec}^{-1}}\right)$$

$$[K(\lambda)A_s]^{-1}\ (4231.8\text{Å}) = 8.8 \times 10^8 \left(\frac{\text{photons cm}^{-2}\ \text{sec}^{-1}}{\text{counts sec}^{-1}}\right)$$

$$[K(\lambda)A_s]^{-1}\ (3938.7\text{Å}) = 7.9 \times 10^8 \left(\frac{\text{photons cm}^{-2}\ \text{sec}^{-1}}{\text{counts sec}^{-1}}\right)$$

$\Phi_h(\lambda_r)$ = the signal emission rate (photons/cm^2-column-sec) due to the solar-illuminated lunar species resonance radiation, λ_r.

$\Phi_1(\lambda_r,h)$ = the equivalent spectral emission rate (photons/cm^2-sec-Å) from background scattering in the spectral interval between λ_1 to λ_2 and centered at λ_r.

$\Phi_2(\lambda_r,h)$ = the equivalent spectral emission rate (photons/cm^2-sec-Å) from lunar surface radiation in the spectral region centered at λ_r. It should be noted that the designation of a constant value for this parameter is justified under full moon conditions. Under other conditions, an appropriate area integral would be required since $\Phi_2(\lambda_r,h)$ would be variable over the illuminated region.

$\Phi_3(\lambda_b,h)$ = the equivalent spectral emission rate (photons/cm^2-sec-Å) from background scattering in the spectral interval between λ_3 to λ_4 and centered at λ_b.

$\Phi_4(\lambda_b,h)$ = the equivalent spectral emission rate (photons/cm^2-sec-Å) from lunar surface radiation in the wavelength interval centered at λ_b.

$s_i(\lambda_{r,b})$ = the triangular slit function with: (1) a base width of (λ_2 - λ_1) centered at λ_r or (2) a base width of (λ_4 - λ_3) centered at λ_b. In the present investigation, this function was determined experimentally as discussed subsequently in greater detail.

The integral terms of Equations (14) through (17) are required since the solar flux exhibits significant variations over the system spectral bandpasses. Additionally, in Equation (15), an additive term involving the resonance signal flux has not been included since its contribution can be considered negligible compared to the lunar surface emission rate. Finally, in the above treatment, it is assumed that the $K(\lambda)$-value has not varied appreciably during the time required to perform the set of total count measurements involved in a single species determination.

In the following analytic treatment, it is convenient to form the ratios of Equations (14) to (15) and Equations (16) to (17) which result in the following expressions:

$$\frac{C_1(\lambda_r,h)}{C_2(\lambda_r,h)} = \frac{\left[\Phi_h(\lambda_r) + \int_{\lambda_1}^{\lambda_2} \Phi_1(\lambda_r,h)\, s_i(\lambda_r)\, d\lambda\right]}{\int_{\lambda_1}^{\lambda_2} \Phi_2(\lambda_r,h)\, s_i(\lambda_r)\, d\lambda} \tag{18}$$

and

$$\frac{C_3(\lambda_b,h)}{C_4(\lambda_b,h)} = \frac{\int_{\lambda_3}^{\lambda_4} \Phi_3(\lambda_b,h)\, s_i(\lambda_b)\, d\lambda}{\int_{\lambda_3}^{\lambda_4} \Phi_4(\lambda_b,h)\, s_i(\lambda_b)\, d\lambda} \quad . \tag{19}$$

It should be noted that the experimentally determined C_3/C_4-value is equivalent to the S-value employed in Figure 3 to evaluate the role of seeing conditions in the field experiments.* In the following analysis, it is assumed that performance of the measurement set for a given species was accomplished without significant variation of instrumental parameters or seeing conditions; therefore, it follows that:

$$\frac{C_3(\lambda_b,h)}{C_4(\lambda_b,h)} = \frac{\int_{\lambda_1}^{\lambda_2} \Phi_1(\lambda_r,h)\, s_i(\lambda_r)\, d\lambda}{\int_{\lambda_1}^{\lambda_2} \Phi_2(\lambda_r,h)\, s_i(\lambda_r)\, d\lambda} \quad . \tag{20}$$

*In accordance with the results of Tables 12, 13, and 14 for the evening of 26 November 1966, the following S-values prevailed at Sacramento Peak: S(5885.0Å) 1.8×10^{-4}, S(4231.7Å) 1.4×10^{-4} and S(3938.7Å) 1.5×10^{-4}.

Substitution of Equation (20) into Equation (18) yields

$$\left[\frac{C_1(\lambda_r,h)}{C_2(\lambda_r,h)} - \frac{C_3(\lambda_b,h)}{C_4(\lambda_b,h)}\right] = \frac{\Phi_h(\lambda_r)}{\int_{\lambda_1}^{\lambda_2} \Phi_2(\lambda_r,h)\, s_i(\lambda_r)\, d\lambda} \quad . \tag{21}$$

The left-hand side of Equation (21) represents the $[X(\lambda_r,h)]$-function of Equation (12) whereas the right-hand side includes the $N(\lambda_r,h)$-and $Y(\lambda_r)$-functions. The numerator of the above expression can be expanded in the following manner

$$\Phi_h(\lambda_r) = PN(\lambda_r,h) = \alpha\, F_s(\lambda_r)\, N(\lambda_r,h) \tag{22}$$

where $F_s(\lambda_r)$ represents the solar flux value pertinent to the specific wavelength, λ_r ; the other parameters have been defined previously (see Table 2 for the appropriate P- and α-values). Rewriting Equation (21) using the above expression yields

$$N(\lambda_r,h) = \left[\frac{C_1}{C_2} - \frac{C_3}{C_4}\right] \left(\frac{1}{\alpha\, F_s(\lambda_r)}\right) \int_{\lambda_1}^{\lambda_2} \Phi_2(\lambda_r,h)\, s_i(\lambda_r)\, d\lambda \quad . \tag{23}$$

The integral on the right-hand side of Equation (23) can be evaluated analytically as follows. The equivalent spectral lunar emission rate, $\Phi_2(\lambda_r,h)$, is geometrically related to the lunar spectral illumination at the top of the earth's atmosphere, $F_m(\lambda)$ [photons/cm^2-sec-Å], by

$$\Phi_2(\lambda_r,h) = \frac{4\pi D^2\, F_m(\lambda)}{A_m} \tag{24}$$

where

A_m = the projected area of the lunar disc

D = the earth-moon distance.

Additionally, the lunar spectral illumination is related to the solar spectral illumination by

$$F_m(\lambda) = \rho(\lambda)\, F_s(\lambda) \tag{25}$$

where

$\rho(\lambda)$ = a parameter involving the lunar reflectivity which exhibits a relatively moderate variation with wavelength. As such, it has been assumed to be constant over the narrow 5Å spectral separation between $[(\lambda_4 - \lambda_3)$ and $(\lambda_2 - \lambda_1)]$ involved in a single species determination.

It is now convenient to define a solar flux function, $f(\lambda_i)$, as the ratio of the solar spectral illumination value at the wavelength λ_i, $F_s(\lambda_i)$, to the value at the specific resonance wavelength λ_r, $F_s(\lambda_r)$:

$$F_s(\lambda_i) = F_s(\lambda_r)\ f(\lambda_i)\ . \tag{26}$$

Substitution of Equations (24) and (26) into Equation (23) yields the following expression:

$$N(\lambda_r,h) = \left[\frac{C_1}{C_2} - \frac{C_3}{C_4}\right]\left[\frac{4\pi D^2\ \rho(\lambda)}{A_m\ \alpha}\right]\int_{\lambda_1}^{\lambda_2} f(\lambda_i)\ s_i(\lambda_r)\ d\lambda\ . \tag{27}$$

The integral in the above equation can be calculated numerically by convolving the published values of $f(\lambda_i)$ [44] with the experimentally measured slit function shown in Figure 12. Designating this calculated value by the symbol, $\Delta\lambda_r$, the final expression may be written as:

$$N(\lambda_r,h) = \left[\frac{C_1(\lambda_r,h)}{C_2(\lambda_r,h)} - \frac{C_3(\lambda_b,h)}{C_4(\lambda_b,h)}\right]\left[\frac{4\pi D^2\ \rho(\lambda)\ \Delta\lambda_r}{A_m\ \alpha}\right] = [X(\lambda_r,h)]\ Y(\lambda_r). \tag{28}$$

In the following discussion, the individual parameters involved in the calculation of $Y(\lambda_r)$ are evaluated for each of the three species determinations.

Determination of $Y(\lambda_r)$-Values

With respect to the ratio $4\pi D^2/A_m$, the A_m-value is a constant which involves the lunar diameter, 3.47×10^3 km, as quoted in the American Ephemeris [66] whereas the D-value is variable since it represents the earth-moon distance which prevails for a given date. For 26 November 1966, the appropriate D-value of 3.97×10^5 km was obtained from published information [66]. Although the derived D-value refers to an observation performed at Greenwich which necessitates a slight correction for application to the Sacramento Peak site, it turns out that the maximum correction involved was less than 0.3 percent so that it was neglected.

With respect to the $\rho(\lambda)$-parameter of Equation (28), three values have been derived on the basis of published experimental data [67] for $F_s(\lambda)$, $F_m(\lambda)$, and the relative spectral reflectivity of the lunar surface as a function of wavelength, $R_m(\lambda)$. The $F_m(\lambda)$- and $R_m(\lambda)$-values pertain to full moon conditions and are therefore directly applicable to the present experimental situation. The measurements were performed for $\lambda\lambda$ 3100 to 5300Å with a relatively-broad spectral bandpass which varied between 10 and 30Å. These data were normalized over an equivalently large spectral bandpass in the vicinity of 4510Å where examination of the Minnaert table [44] indicated that the solar spectrum was relatively free from absorption line structure over an interval of about 20Å. The published $\rho(4510\text{Å})$ value was 2.8×10^{-6} which, when combined with published $R_m(\lambda)$-values, resulted in the $\rho(\lambda_r)$-values presented in Table 15.

TABLE 15

DERIVED VALUES FOR SELECTED PARAMETERS

Species	$\frac{4\pi D^2}{A_m}$	$\rho(\lambda)$	$\Delta\lambda_r$ (cm)	$\frac{1}{\alpha}$ (cm^{-3})	$Y(\lambda_r)$-value (cm^{-2})
Na(5890.0Å)	2.09 (5)*	3.2 (-6)†	8.95 (-8)	4.26 (20)	2.55 (13)
Ca(4226.8Å)	2.09 (5)	2.6 (-6)	14.20 (-8)	4.25 (20)	3.28 (13)
Ca^+(3933.7Å)	2.09 (5)	2.3 (-6)	2.90 (-8)	8.77 (20)	1.22 (13)

*The value in parentheses is the power of ten.

†This value is estimated [67] from 5300Å.

In accordance with a previous discussion, it has been shown that

$$\Delta\lambda = \int_{\lambda_1}^{\lambda_2} f(\lambda_i)\, s_i(\lambda_r)\, d\lambda \qquad (29)$$

where

$$f(\lambda_i) = F_s(\lambda_i)/F_s(\lambda_r)$$

$s_i(\lambda_r)$ = the effective slit function over the spectral interval centered at λ_r.

In practice, the $\Delta\lambda_r$-values were calculated numerically by approximating Equation (29) by

$$\Delta\lambda_r = \sum_i f(\lambda_i)\, s_i(\lambda_r)\, \delta\lambda \,. \qquad (30)$$

The $f(\lambda_i)$ function is defined in terms of the spectral data presented in Figures 18, 19, and 20 which have been reproduced from Minnaert tables [44]. Furthermore, $s_i(\lambda_r)$ represents the instrumental slit function (normalized to unity at the peak transmission wavelength, λ_r) as determined on the basis of a laboratory calibration and indicated in Figure 12. In the numerical analysis, the summation was performed over $\delta\lambda$-increments of 0.05Å owing to the structurally complex spectral patterns that prevail in these spectral regions.

Finally in the $Y(\lambda_r)$ evaluation, the $1/\alpha$-values have been presented previously in Table 2. The individually derived parameters comprising the $Y(\lambda_r)$-values have been grouped for the sake of convenience in Table 15.

From Equation (12), it would appear that the calculated $Y(\lambda_r)$-values and the corresponding measured $X(\lambda_r,h)$-values could be combined as indicated to obtain experimental estimates of $N(\lambda_r,h)$ for the three species investigated. This procedure is clearly valid for the case where $[X(\lambda_r,h)] \gg \sigma[X(\lambda_r,h)]$. However, it will be shown that in all cases involved in the present analysis, $X(\lambda_r,h) < \sigma[X(\lambda_r,h)]$. As such, the present analysis involves evaluation of both $[X(\lambda_r,h)]$ and $\sigma[X(\lambda_r,h)]$ as specified in Equation (13), i.e.

$$N(\lambda_r,h) = \Big(X(\lambda_r,h) \pm \sigma[X(\lambda_r,h)]\Big)\, Y(\lambda_r) \,. \qquad (13)$$

Determination of the Required $\Big(X(\lambda_r,h) \pm \sigma[X(\lambda_r,)]\Big)$-Values. In accordance with previous discussions,

$$X(\lambda_r,h) \pm \sigma[X(\lambda_r,h)] = \left[\frac{C_1(\lambda_r,h)}{C_2(\lambda_r,h)} - \frac{C_3(\lambda_b,h)}{C_4(\lambda_b,h)}\right] \pm \sigma\left[\frac{C_1(\lambda_r,h)}{C_2(\lambda_r,h)} - \frac{C_3(\lambda_b,h)}{C_4(\lambda_b,h)}\right]. \qquad (31)$$

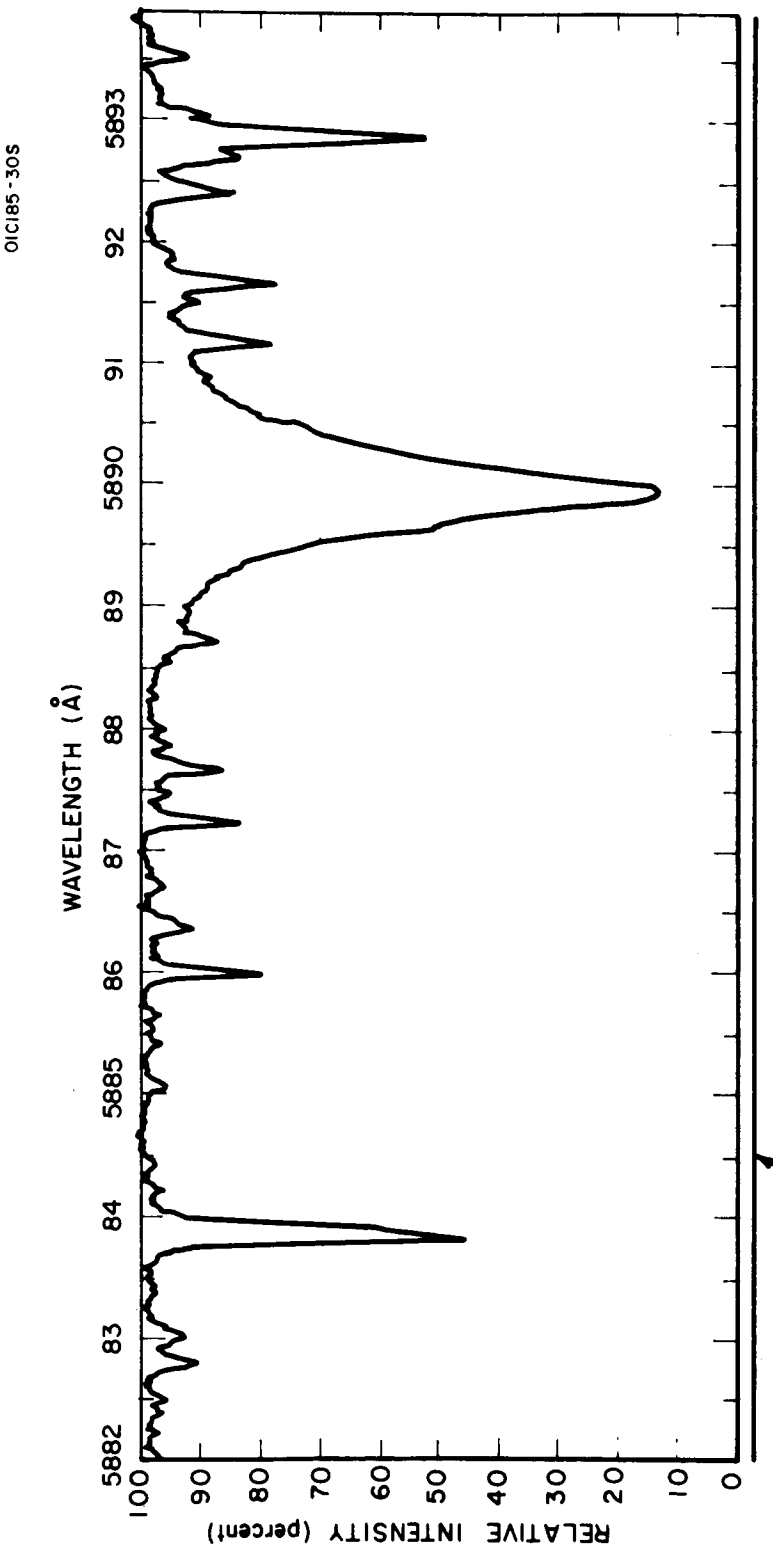

Figure 18. Solar spectrum [44] in the vicinity of Na, λ_r (5890.0Å).

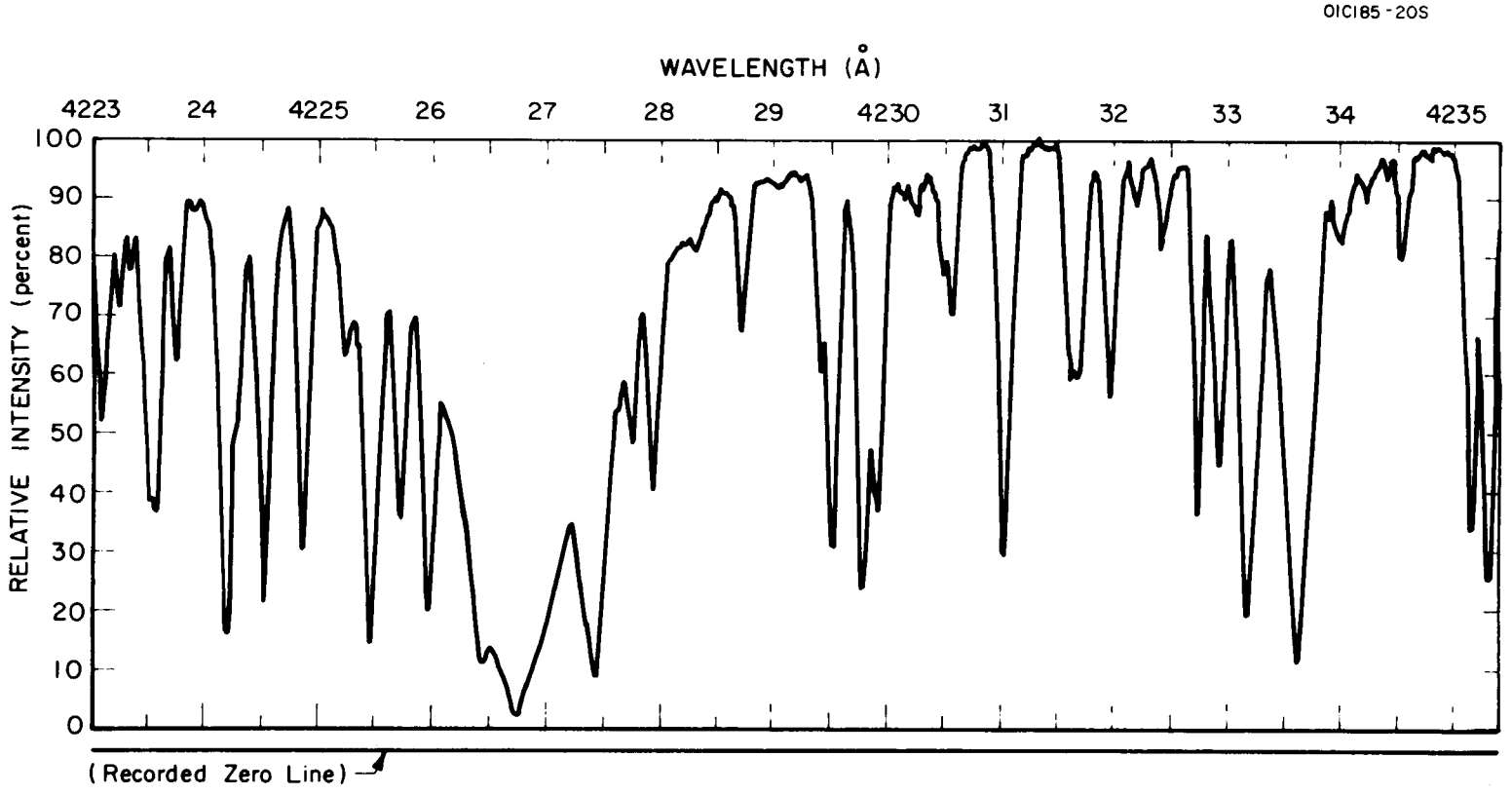

Figure 19. Solar spectrum [44] in the vicinity of Ca, λ_r (4226.8Å).

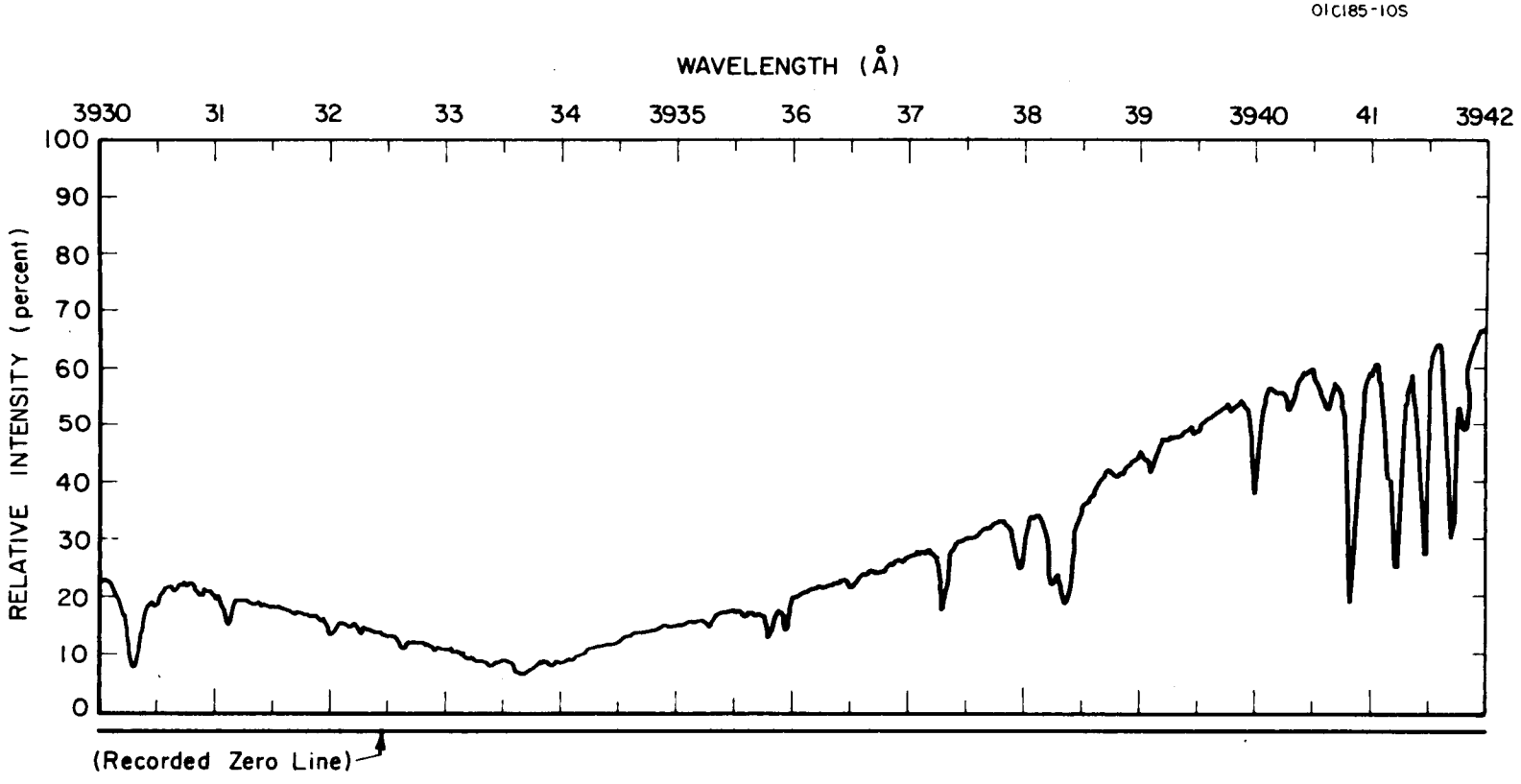

Figure 20. Solar spectrum [442 in the vicinity of Ca^{+}, λ_r (3933.7Å).

Application of the law of propagation of errors [68] allows the standard deviation to be expressed in the following convenient form:

$$\sigma\left[X(\lambda_r,h)\right] = \left\{\frac{C_1^2}{C_2^2}\left[\frac{\sigma^2(C_1)}{C_1^2} + \frac{\sigma^2(C_2)}{C_2^2}\right] + \frac{C_3^2}{C_4^2}\left[\frac{\sigma^2(C_3)}{C_3^2} + \frac{\sigma^2(C_4)}{C_4^2}\right]\right\}^{1/2} . \quad (32)$$

With respect to the present results, a cursory examination of the tabulated data indicates that in all cases:

$$\frac{\sigma^2(C_2)}{C_2^2} \ll \frac{\sigma^2(C_1)}{C_1^2}$$

and

$$\frac{\sigma^2(C_4)}{C_4^2} \ll \frac{\sigma^2(C_3)}{C_3^2}$$

so that

$$\sigma[X(\lambda_r,h)] \simeq \left(\frac{\sigma^2(C_1)}{C_2^2} + \frac{\sigma^2(C_3)}{C_4^2}\right)^{1/2} . \quad (33)$$

It is desirable at this point to express Equation (33) in terms of the data presented previously in Tables 9 through 14.

The total count measurements (which are assumed to be described by a Poisson distribution in time) can be expressed by

$$T_i(\lambda,h,t_i) \pm \sigma[T_i(\lambda,h,t_i)] = T_i(\lambda,h,t_i) \pm \sqrt{T_i(\lambda,h,t_i)} \quad (34)$$

and

$$T_5(t_5) \pm \sigma[T_5(t_5)] = T_5(t_5) \pm \sqrt{T_5(t_5)} \quad (35)$$

where

$T_i(\lambda,h,t_i)$ = the total count measurement

$\sigma[T_i(\lambda,h,t_i)]$ = $\sqrt{T_i(\lambda,h,t_i)}$ which is the standard deviation ascribed to, $T_i(\lambda,h,t_i)$

$T_5(t_5)$ = the total thermal counts

$\sigma[T_5(t_5)]$ = $\sqrt{T_5(t_5)}$ which is the standard deviation ascribed to $T_5(t_5)$.

Thus, from Equation (11):

$$C_i(\lambda,h) \pm \sigma[C_i(\lambda,h)] = \left[\frac{T_i(\lambda,h,t_i)}{t_i} - \frac{T_5(t_5)}{t_5}\right] \pm \left[\frac{\sigma^2[T_i(\lambda,h,t_i)]}{t_i^2} + \frac{\sigma^2[T_5(t_5)]}{t_5^2}\right]^{1/2} \quad (36)$$

where

$C_i(\lambda,h)$ = derived counting rate

$\sigma[C_i(\lambda,h)]$ = the standard deviation for the derived $C_i(\lambda,h)$ - value.

Thus, substitution of Equation (36) into (33) yield:

$$\sigma[X(\lambda_r,h)] = \left[\frac{1}{C_2^2}\left(\frac{T_1}{t_1^2} + \frac{T_5}{t_5^2}\right) + \frac{1}{C_4^2}\left(\frac{T_3}{t_3^2} + \frac{T_5}{t_5^2}\right)\right]^{1/2} . \quad (37)$$

The appropriate parameters presented in Tables 9 through 14 inclusive were employed to evaluate the $\left(X(\lambda_r,h) \pm \sigma[X(\lambda_r,h)]\right)$ - values for Na,Ca, and Ca^+, respectively; the results are presented in Table 16.

TABLE 16

VALUES OF $X(\lambda_r,h)$ AND $\sigma[X(\lambda_r,h)]$ FOR Na, Ca, AND Ca^+ AT LUNAR OBSERVATION ALTITUDES OF 100 AND 200 KM

Species	$X(\lambda_r,100\ km) \pm \sigma[X(\lambda_r,100\ km)]$	$X(\lambda_r,200\ km) \pm \sigma[X(\lambda_r,200\ km)]$
Na	$(2.2 \pm 3.7) \times 10^{-5}$	$(2.8 \pm 3.8) \times 10^{-5}$
Ca	$(0.3 \pm 3.3) \times 10^{-5}$	$(1.1 \pm 3.0) \times 10^{-5}$
Ca^+	$(-0.1 \pm 3.6) \times 10^{-5}$	$(1.4 \pm 4.0) \times 10^{-5}$

Data Interpretation

In accordance with previous discussions, it can be seen from the magnitudes of the derived experimental values of Table 16 that $X(\lambda_r,h) < \sigma[X(\lambda_r,h)]$ for all cases which signifies that the random error associated with the set of measurements employed to derive the X-parameter exceeds the derived value of the parameter itself. Under these conditions, the question arises as to the basic validity associated with the derived X-values. In this regard, it is instructive at this juncture to consider both the random and systematic error components associated with the performance of the present experiment. As noted previously, the random error in the derived X-parameter has been evaluated by application of measurement statistics to derive the $\sigma(X)$-values of Table 16. Alternatively, the magnitude of the systematic error component cannot be assessed analytically, although a qualitative discussion of its contribution in the present experiment is presented below. First, a comparison of Equations (11) and (37) demonstrates the relatively high insensitivity of the $\sigma(X)$-value to the presence of systematic errors in the experimental loop as compared to the situation with respect to the X-parameter. This is emphasized further by reference to Table 16 where it can be seen that in all cases, $X(\lambda_r, 200 \text{ km}) > X(\lambda_r, 100)$ which represents physically unacceptable results requiring negative lunar atmospheric scale heights. As a result of the above discussion, no physical significance has been associated with the tabulated X-values of Table 16, and the remainder of the present data interpretation discussions which follow is predicated on the $\sigma(X)$-values.

The Determination of Upper Limit Species Values for Na, Ca, and Ca^+. The derived random error components, $\sigma[X(\lambda_r,h)]$, can be employed to derive corresponding upper limit values for $N(\lambda_r,h)$ based on the previous discussions. It should be noted that employment of the 1σ-values is associated with the classic statistical probability or confidence factor. As such the $\sigma(X)$-values of Table 16 were inserted into Equation (13) to obtain the following corresponding upper limit cm^2-column counts of the three species at the indicated lunar atmospheric measurement altitudes:

$$N(5890.0\text{Å}, 200 \text{ km}) = 9.7 \times 10^8/cm^2$$

$$N(5890.0\text{Å}, 100 \text{ km}) = 9.4 \times 10^8/cm^2$$

$$N(4226.8\text{Å}, 200 \text{ km}) = 9.8 \times 10^8/cm^2$$

$$N(4226.8\text{Å}, 100 \text{ km}) = 1.1 \times 10^9/cm^2$$

$$N(3933.7\text{Å}, 200 \text{ km}) = 4.9 \times 10^8 \ cm^2$$

$$N(3933.7\text{Å}, 100 \text{ km}) = 4.4 \times 10^8/cm^2 \ .$$

In accordance with a previous discussion presented in Section II regarding the maximum Na nighttime airglow signal (which was noted to be ≤ 200 Rayleighs), it can be seen that the above-listed N(Na)-values correspond

to a signal brightness of about 1.7 kiloRayleighs. As such, it is evident that the derived results were not influenced significantly by the presence of the Na night airglow.

The upper limit $N(\lambda_r,h)$-values can be employed to calculate corresponding local number density values, $n(\lambda_r,h)$, using Equation (3) as listed below:

$$n(5890.0\text{Å}, 200 \text{ km}) = 9.2 \text{ cm}^{-3}$$

$$n(5890.0\text{Å}, 100 \text{ km}) = 9.1 \text{ cm}^{-3}$$

$$n(4226.8\text{Å}, 200 \text{ km}) = 12 \text{ cm}^{-3}$$

$$n(4226.8\text{Å}, 100 \text{ km}) = 14 \text{ cm}^{-3}$$

$$n(3933.7\text{Å}, 200 \text{ km}) = 6.1 \text{ cm}^{-3}$$

$$n(3933.7\text{Å}, 100 \text{ km}) = 5.7 \text{ cm}^{-3}.$$

These above tabulations represent upper limit number density values at the two lunar atmospheric altitudes involved in the experiment. Further, upper limit surface number density values, $n(\lambda_r,0)$, can also be calculated using the F_1 function specified in Figure 2. This requires a downward extrapolation of the experimental data so that the $n(\lambda_r, 100 \text{ km})$-values were employed for this calculation. On this basis, the resultant values are listed below:

$$n(5890.0\text{Å}, 0 \text{ km}) = 28 \text{ cm}^{-3}$$

$$n(4226.8\text{Å}, 0 \text{ km}) = 99 \text{ cm}^{-3}$$

$$n(3933.7\text{Å}, 0 \text{ km}) = 40 \text{ cm}^{-3}$$

With respect to the above upper limit species calculations, it should be noted that the presented values have been predicated on the directly calculated $Y(\lambda_r)$-values of Table 15, which were obtained from published literature results without regard to possible errors. Owing to this and including the nature of the above analysis and selection of the 1σ value basis for the species calculations, it is felt that the presented species column counts and number densities can be regarded with a greater degree of confidence by increasing the tabulated results by a factor of two.

It should be realized that the magnitudes of the experimentally derived upper limit number densities specified above represent relevant and important data regarding the extent of the lunar atmosphere. Specifically, the most representative previous theoretical and experimental upper limit number density values are quoted as 10^6 and $10^3/\text{cm}^3$ for the total neutral and ion species, respectively. As such, the values quoted herein represent significantly lower upper limit values for the specific neutral and ion

species examined during the present program. Finally, owing to the lack of direct and possible evidence of the existence of the particular constituents in the lunar atmosphere, it is somewhat unjustified to perform a lunar atmospheric model validity analysis based on the available experimental results.

REFERENCES

1. Marmo, F.F. and Engelman, A.,"Earth Based Lunar Atmospheric Study," GCA Proposal 1191-5-01 (1965).

2. Glennon, B.M. and Wiese, W.L., "Bibliography on Atomic Transition Probabilities," NBS Misc. Pub. 278 (1966).

3. Sauermann, G.O. and Schultz, E.D., "Resonant Scattering Parameters for the Elements," Table 1, GCA Technical Note (1965).

4. Kvater, G.S., Vest. Leningrads. Univ. 2, 135 (OTP I, p. 142), (1947).

5. Penkin, N.P., JQSRT 4, 41 (1964).

6. Nesmeyanov, An. N., "Vapor Pressures of the Chemical Elements, Izd. ANSSSR, Moscow (1961).

7. Stephenson, G., Proc. Phys. Soc. 64A, 458 (1951).

8. Weingeroff, M., Z. Phys. 67, 679 (1931).

9. Chapman, R.D., Clarke, W.H., and Aller, L.H., Ap. J. 144, 376 (1966).

10. Bersuker, I.B., Izv, ANSSSR Ser. Fiz. 22, 749 (1958).

11. Griem, H.R., Plasma Spectroscopy, McGraw-Hill, New York (1964).

12. Bates, D.R. and Damgaard, A., Phil. Trans. Roys. Soc. Series A 242, 101 (1949).

13. Houziaux, L. and Sadoine, M.P., Bull. Soc. Roy. Sci. Liege 30, 287 (1961).

14. Fock, V., Z. Phys. 89, 744 (1934).

15. Biermann, L., Z. Ap. 22, 157 (1943).

16. Anderson, E.M. and Zilitis, V.A., Opt. Spect. 16, 99 (1964).

17. Stewart, J.C. and Rotenberg, M., JILA Rpt. No. 48 (1965).

18. Yu. I. Ostrovskii and Penkin, N.P., Opt. Spect. 10, 3 (1961a)

19. Trefftz, E. and Biermann, L., Z. Ap. 30, 275 (1952).

20. Douglas, A.S. and Garstang, R.H., Proc. Camb. Phil. Soc. 58, 377 (1962).

21. Douglas, A.S., Proc. Camb. Phil. Soc. 52, 687 (1956).

22. Zwaan, A., Naturniss. 17, 121 (1929).

23. Yu. I. Ostrovskii and Penkin, N.P., Opt. Spect. 11, 307 (1961b).

24. Lurio, A., de Zafra, R.L., and Goshen, R.J., Phys. Rev. 134, A1198 (1964).

25. Garstang, R.H., J. Opt. Soc. Am. 52, 845 (1962).

26. Trefftz, E., Z. Ap. 29, 287 (1951).

27. Hartree, D.R. and Hartree, W., Proc. Roy. Soc., A164, 167 (1938).

28. Brehm, B., Demtroder, W., and Osberghaus, O., Z. Natwforsch 16a, 843 (1961).

29. Penkin, N.P. and Shabanova, L.N., Opt. Spect. 14, 5 (1963).

30. Penkin, N.P., Conference on the Measurement and Calculation of Oscillator Strengths in Atomic Spectra, Leningrad (1959).

31. Biermann, L. and Lubeck, K., Z. Ap. 25, 325 (1948).

32. Yu. I. Ostrovskii and Penkin, N.P., Opt. Spect. 3, 193 (OTP I, p. 332), (1957).

33. Lawrence, G.W., Link, J.K. and King, R.B., Ap. J. 141, 293 (1965).

34. Goldberg, L., Muller, E.A., and Aller, L.H., Ap. J. Supp. 5, 1 (1960).

35. Manring, E., "Nuclear Debris Detection By Resonance Scattering of Sunlight-Project VELA," Semi-Annual Tech. Rpt. on Contract AF33(600)-42657, GCA-TR-61-42-A (1961).

36. Bucka, H. and Schussler, H.J., Ann. Physik 7, 225 (1961).

37. Gol'dberg, G.I., Izv. Glavn. Astron. Obs. Pulkovo 20, 156 (1956).

38. Allen, C.W., MNRAS 121, 299 (1960).

39. Morozova, N.G. and Startsev, G.P., Opt. Spect. 17, 174 (1964).

40. Bell, G.D., Davis, M.H., King, R.B. and Routly, P.M., Ap. J. 129, 437 (1959).

41. Ivanova, A.V. and Ivanova, A.N., Opt. Spect. 16, 499 (1964).

42. Weiss, A.W., Ap. J. 138, 1262 (1963).

43. Marmo, F.F., Engelman, A. and Best, G.T., "Study of Lunar Atmosphere Detection and Monitoring System, Volume I," GCA-TR-65-13-N (June 1965).

44. Minnaert, M., Mulders, G.F.W. and Houtgast, J., Photometric Atlas of the Solar Spectrum, D. Schnabel, Amsterdam, The Netherlands (1940).

45. Johnson, F.S., J. Meteorology 11 431 (1954).

46. Michel, F.C., Planet. Space Sci. 12 (11), 1075-1092 (1964).

47. Aller, L.H., The Abundance of the Elements, Volume VII, 54-55 and 122-123, Interscience Pub. Inc., New York (1961).

48. Bernstein, W., Fredericks, R.W., Vogl, J.L., and Fowler, W.A., "The Lunar Atmosphere and the Solar Wind," Icarus 2, 233 (1963).

49. Chamberlain, J.W., Physics of the Aurora and Airglow, Academic Press (1961)

50. Roach, F.E. and Megill, L.R., "Integrated Starlight over the Sky," Astrophys. J. 133, 228-242 (1961).

51. Roach, F.E. and Smith, L.L., "Absolute Photometry of the Light of the Night Sky," NBS Tech. Note No. 214 (1964).

52. Broadfoot, A.L., "Twilight Ca^+ Emission from Meteor Trails up to 280 km," Planet. Space Sci. 15 No. 3, 503-514 (1967).

53. Chorvinsky, M., Herman, J.R., McMinn, W.O., and Strano, J.S., "Optical Phenomena in Space," RADC Report No. TR-61-163, American Machine and Foundry Co. (1961).

54. Davis, R.J., "Project Celescope," Smithsonian Astrophysical Obs. Special Report No. 110 (1962).

55. Stecher, T.P. and Milligan, J.E., "Stellar Spectrophotometry below 3000Å," Astron. J. 66, 296 (1961).

56. Alexander, J.D.H., Bowen, P.H., and Heddle, D.W.O, "Southern Hemisphere Observations of Ultraviolet from Celestial Objects," Space Sci. Reviews IV, P. Muller, ed., J. Wiley and Sons, Inc., New York (1964).

57. Byram, E.T., Chubb, T.A., and Friedman, H., "Ultraviolet Light from Celestial Objects," Mem. Soc. Roy. Sci. Liege (Series 5) 4, 469-475 (1961).

58. Russell, H.N., Dugan, R.S., and Stewart, J.Q., Astrophysics and Stellar Astronomy II, Ginn and Co. (1955).

59. Chapman, R.M., et al., GCA Technical Report No. 61-35-A, Contract No. AF19(604(-7412, GCA Corp. (1961).

60. Blackwell, D.W. and Ingham, M.F., "The Zodiacal Light from a Very High Altitude, I," Mon. Not. Roy. Astron. Soc. 122(2), 113-128 (1961).

61. Smith, L.L., Roach, F.E., and Owen, R.W., "The Absolute Photometry of the Zodiacal Light," Planet. Space Sci. 13, 207-218 (1965).

62. Allen, C.W., Astrophysical Quantities, 2nd ed., The Athlone Press, London, 159-160 (1963).

63. Marmo, F.F., "Earth-Based Lunar Atmosphere Investigation,"Mid-Term Report, Contract No. NAS9-5589, GCA-TR-67-9-N (May 1967).

64. The Nautical Almanac for the Years 1966 and 1967, U.S. Government Printing Office, Washington, D.C.

65. Hamilton, D.R., "The Resonance Radiation Induced by Elliptically Polarized Light," Astrophys. J. 106, 457-465 (1947).

66. American Ephemeris and Nautical Almanac, 1956, U.S. Government Printing Office, Washington, D.C.

67. Stair, R. and Johnston, R., J. Res. NBS 51, 81 (1953).

68. Mandel, J., The Statistical Analysis of Experimental Data, Interscience, p. 75 (1964).

APPENDIX A

CRITICAL ANALYSIS OF OSCILLATOR STRENGTH DETERMINATIONS FOR SELECTED TRANSITIONS

A.1 INTRODUCTION

This Appendix contains a detailed discussion of the critical analysis performed to obtain the gf-values and error estimates of Table 1 in Section II. Under a previous program a list of oscillator strength values (Sauermann and Schultz, 1965) was derived using both theoretical and experimental values published in the open literature. However, no detailed evaluation was directed toward determining the "best" values along with corresponding error estimates. This approach was justified since the objective of a previous investigation was the determination of the feasibility of observing lunar atmospheric constituents by resonant scattering techniques. The previous oscillator strength estimates were sufficient for the design of the experiment, but it became evident that a critical analysis of the problem was required to derive values suitable for application to the analysis of the anticipated experimental results. It is the purpose of the present discussion to review and comment critically on current methods of oscillator strength determinations based on a large variety of experimental and theoretical techniques so that definitive uncertainty values can be attached to estimates.

A.2 CALCULATIONS OF OSCILLATOR STRENGTHS

Since neither a review of methods for calculating oscillator strengths nor the accuracy of such calculations exists in the literature, it is necessary to discuss these aspects of the problem in some detail.

For the present purposes, only allowed transitions (i.e., dipole transitions) are considered between low-lying levels of the discrete spectrum. Under these circumstances, the dipole approximation (neglect of retardation) is expected to be generally satisfactory except for atoms or ions with very large values of nuclear charge Z (Bethe and Salpeter, 1957, p. 248).

A.2.1 General Formulae for the Dipole Approximation. To find the oscillator strength in the dipole approximation it is necessary to calculate the matrix element of the dipole moment between the initial state, a, and the final state, b, of the system. Standard quantum mechanics (see e.g., Bethe and Salpeter, 1957, p. 251) leads to three different forms for this matrix element:

the dipole-length form $$\left\langle b\left|\sum_i \underline{r}_i\right|a\right\rangle = \left\langle a\left|\sum_i \underline{r}_i\right|b\right\rangle , \qquad \text{(A-1)}$$

the dipole-velocity form $$\frac{\left\langle b\left|\sum_i \underline{\nabla}_i\right|a\right\rangle}{(E_b - E_a)} = \frac{\left\langle a\left|\sum_i \underline{\nabla}_i\right|b\right\rangle}{(E_b - E_a)} , \qquad \text{(A-2)}$$

and the dipole-acceleration form $$\frac{\left\langle b\left|\sum_i \underline{\nabla}_i\, V\right|a\right\rangle}{(E_b - E_a)^2} = \frac{\left\langle a\left|\sum_i \underline{\nabla}_i\, V\right|b\right\rangle}{(E_b - E_a)^2} \qquad \text{(A-3)}$$

where the position of the ith electron is denoted by $\underline{r}_i$, and the energies of the initial and final states by E_a and E_b, respectively. Equations (A-1), (A-2), and (A-3) hold under very general circumstances; the case for the dipole-velocity form has been discussed by Green and Weber (1950). A sufficient condition is

$$H_a|a\rangle = E'_a|a\rangle \text{ and } H_b|b\rangle = E'_b|b\rangle \qquad \text{(A-4)}$$

for some (not necessarily the same) Hamiltonians H_a, H_b with eigenvalues E'_a, E'_b not necessarily equal to E_a, E_b. On the assumption of many-electron atom form for the potential,

$$V = -Z\sum_i \frac{1}{r_i} + \sum_{i<j} \frac{1}{|\underline{r}_i - \underline{r}_j|} \qquad \text{(A-5)}$$

where Z is the nuclear charge. The dipole-acceleration form (A-3) may be written (Bethe and Salpeter, 1957, p. 252)

$$\frac{Z\left\langle b\left|\sum_i \frac{\underline{r}_i}{r_i^3}\right|a\right\rangle}{(E_b - E_a)^2} = \frac{Z\left\langle a\left|\sum_i \frac{\underline{r}_i}{r_i^3}\right|b\right\rangle}{(E_b - E_a)^2} . \qquad \text{(A-6)}$$

The condition that the various expressions (A-1), (A-2), (A-3), and (A-6) should be equal to each other is more restrictive; a sufficient condition is that

$$H|a\rangle = E_a|a\rangle \quad \text{and} \quad H|b\rangle = E_b|b\rangle \ . \qquad \text{(A-7)}$$

It is not necessary that H should be the Hamiltonian of the actual physical problem, but it is necessary that the values used in (A-2), (A-3), and (A-6) for E_a and E_b should be the appropriate eigenvalues of this H.

Recently, Chen (1964) presented a fourth expression for the dipole matrix element and has shown how further equivalent expressions may be obtained; these, however, seem of little practical value.

A.2.2 Approximate Wave Functions: General Considerations. In non-relativistic quantum mechanics, the calculation of the dipole matrix element can be performed exactly only for the one-electron problem (Bethe and Salpeter, 1957, p. 262; Green, Rush, and Chandler, 1957). For any atom more complex, it is necessary to employ approximate wave functions to describe the upper and lower states of the transition; in general, these will not be eigenfunctions of the source Hamiltonian and in consequence, the different forms of the matrix element (A-1), (A-2), (A-3) will lead to different results. The problem now is to decide which forms of the matrix element are appropriate to the various possible types of approximate wave function.

Qualitatively, the forms (A-1), (A-2) and (A-3) may be distinguished by observing that, in the dipole length form, the contribution to the matrix element from regions of large r is important; whereas in the acceleration form, it is the region near the nucleus which is important. The velocity form lies between these two cases. As such, the regions in which an approximate wave function is well determined should be considered.

In view of the somewhat qualitative nature of this argument and the importance which will be attached to it, it is worthwhile to refer briefly to the extensive literature on the calculation of the bound-free absorption coefficient for the hydrogen negative ion. This involves calculating the transition matrix element between the ground state of H^- and the singly ionized system. The argument suggested above was employed by Massey and Bates (1940) to justify the use of a plane-wave continuum function in the dipole-length matrix element. Subsequent calculations of the absorption coefficient were reviewed by Chandrasekhar (1944) who pointed out that an increase in complexity of the Hylleraas-type variational wave function, corresponding to a small change in energy, yielded a relatively large change in the absorption coefficient. This he attributed to the variational wave functions being poorly determined by the energy criterion at large r. In a subsequent paper (Chandrasekhar, 1945a), calculations were performed using a 6-term and an 11-term Hylleraas trial function and all three forms of the matrix element. The velocity form was shown to be more stable under variations of the wave function than either of the other forms; this was attributed to the energy criterion leading to good determination of the wave functions in the regions (medium values of r) of importance in the velocity matrix element. A striking comparison of

the way in which the different forms of the dipole matrix element weight regions of space is presented by Chandrasekhar (1945b, Figure 1). Subsequent calculations using 20- and 70-term wave functions by Geltman (1962) have confirmed this result; furthermore, Geltman shows that the velocity form yields excellent agreement with the experimental results of Smith and Burch (1959).

It could be argued that H^- constitutes a particularly sensitive case; however, precisely the same problem arises in the calculation for He (Stewart, 1963, p. 346), and for systems with more than two electrons. Since it is necessary to employ approximate wave functions of types much less sophisticated than the wave functions available for the two electron case, the sort of problem discussed is expected to be even more important. On the other hand, for bound-bound transitions the simple arguments concerning dependence of the different forms of the matrix element on different regions of space do not necessarily follow, since the importance of a region heavily weighted by one bound-state function may be multiplied by the second function taking very small values.

Some insight into the accuracy of different types of wave functions may be obtained by an evaluation of the expectation values of various operators for two-electron systems with such wave functions and by a comparison of these results with those obtained using sophisticated wave functions of the Hylleraas, Kinoshita, or Pekeris types (see Stewart, 1963, for details). Such calculations were performed by Cohen (1961), who showed that the Hartree-Fock wave function for helium of Green, Lewis, Mulder, and Woll (1954) lead to expectation values of the operators r_1, r_1^{-1} and r_1^{-2} which agreed within 0.5 percent with values derived from the wave function of Pekeris (1959). Operators which weighted regions nearer to or further from the nucleus yielded less satisfactory agreement. More recently, Chen and Dalgarno (1965) performed similar calculations using the simple screened hydrogenic product function for helium, with and without correlation and in both the closed- and open-shell approximations, for the operators r_1^n, n taking integer values from -1 to +9. Again, good agreement is obtained with the more sophisticated calculation for n = -1, but the discrepancy increases to as much as 100 percent at n = 9.

These results reinforce the argument that a variational wave function is only reliable in the energy-important region and thus good only for evaluation of quantities roughly dependent on $\sum_i r_i^{-1}$ (note that normalization ensures that the expectation value of $\sum_i r_i^0$ is always given exactly). This in turn reinforces the argument that the dipole-velocity matrix element is to be preferred when a variational wave function is used. This may also be argued in another way. The virial theorem, which is always satisfied by a Hartree-Fock wave function and, obviously, by any wave function which includes a scaling parameter, ensures that a good total energy estimate implies a good kinetic energy estimate; that is, an energy-optimized wave function will give a good result for $< p^2 >$, the expectation value of the square of the momentum. Hence, reasonable values of $< p >$ can be expected as well as reasonable values of dipole-velocity matrix elements.

A step in the direction of putting these qualitative arguments on a mathematical basis may be made as follows. Assume that the available approximate wave function b′ may be related to the unknown exact wave function by

$$b' = b + \delta b \tag{A-8}$$

where δb is small. Then the dipole-length matrix element is

$$\langle b' | \sum_i \underline{r}_i | a \rangle = \langle b | \sum_i \underline{r}_i | a \rangle + \langle \delta b | \sum_i \underline{r}_i | a \rangle \tag{A-9}$$

where for simplicity it is assumed that the wave function a is known exactly. Now the dipole-velocity formulation yields

$$\frac{\langle b' | \sum_i \underline{\nabla}_i | a \rangle}{(E_b - E_a)} = \frac{\langle b | \sum_i \underline{\nabla}_i | a \rangle}{(E_b - E_a)} + \frac{\langle \delta b | \sum_i \underline{\nabla}_i | a \rangle}{(E_b - E_a)} \quad . \tag{A-10}$$

By (A-2), the first terms of the right-hand sides of (A-9) and (A-10) are equal (at least to a good approximation, if the experimental values for E_b and E_a are employed) to the exact value; the errors due to use of the approximate wave function are given by the second terms. In the dipole-velocity form, this error is inversely proportional to the excitation energy; this implies that the velocity form will be less sensitive to errors in the wave function for large excitation energies.

A more sophisticated version of this argument has been presented by Dalgarno and Lewis (1956) who conclude that if the excitation energy is larger than that associated with any other possible transition, then the velocity form is to be preferred. Calculations of the photoionization of helium support this hypothesis (Dalgarno and Kingston, 1958). From Equation (A-3) follows an obvious corollary that the dipole-acceleration form is likely to be especially sensitive to the approximate wave function for small excitation energies and reliable for very large excitation energies.

There is, however, a serious difficulty in estimating the error in a calculation of the transition integral (A-1), or any of the equivalent integrals, due to the fact that contributions to the integral may cancel. A very simple measure of this cancellation, suggested by Bates (1947), is obtained by calculating, in addition to the transition integral,

$$R = \int_0^\infty P_{n'\ell'}\, r\, P_{n\ell}\, dr \tag{A-11}$$

(where for convenience the central-field model is assumed in which only the radial integrals are considered over a single electron), the integral

$$X = \int_0^\infty |P_{n'\ell'}\ r\ P_{n\ell}|\,dr \tag{A-12}$$

where $P_{n\ell}$ and $P_{n'\ell'}$ denote the initial and final radial wave functions normalized in the sense

$$\int_0^\infty P^*_{n\ell}\ P_{n\ell}\ dr = 1\ . \tag{A-13}$$

Then

$$0 \leq \frac{|R|}{X} \leq 1\ , \tag{A-14}$$

the value 1 signifying no cancellation and the value 0 signifying complete cancellation. This simple test is useful for picking out transitions with heavy cancellation which in consequence cannot be calculated reliably.

A more sophisticated test of cancellation has been suggested by Layzer (1961). Using the same notation, $R_{n\ell}$ is defined by

$$R_{n\ell} = \int_0^\infty P_{n\ell}\ r\ P_{n\ell}\ dr \tag{A-15}$$

and $R_{n'\ell'}$ correspondingly.

Then, by Schwarz's inequality,

$$0 \leq \frac{|R|}{\sqrt{R_{n\ell}\ R_{n'\ell'}}} \leq 1 \tag{A-16}$$

where complete cancellation in R, of course, gives the lower limit 0, while the upper limit can only be attained when $P_{n\ell} = P_{n'\ell'}$. The expression (A-16) thus yields an indication of the similarity of $P_{n\ell}$ and $P_{n'\ell'}$.

It is important to note that in the central field approximation, certain transitions have no cancellation since neither radial function contains a node; these are transitions of the type $n,\ell \rightarrow n+1,\ \ell+1$ with $\ell = n - 1$. For these cases, the inequality (A-14) assumed the value 1, but (A-16) does not. The above considerations suggest that these nodeless transitions may be particularly amenable to calculation.

A final general matter concerns the excitation energies required for (A-2) and (A-3) and for converting dipole matrix elements into oscillator strengths, transition probabilities, and emission intensities (Bethe and Salpeter, 1957, pp. 248-250). Green and Weber (1950) and Green, Weber, and Krawitz (1951) discussed these problems and concluded that calculated energies should be used in preference to experimental energies. However, their evidence is very slight, although there is a possible qualitative argument in favor of using the calculated excitation energy with the dipole-velocity matrix element on the grounds that the two errors involved might cancel. In the absence of any sound theoretical argument, it is preferable to use the most accurate excitation energy available. It is the nonrelativistic energy which is required so the calculated value should be used for one- and two-electron problems and the experimental value in all other cases, except possibly when the relativistic error is expected to be very large as might be the case for an X-ray transition in a very heavy atom. These conclusions are in broad agreement with those of Bagus (1964). A possible source of error on this procedure, however, arises since identification of spectral lines is sometimes incorrect. A well-known example is a two-electron spectrum - that of Li^+ where Pekeris (1962) showed by calculation that the 2^1S - 2^1P line was at 9584Å and not at 8517Å as identified by Series and Willis (1958). A second example caused an error in calculations by Biermann and Lubeck (1948). They assumed that the line at 3082Å in Aℓ I belonged to the transition $3s^2\ 3p\ {}^2P^o$ - $3s^2\ 3d\ {}^2D$, as given by Moore (1949). Burgess, Field, and Michie (1960) suggest that the upper level should be $3s\ 3p^2\ {}^2D$, and this has been confirmed by Crossley (unpublished).

A.2.3 Coupling Schemes and Configuration Interaction. Most calculations are performed assuming LS-coupling (i.e., ignoring spin-orbit effects) and in a single configuration scheme. In certain cases, these are good approximations; when they are not, it is extremely difficult to estimate the error involved.

The expression "configuration interaction" is often used rather loosely, sometimes meaning little more than using a more flexible variational trial function. Perturbation theory affords a description of atoms in which the configurations that interact in LS-coupling are defined as those in the complex; the complex is defined by the set of one-electron principal quantum numbers and parity (Layzer, 1959). A good indication of the mixing involved is provided by the zero-order mixing coefficients of this scheme (Godfredsen, 1966). Configuration interaction is likely to be important when the active electron in either the initial or final state is in a shell containing other electrons; it is probably not important for transitions between states in both of which the active electron is highly excited and no other electron is excited. Thus, for a resonance transition, configuration interaction is usually important except for univalent atoms. Note that through configuration interaction, the simple concept of labelling a spectral term with a configuration breaks down, and two-electron jumps become permitted (see Edlen, 1964, p. 144).

While LS-coupling is generally satisfactory for small atoms, it is certainly necessary to allow for the spin-orbit interaction when the nuclear charge is large. This may be performed using intermediate coupling (Garstang, 1962; Gruzdev, 1962; and Mendlowitz, 1966). While Garstang's argument that the effects of spin-orbit interaction are important in O II cannot be agreed with, they certainly are important in A II; the change in intensity in weak lines is sometimes large percentage-wise. Again, the interaction is expected to be most important when the active electron is near other electrons - in particular, for a resonance transition. Qualitative insight into the importance of spin-orbit coupling may be gained from inspecting the strengths of forbidden lines or the relative line strengths in a transition array. An extensive study of lines of Fe I has recently been made by Shore (1965), but the general unreliability of the experimental data makes it impossible to derive more than the most qualitative conclusions in this way. Note that intermediate coupling is semi-empirical, since use is made of the observed energy levels.

The transitions of interest here are usually electric-dipole transitions, as discussed in this report; occasionally, however, data for a transition arising from other electric or magnetic interactions may be required. Such forbidden transitions have been reviewed by Garstang (1962, 1964).

A.2.4 The Two-Electron Atom. Because of the practicability of introducing coordinate systems which include the electron separation r_{12} explicitly, the solution of the Schrodinger equation for two electron ions has been developed to the stage where greater accuracy is achieved by calculation than by experiment; for a review, see Stewart (1963). Transition probabilities have been calculated for the $1,2\ ^{1,3}S - 2,3\ ^{1,3}P$ transitions in helium using the length, velocity, and acceleration forms and wave functions to three different orders of accuracy by Schiff and Pekeris (1964). The wave functions of the S-states were optimized under a constraint to ensure the correct atmospheric behavior, while the P-states were determined by the energy criterion alone. Additional results were presented for the $1\ ^{1}S - 2,3\ ^{1}P$ transitions with both functions optimized under the asymptotic criterion. This variety of results allows interesting comparisons of the convergence and accuracy of the different methods of calculation. Taking first the calculations in which only the S-state function is asymptotically correct, the velocity form yields excellent convergence in all cases, the greatest variation being 0.0008 on the f-value (1.3 percent). The length-form does almost as well and improves with decreasing excitation energy. The acceleration-form gives adequate results for large excitation energy, but fails badly in other cases (e.g., for $2\ ^{1}S - 2\ ^{1}P$ there is a variation of 50 percent). When both wave functions are asymptotic, the convergence of the velocity form increases while that of the length-form remains about the same (it must be borne in mind that the asymptotic restraint leads to a poorer overall representation of the eigenfunction for a given expansion-length). All this evidence indicates that, on the basis of the limited number of calculations so far available, the qualitative ideas discussed above apply very well in practice.

A.2.5 Hartree-Fock Wave Functions. The usual approach to solving the Schrodinger equation for the N-electron atom (N > 2) is to employ the central field approximation and the variational method (see e.g., Condon and Shortley, 1935). The Hartree-Fock method is the most sophisticated treatment of this kind and provides the best available wave functions for a complex atom (see e.g., D. R. Hartree, 1957). Programs are available for solving the Hartree-Fock coupled integro-differential equations both numerically (Froese, 1963; Mayers and Hirsh, 1965) and analytically (i.e., using a set of basis functions with variable parameters) (Roothaan and Bagus, 1963; Pfennig, Steele, and Trefftz, 1965). The numerical method of solution is practical and to be preferred, since it leads to better energies and avoids the arbitrariness of the choice of basic functions in the analytical method; however, transition probabilities do not appear to be very sensitive to the wave functions employed (Pfennig et al. 1965). Approximate methods, such as the "configuration average" method of Slater (1960) and Herman and Skillmann (1963) employed by Kelly (1964b) are unnecessary and should be avoided, since they ignore the configuration structure of interest herein. It is possible to allow for configuration interaction, but to do this consistently requires an iteration process for the mixing coefficients (Hartree, Hartree, and Swirles, 1939; Hartree, 1957) which makes the calculation very lengthy; however, a program has recently been developed to accomplish this (Froese, unpublished). A simpler, but less exact, method is to treat each configuration separately, diagonalize the energy matrix, and use the ensuing wave functions (extended Hartree-Fock scheme). Transition probabilities have been calculated in this way by Biermann and Trefftz (1949), Trefftz (1949, 1950, 1951), and Froese (1964, 1965a, b); these calculations show the importance of allowing for configuration interaction within a complex, as is suggested by the Z-expansion treatment of the Hartree-Fock method (see Section A.2.9). The addition of other configurations usually has only a very small effect, essentially due to the trial wave function being made more flexible. Froese (1965b) discusses a transition for which the upper bound state lies in and interacts with the continuum; in such a case, it is necessary to allow for autoionization (see e.g., Fano, 1961).

Herman and Skillmann (1963) and Mayers and Hirsh (1965) discuss spin-orbit and relativistic corrections in the Hartree-Fock scheme. It is also possible to perform calculations directly in a relativistic scheme (see Hartree, 1957), or in an "open-shell" scheme (unrestricted Hartree-Fock; Pratt, 1956); this last method, however, has certain drawbacks (Marshall, 1961) and does not appear to yield reliable transition probabilities (Trefftz et al. 1957). Other generalizations of the Hartree-Fock method are described by Hartree (1946).

The "active electron" approximation in obtains when the spin-orbitals of the "passive" electrons (i.e., those not engaged in the transition) seem to satisfy orthonomality integrals between the two states of the system; calculations suggest that the error here is very small (Veselov, 1949; Bagus, 1964). It is also possible to perform calculations in which the spin-orbitals of both the initial and final states are drawn from the

wave function of a system with one more electron (the "frozen orbital" approximation); this leads to rather less satisfactory results (Bagus, 1964). Improvement might be obtained with an additional term in the potential to allow for polarization (e.g., Chisholm and Opik, 1964). However, the recent development of adequate computer programs has made these approximations unnecessary.

A serious difficulty arises in the Hartree-Fock method in defining excited-state wave functions when there is a lower state of the same symmetry. The problem is discussed by Hartree (1946, 1957, p. 36) and more recently by Cohen and Kelly (1965), but no definite conclusions are reached. For a resonance transition, however, this problem will not usually occur.

The existence of the calculations of Schiff and Pekeris (1964) for helium, described above (Section A.2.4), allows a direct assessment of the accuracy of approximate calculations for this atom. Extensive Hartree-Fock calculations have been performed by Vizbaraite, Kantserevichyus, and Yutsis (1956) who simplified the method for the more highly excited states and by Trefftz, Schluter, Dettmar, and Jorgens (1957) who employed both correlated and uncorrelated wave functions in both the closed- and open-shell approximations with both length and velocity formulae. Similar calculations have been performed by Weiss (unpublished) and Froese (unpublished).* Comparison with the essentially exact result is interesting; taking the ordinary Hartree-Fock calculations first, for the six transitions where comparison is possible, the error ranges up to 13-1/2 percent with the length form and up to 28 percent with the velocity form. Introduction of a correlating factor (Trefftz et al. 1957) brings about a considerable improvement, the largest errors now being 8-1/2 percent (length) and 8 percent (velocity). Correlated open-shell calculations (only two comparisons available) reduce the largest errors to 1 percent (length) and 2 percent (velocity); however, for these two transitions the correlated closed-shell calculations lead to greatest errors of only 5 percent (length) and 3-1/2 percent (velocity), and the open-shell method without correlation is not very successful. Thus, the bulk of the error in the Hartree-Fock calculation can be avoided by inclusion of a simple correlation term in the closed-shell calculation. As might be expected, this correlation correction is particularly important for the resonance transition; the difficulty of performing a satisfactory calculation for resonance transitions has previously been noted by Dalgarno and Lynn (1957).

Trefftz et al. (1957) recommend the use of the dipole velocity formula with calculated energies, while Weiss (unpublished) recommends the length formula with experimental energies on the strength of comparisons between Hartree-Fock calculations and calculations of Pekeris-type. As discussed above, there is no good reason for using calculated energies; on the other

*Weiss and Froese show that the dipole-length result of Trefftz et al. (1957) for the resonance transition (closed-shell method) is incorrect.

hand, it is interesting to note that apart from the resonance transition, good results are obtained from the straight Hartree-Fock calculations for helium by application of the qualitative arguments advances above. Clearly, the $1\ ^1S - 3\ ^1P$ and $2\ ^3S - 3\ ^3P$ transitions can be excluded, where the matrix elements are small and cancellation difficulties are expected. Using the length formula for transitions where there is no change of principal quantum number and no small excitation energy (and the velocity formula in other cases) then the errors in the three transition remaining are:

$2\ ^1S - 2\ ^1P$	(length)	3.5 percent
$2\ ^1S - 3\ ^1P$	(velocity)	1.9 percent
$2\ ^3S - 2\ ^3P$	(length)	3.3 percent

These results are very satisfactory.

Bagus (1964) presents results for Ne^+ and Ar^+ using the length, velocity, and acceleration forms of the matrix element. Since there are no exact results available, it is impossible to state which form of the matrix element is the best. However, the general arguments advanced here are supported by the fact that the acceleration form leads to much more satisfactory results (i.e., results in better agreement with the length and velocity results) for X-ray (high energy) transitions than in other cases.

Pfennig, Steele, and Trefftz (1965) present single-configuration Hartree-Fock calculations for nine transitions in beryllium-like ions (Be I, C III, N IV, O V) using both the length and velocity matrix elements. Agreement between these two methods for Be I, while fair for triplet transitions, is quite poor for singlet transitions where even in the best case (the resonance transition) the length result is twice the velocity result. The results for the isoelectronic ions exhibit similar but less extreme tendencies, the agreement between length and velocity forms improving with increasing ionization. These results are qualitatively what might be expected on the assumption that the major error for the singlet transitions is due to neglect of configuration interaction, while for the triplet states considered, which are probably not seriously affected by configuration interaction, discrepancies are due to neglect of correlation. No comparison with experimental work is possible for these ions.

A procedure which allows for correlation effects in atomic structure and uses the random phase approximation of many-body theory (see e.g.,Pines, 1955; Valatin, 1961) yields a formulation which is a generalization of the Hartree-Fock method which has been discussed by Altick and Glassgold(1964) who performed trial calculations for Be, Mg, Ca, and Sr which demonstrate that large errors may accrue in a transition probability calculation from use of an overly simple approximation; however, the use of Hartree or Thomas-

Fermi central fields by these authors reduces the value of their qualitative results. The Brueckner-Goldstone treatment of many-body theory has been employed for atoms by Kelly (1964) who presents transition probability calculations for $2S^2\ ^1S$ - 2S np ^1P transitions in beryllium. These results also show the importance of taking correlation effects into account. However, neither of these developments at present appear likely to supersede the conventional Hartree-Fock treatments.

It is concluded that carefully performed extended Hartree-Fock calculations can possibly lead to transition probabilities as accurate as 5 percent. However, the evidence discussed is very scanty; more calculations and comparisons are necessary. For resonance transitions, the Hartree-Fock method is insufficient unless allowance is made for correlation; errors of 10 to 15 percent occur even in apparently favorable cases.

A.2.6 Other Variational Wave Functions. Simple analytical trial functions for the variational method are described by Slater (1960; Vol. I, p. 348). Those of Morse, Young, and Haurwitz (1935) are the most complex;* a simple scheme is suggested by Slater (loc.cit.p. 368). Energies obtained with these functions are usually inferior to Hartree-Fock energies, and there is no reason to suppose that transition probabilities calculated with such functions will be other than correspondingly inaccurate. Nevertheless, calculations of this type have been performed by Vainshtein and Yavorskii (1952) using Slater-type functions and Bolotin and Yutsis (1953) using Morse-type functions with configuration-interaction. A brief review of work up to 1956 is given by Vainshtein (1961); a more recent paper discussing the convergence of the multi-configurational approximation is that of Yutsis, Vizbaraite, Strotskite, and Bandzaitis (1962). Vetchinkin (1963) discusses the choice of approximate wave functions with particular reference to transition probability calculations.

These calculations, while showing the importance of allowing for configuration interaction, lead to unsatisfactory results. The obvious development is to include much larger numbers of configurations in the interaction, that is, to use a variational trial function consisting of a linear combination of Slater determinants each built up from, for example, Slater orbitals. The physical concept of the configurations is thus more or less abandoned (cf. the discussion of Green, Kolchin, and Johnson, 1965). Calculations of this sort for the ground state and a few excited states of two-electron ions have been reviewed by Stewart (1963). More recently, extensive calculations for the ground and excited states of helium have been performed by Green, Kolchin, and Johnson (1965), and the results have been used in the calculation of helium oscillator strengths (Green, Johnson, and Kolchin, 1966a). The results of this work are most encouraging; first, the method yields better energies than Pekeris' for the

*Corrections and extensions of the original work have since been published (Tubis, 1956; Morse and Yilmaz, 1956; and see Slater, loc.cit).

3 ^1S and 6 ^3S states upwards (showing, as is to be expected, that electron correlation is more important in the triplet states than in the singlet states) even though only eight configurations are used for the 6 ^3S wave function. In 100 cases out of 203, the length and velocity forms lead to results agreeing within 1 percent. For the 1 ^1S - n ^1P transitions (Green, Johnson, and Kolchin, 1966b), the length and velocity results agree within 2 percent in every case, and the 1 ^1S - 2 ^1P and 1 ^1S - 3 ^1P oscillator strengths are within 1 percent of the effectively exact results of Schiff and Pekeris (1964). The energies of the 42 excited levels differ from the experimental values (the lower levels corrected for relativistic effects) by an average of 1 in 300,000.

These results tend to confirm that the transition matrix element is not over-sensitive to the precise form of the wave function, except under conditions of extreme cancellation. The real value of Green's work, however, is that it is straightforward to extend his method to more complex atoms; indeed this may well prove to be a more practicable approach for the calculation of transition probabilities than the extended Hartree-Fock method.

A.2.7 The Coulomb Approximation. Hartree (1927) very early recognized that Hartree-type wave functions did not have the correct asymptotic behavior at large r, and attempted to construct improved wave-functions for single valence electrons moving in the assumed central field of the nucleus and core electrons by finding the correct asymptotic form and joining it smoothly to the Hartree wave function describing the energy-important region. The asymptotic behavior of the wave function is described by the Whittaker functions; the appropriate mathematical development is given by Waller (1927), Hartree (1927), and Hylleraas (1945). Chandrasekhar (1944) suggested that transition probability calculations with the length form would be improved by the use of wave functions having the correct asymptotic form, and Bates and Damgaard (1949) showed that the use of the asymptotic form alone was sufficient for the calculation of a wide range of transition probabilities (the Coulomb approximation). The use in this method of the experimental energy to determine the asymptotic form leads to noninteger principal quantum numbers, and a problem arises as to how to normalize the Whittaker functions under these circumstances. This problem has been investigated by Ham (1955), Seaton (1958), and Burgess and Seaton (1960) who show that the assumption about normalization made by Hartree (1927) and Bates and Damgaard (1949) is incorrect but will not lead to serious error except when the change in the effective principal quantum number in the transition is less than 1.5. It is not possible, however, to obtain the exact normalization factor. It may still be asked, however, whether normalization of the asymptotic wave function is the best procedure; an alternative procedure would be to choose the normalization factor so that some atomic property, e.g., $< r >$, is given correctly.

Bates and Damgaard show that their method is accurate for a simple case (e.g., transition between high-lying singly-excited states), and

their results yield generally good agreement with experiment except in complex cases where the active electron is involved with partly-filled shells. The method is semi-empirical in that experimental ionization energies are used, but this means that, qualitatively, some configuration mixing is allowed for. The claims made for their method by Bates and Damgaard seem, in general, over-cautious.

Bates and Damgaard present tables from which transition probabilities may be calculated. Many authors have given f-values from these tables (Asaad, 1956; Goldberg, Muller, and Aller, 1960; Allen, 1960, 1963; Houziaux and Sadoine, 1961); a particularly extensive tabulation has recently been given by Griem (1964).

Three alternative methods suitable for a one-electron problem have been developed. The first (Zwaan, 1929) employs the Wentzel-Brillouin-Kramers method to describe the central field (see e.g., Condon and Shortley, 1935, p. 339; and Jeffreys, 1961, p.245); Zwaan's results are discussed briefly by Condon and Shortley (1935, p. 148) and by Bates and Damgaard (1949). More recently, Petrashen and Abarenkov (1954) have taken up the original suggestion of Hartree (1927) discussed above, and calculations of transition probabilities on sodium by this method have been performed by Anderson, Buzka, Grinsberg, and Saulgozka (1956). The third approach (Stewart and Rotenberg, 1965) uses a scaled Thomas-Fermi potential.

These three methods in principle should be more accurate than the Bates-Damgaard method, but in practice the improvement seems to be marginal and the Bates-Damgaard method is more widely applicable and easier to handle. The accuracy of all these methods is good, the probable error for appropriate transitions being 10 percent or better; however, resonance transitions rarely fall into the class of "appropriate transitions".

A.2.8 Screening Methods. Varsavsky's (1958, 1961) calculation of transition probabilities has had considerable application in astrophysics, being the only method claiming to yield good results from a simple calculation. Hydrogenic functions are screened with the screening constant determined (effectively) by the variation principle. Similar to the methods of Section A.2.2, the dipole-length matrix element is employed. Bagus (1964) compares his Hartree-Fock results with Varsavsky's for univalent cases, which Varsavsky's method should treat best, and finds an almost constant factor 2 difference; this suggests use of an incorrect formula by Varsavsky. Generally, Varsavsky's results agree poorly with experiment, so it seems wise to treat his work with considerable caution.

A.2.9 Perturbation Treatments. Dalgarno recently developed a method of calculating atomic properties based on Rayleigh-Schrodinger perturbation theory; a convenient review is provided by Hirschfelder, Byers, Brown, and Epstein (1964). Its advantage is that a single calculation yields results for a whole isoelectronic sequence, and the accuracy increases with the nuclear charge. The calculation of transition probabilities by this

method has been performed by Cohen and Dalgarno (1964) (up to ten electrons), Crossley and Dalgarno (1965) (sodium and magnesium sequences), and Crossley, Dalgarno, and Parkinson (to be published) (aluminum sequence); similar results (up to magnesium) were obtained by Froese (1965a) who used a numerical method. All these calculations are based on the extended Hartree-Fock method (that is, configuration interaction is included at zero-order in the wave function) and use the dipole length matrix element. A screening parameter is introduced - chosen so that the first-order contribution to the matrix element is zero; this choice is correct in calculations of energy, but theoretical justification for other expectation values is lacking (Dalgarno and Stewart, 1960, and Section A.2.11). Only transitions in which the principal quantum number $\underset{\sim}{n}$ of the active electron has its lowest value (and does not change) have been considered. The agreement with comparable full extended Hartree-Fock calculations is surprisingly good, the difference in the values of the transition integral being generally less than 1 percent for ions at least twice ionized.

An improved method (Cohen and Dalgarno, 1966) uses the Hartree-Fock formalism as the zero-order problem; matrix elements can then be calculated exactly to first order. Results for the $2^{1,3}S - 2^{1,3}P$ transitions in neutral helium agree with the effectively exact results of Schiff and Pekeris (1964) to 4 percent, and the accuracy of the method is expected to improve rapidly with increasing degree of ionization. This approach enables the shortcomings of the Hartree-Fock method to be analyzed (see also LaPaglia and Sinanoglu, 1966).

A.2.10 Sum Rules. Many authors used the Kuhn-Reiche-Thomas f-sum rule (Allen, 1963, p. 55) to obtain crude f-values and also to put experimental relative values on an absolute scale (see e.g., Allen, 1960). Since the summation is performed over all bound-bound and bound-free transitions from a given bound state, accuracy for a particular level is usually impossible; however, a limit may sometimes be obtained (see e.g., Dalgarno and Kingston, 1959). Green, Weber, and Krawitz (1951) show that satisfaction of this sum rule says nothing about the individual f-values. However, other sum rules exist and have been used very successfully in the case of the helium atom (see Stewart, 1963) where extensive calculations of oscillator strengths for bound-bound and bound-free transitions, and of other properties, were available.

A.2.11 The Improvement of Approximate Results. Currently, much attention is being paid to the problem of determining good expectation values in quantum mechanics; a brief survey of work in progress is described below.

The most unsatisfactory feature of the methods described above is that in no case are we able to do better than guess the accuracy of the results. It would be a great advance to have a means for predicting theoretical upper and lower bounds to expectation values, as in the case for energy (see e.g., Wilson, 1965; Lowdin, 1965). At present, unfortunately, this seems to be a rather ambitious objective.

As noted previously in Section A.2.9, Dalgarno introduced a screening parameter into the calculation of expectation values by the expansion method. Various attempts have been made recently to justify this step by application of hypervirial theorems (Hirschfelder and Sanders, 1965; Robinson, 1965; Bangudu and Robinson, 1965), by use of the first-order density matrix (Hall, Jones, and Rees, 1965),and by use of the Hellmann-Feynman theorem (Jones, 1965). The evidence generally supports Dalgarno's choice (Hirschfelder and Sanders, 1965), but a proof is still lacking.

Additionally in Section A.2.9,a perturbation treatment was discussed in which the Hartree-Fock method is used as the zero order problem. Chen and Dalgarno (1965) have given a method of improving expectation values obtained from approximate wave functions. The method has not been applied to transition probabilities, but appears very promising for this purpose. Other advances in perturbation theory were described in Section A.2.9.

Finally, it is possible that wave functions leading to inferior energies would yield better expectation values than wave-functions which are "best" in the energy sense. Attempts to find criteria for choosing such "operator-adapted" wave functions are being made (Mukherji and Karplus, 1963; Coulson, 1965).

A.3 MEASUREMENT OF OSCILLATOR STRENGTHS

It is unnecessary to present a detailed discussion of the methods of experimental measurement of atomic oscillator strengths herein, since this subject has been thoroughly reviewed by Foster (1964). Therefore,the present section is limited to commentary and where necessary,a revision to Foster's article. For ease of cross-reference, Foster's paragraphs numbers will be used here, prefixed by "3".

3.1 "Few of these constants (oscillator strengths, etc.) are known to 1 percent, or even to 10 percent, and their precise measurement presents formidable difficulties."

3.1.1 Errors in experimental oscillator strengths fall into two classes: errors in the measurement itself (these are the errors usually estimated) and systematic errors in the reduction of the experimental data to the theoretical quantity required which arise from the shortcomings of assumptions about thermal equilibrium vapor pressure, optical thickness, collisions, etc. These systematic errors may often be large and are difficult to allow for. An example of a source of systematic error is the disagreement over the standard carbon arc intensity, which varies up to 7 percent according to author and wavelength region.

3.1.2.1 Most experimental methods measure intensity; to obtain the Einstein transition probability, A, requires further measurement (see Foster's Equation 1.6) of the number density of atoms and the thickness of the emitting layer. These are usually very difficult to determine

and so it is not possible to obtain accurate absolute oscillator strengths; however, it is generally possible to control the experiment in such a way that an assumption may be made about the thermal equilibrium and reliable relative oscillator strengths obtained.

3.1.2.2 Measurements of lifetimes of excited states are usually free from the problem of the determination of number density.

3.1.2.3 The neglect of forced emission is another example of an approximation often made in reducing experimental measurements to the theoretically-defined quantities.

3.1.2.4 A discussion of the methods and accuracy of theoretical methods for the determination of transition probabilities has, of course, been given in this report.

3.1.5 A revised edition of the "Bibliography on Atomic Transition Probabilities" has now been published (Glennon and Wiese, 1966).

3.2 Lifetime measurement is one of the three most profitable approaches to experimental oscillator strengths and is (in suitable cases) the most reliable method for absolute oscillator strengths. The conversion of lifetimes to oscillator strengths sometimes requires knowledge of "broadening factors" - that is, relative oscillator strengths. If these are not available, or if a forbidden transition is ignored, then the lifetime method usually gives an upper bound to the oscillator strength.

3.2.1 Method of Direct Observation of Decay. This method is only suitable for weak lines (long lifetimes) and is not suitable for resonance transitions.

3.2.2 Phase-Shift Method. This method, with optical excitation, is particularly suitable for the determination of absolute oscillator strengths of resonance transitions. The use of electronic excitation brings added difficulties due to cascading; nevertheless, this method has been used recently by Lawrence (1965) who shows how cascading may be allowed for. Results for atoms are given by Lawrence and Savage (1966) and by Savage and Lawrence (1966)who estimate the error is due to zero phase reference inaccuracy, instrumental errors, approximations in the cascade correction, and spectral impurities at 10 to 15 percent for the longer-lived states. Less precision is possible for the shorter-lived states which, of course, correspond to the larger oscillator strengths. An additional source of error might be self-absorption, particularly with resonance lines (see Section 3.2.3). Thus, this very recent work does not appear to have the accuracy of the optical excitation experiments of Brehm, Demtroder, and Osberghaus (1961) discussed by Foster.

3.2.3 Delayed Coincidence Methods. The problem of self-absorption in the resonance line, mentioned above, is discussed here by Foster.

3.3 Thermal Equilibrium in Arc Discharges. The vast majority of relative oscillator strengths in the literature derived from experiments of this kind, notably by Corliss and Bozman (1962), is discussed below (Section 3.3.2.1). A brief review of these methods is given by Penkin (1964), and reference may be made to the book by Griem (1964). Control of these experiments is extremely difficult so that absolute oscillator strengths cannot be determined, in general, to better than an order of magnitude. However, under suitable circumstances relative oscillator strengths can be obtained for a very wide range of excitations and intensities, these being the only practicable methods for measuring weak lines connecting highly excited levels. Such relative determinations could then be put into an absolute scale by recourse to some other method for a few selected lines. The discharge process itself has been the subject of very extensive investigations (e.g., Mazing, 1961; Hefferlin and Gearhart, 1964).

3.3.1 Utrecht Arc Method. See Section 3.3.2.1.

3.3.2 Other Arc Methods.

3.3.2.1 The Semi-Absolute Dilute Copper Alloy Calibration Method. By far the largest collection of f-values in the literature is the computation of Corliss and Bozman (1962). This is based on the tables of spectral line intensities of Meggers, Corliss, and Scribner (1961) which were prepared primarily for the purposes of spectrochemical analysis. Consequently, the accuracy of the derived gf-values is not large; Corliss and Bozman suggest standard deviations of 40 to 50 percent in relative gf-values within a single spectrum, and of 70 to 100 percent in absolute gf-values. These estimates are based on estimates of the accuracy of the intensity determinations (standard deviation 32 percent) and of the arc temperature (6 to 56 percent according to excitation energy; see Corliss, 1962). However, there appear to be further errors in the second section of iron-group elements, and presumably elsewhere due to the ionization potentials used; these errors decrease with ionization potential to an order of magnitude for nickel (Warner, 1964). Below 2500Å the quoted values appear to be too small by up to a factor of two, presumably due to an error in the extrapolation process used to determine the energy calibration in this region (Warner, 1964; Morozova and Startsev, 1965). Beyond these specific errors, the whole process used of dissolving electrodes containing the different elements into the plasma is perhaps open to question though Morozova and Startsev (1964), who have performed similar experiments, give arguments in support of the process. Resonance lines, however, may often be subject to self-absorption.

The rather similar work of Allen is sufficiently described by Foster.

3.3.2.2 The Absolute Method of Mannkopff, Eberhagen, and Eicke. There are so many problems to be resolved with arc methods that determinations of absolute f-values at present must be reported as untrustworthy. Eberhagen (1955) gives an estimated error of 33 percent for the resonance line of

strontium; Penkin and Shaganova (1962) find his results in poor agreement with their own from the Hook method (Section 3.4.4).

3.3.3 Absolute Measurements with the Kiel Arcs. In addition to the methods described by Foster, a free-burning arc source has been developed and utilized for the measurement of absolute oscillator strengths in argon by Olsen (1963a), who has also given a review of arc methods for quantitative spectroscopy (Olsen, 1963b). Olsen has paid particular attention to estimating thermal equilibrium, to investigating the thermal plasma composition (Olsen, 1959) and the ionization equilibrium (Olsen, 1961), and to correcting for self-absorption. Similar techniques have been used by Dickermann and Deuel (1964a) for determining relative transition probabilities in copper, aluminum, and molybdenum; these authors have also suggested an alternative means of dealing with self-absorption (Dickermann and Deuel, 1964b). Olsen (1963a) estimates his errors in intensity measurement at 3 to 12 percent, and the error in the absolute transition probabilities at ~20 percent. Dickermann and Deuel plan to put their relative values into an absolute scale by the use of other work; this procedure seems to us the most satisfactory.

3.3.4 Luminous Shock Tubes. Another description of the use of shock tubes for quantitative spectroscopy has been given by Wurster (1963). The problems involved in understanding the shock tube process are still being studied. In addition to the problems discussed by Foster, there are those connected with the insertion of the material of interest into the shock; for a recent discussion see Garton, Parkinson, and Reeves (1964).

3.4 Measurement of Oscillator Strengths of Discrete States. The two most valuable sources of oscillator strength measurements are derived from the work of King, using absorption methods, and the work of Penkin, using the "Hook" method of Rozhdestvenskii. In both cases, there has been continuing improvement of the experimental methods and of the resulting accuracy.

3.4.1 - 3.4.2 Measurement of the equivalent width of an absorption line is the basis of the total absorption method. This is the procedure used by Bell, Davis, King, and Routly (1958) and described by Foster. Penkin (1964) gives a brief review of the method, pointing out the possible limitation and sources of error - in particular, the necessity of knowledge of the hyperfine structure. Improved procedures, notably the use of photoelectric means of recording, were discussed by King (1963) in a brief review, and employed by Lawrence, Link, and King (1965) who estimate the errors in their absolute f-values as 10 to 20 percent. Most of the error is attributed to the difficulty of determining the number density; for example, Lawrence, Link, and King recalculated results of Estabrook (1951) for nickel on the basis of improved vapor pressure data, giving a 60 percent increase in the f-values. Consequently, the relative f-values of Lawrence, Link, and King should be of much higher accuracy (5 percent).

3.4.3 Absorption Methods - The King-Furnace Observations. This earlier work has largely been superseded by the work just discussed. Some of the relative f-values have been scaled according to later absolute determinations; see e.g., Lawrence, Link, and King (1965).

3.4.4 Dispersion and Anomalous Dispersion. The anomalous dispersion or Hook method as now developed is one of the most valuable techniques for measuring f-values. The description given by Foster, however, is in need of revision. The most significant improvement in the method has been the combining of the Hook and total absorption methods so that the determinations of number density and vapor column length are avoided; these were thought to be the major sources of error in the method described by Foster. The use of photoelectric recording techniques eliminates most of the remaining errors, so that Penkin now claims an overall accuracy of 3 to 5 percent for absolute f-values; this is perhaps a little optimistic. These improvements have been described by Ostrovskii and Penkin (1961),and the whole program of work in this field by Penkin and his co-workers up to about June 1962 has been reviewed (Penkin, 1964). Some of the results from earlier work are given in this review in revised form on the basis of new vapor pressure data (Nesmeyanov, 1961) which appear to be sufficiently reliable to remove most of the error from the method described by Foster. This has permitted accurate measurements to be made for silver, gold, tin, and lead (Penkin and Slavenas, 1963a,b) which are not suitable for the total absorption method; in the case of the resonance line of silver, 3280Å (for which a wide scope of temperatures is possible) Penkin's results show a random error of less than 1 percent while the system errors may be as low as 2 percent.

An even more recent review of the Hook method has been presented by Marlow (1965) who gives numerous references to the recent literature; more recent papers are those of Shukhtin (1965) and Mertz (1966).

3.5 Some Special Methods for Discrete States. In addition to the methods described by Foster, interest has recently been renewed in the method of linear absorption, which is fully described by Mitchell and Zemansky (1934). Relative oscillator strengths in copper have been measured by Ostroumenko and Rossikhin (1965) using this method; it should be noted that their results may readily be put on an absolute scale by using the results for the resonance doublet given by Penkin and Slavenas (1963a) mentioned in the previous paragraph. There is, however, insufficient comparison data as yet for an evaluation of the accuracy of this method.

The linear absorption method has been ingeniously combined with the total absorption method to measure absolute values of oscillator strengths by Lvov (1965) whose results for the resonance lines of lead and cadmium are in reasonable agreement (10 percent) with other work.

3.6 - 3.7 Since the measurements of resonance transitions are of major concern herein, comment on Foster's discussion of auto- and photoionization is omitted.

A.4 CONCLUSION

Oscillator strengths for hydrogen-like ions may be calculator precisely in the dipole approximation (Section A.2.2). For the case involving two-electron ions, see Section A.2.4 whereas for more complicated ions, a combination of methods is recommended. Resonance lines of neutral atoms may be measured to great accuracy by the lifetime method with optical excitation (Section 3.2.2),and the results used to put relative f-values on an absolute scale; good relative values may be obtained from the absorption methods (Section 3.4.3) or from the Hook method (Section 3.4.4) for at least the lower transitions of many atoms. Alternatively, the absolute scale could be attained in some cases by means of a sophisticated calculation of the kind described in Section A.2.6. In this way, it should be possible to obtain oscillator strengths for a large number of low transitions in neutral atoms to an accuracy of better than 5 percent.

For transitions involving higher excited levels in neutral atoms and for ionized atoms, the situation is more complex. Higher excitations in neutral atoms are probably best dealt with by taking relative f-values from carefully controlled emission-arc methods (Section 3.2.3) leading to absolute values of about 10 percent accuracy; for small atoms (and ions) in suitable configurations,the Bates-Damgaard method (Section A.2.7) is recommended (10 percent). For positive ions, experimental methods become inaccurate, increasingly so with increasing ionization; on the other hand calculations generally become more accurate (notably the perturbation methods described in Section A.2.9). It is possible that the accuracy of calculations based on a nuclear-charge expansion could be improved by fitting the expansion to experimental results for the neutral atom case.

In conclusion,it seems reasonable to suppose that the enormous effort now being directed to finding oscillator strengths for atomic systems will lead to a considerable improvement in the existing data, particularly for the lower transitions of neutral atoms.

REFERENCES

(OTP I, OTP II refer to the two volumes of Russian Translations, Optical Transition Probabilities, NSF Israel Program for Scientific Translations.)

C W. Allen, 1960: Mon. Nat. Roy. Astr. Soc. 121, 299.

C. W. Allen, 1963: Astrophysical Quantities (2nd edition) Athlone Press, London.

P. L. Altick and A. E. Glassgold, 1964: Phys. Rev. 133, A632.

E. M. Anderson, Z. A. Buska, R. O. Grinberg and A. K. Saulgozka, 1956: Vestnik Leningradskogo Universiteta, No. 4, 27. OTP I, p. 296.

A. S. Asaad, 1956: Thesis, London University.

P. S. Bagus, 1964: SCF Excited States and Transition Probabilities of Some Neon-like and Argon-like Ions, Argonne National Laboratory Report No. ANL-6959.

E. A. Bangudu and P. D. Robinson, 1965: Proc. Phys. Soc. 86, 1259.

D. R. Bates, 1947: Proc. Roy. Soc. A188, 350.

D. R. Bates and A. Damgaard, 1949: Phil. Trans. Roy. Soc. A242, 101.

G. D. Bell, M. H. Davis, R. B. King and P. M. Routly, 1958: Ap. J. 127, 775.

H. A. Bethe and E. E. Salpeter, 1957: Quantum Mechanics of One- and Two-Electron Atoms, Academic Press, New York.

L. Biermann and K. Lubeck, 1948: Z. Ap. 25, 325.

L. Biermann and E. Trefftz, 1949: Z. Ap. 26, 213.

A B. Bolotin and A. P. Yutsis, 1953: ZETF 24 (5), 527. OTP I, p. 271.

B. Brehm, W. Demtroder and O. Osberghaus, 1961: Z. Natwforsch. 16a, 843.

A. Burgess and M. J. Seaton, 1960: Mon. Nat. Roy. Astr. Soc. 120, 121.

A. Burgess, G. B. Field and R. W. Michie, 1960: Ap. J. 131, 529.

S. Chandrasekhar, 1944: Ap. J. 100, 176.

S. Chandrasekhar, 1945a: Ap. J. 102, 223.

S. Chandrasekhar, 1945b: Ap. J. 102, 395.

J. C. Y. Chen, 1964: J. Chem. Phys. 40, 615.

J. C. Y. Chen and A. Dalgarno, 1965: Proc. Phys. Soc. 85, 399.

C. D. H. Chisholm and U. Opik, 1964: Proc. Phys. Soc. 83, 541.

C. D. H. Chisholm and A. Dalgarno, 1966: Proc. Roy. Soc. (in press).

M. Cohen, 1961: Thesis (unpublished), Oxford University.

M. Cohen and A. Dalgarno, 1964: Proc. Roy. Soc. A280, 258.

M. Cohen and P. S. Kelly, 1965: Can. J. Phys. 43, 1867.

M. Cohen and A. Dalgarno, 1966: Proc. Roy. Soc. A. (to be published).

E. U. Condon and G. H. Shortley, 1935: The Theory of Atomic Spectra, Cambridge University Press.

C. H. Corliss and W. R. Bozman, 1962: NBS Monograph No. 53.

C. H. Corliss, 1962: J. Res. NBS 66A, 5.

C. A. Coulson, 1965: Q. J. Math. (Oxford) 16, 279.

R. J. S. Crossley and A. Dalgarno, 1965: Proc. Roy. Soc. A286, 510.

A. Dalgarno and J. T. Lewis, 1956: Proc. Phys. Soc. 69A, 285.

A. Dalgarno and N. Lynn, 1957: Proc. Phys. Soc. 70A, 802.

A. Dalgarno and A. E. Kingston, 1958: Proc. Phys. Soc. 72, 1053.

A. Dalgarno and A. E. Kingston, 1959: Proc. Phys. Soc. 73, 455.

A. Dalgarno and A. L. Stewart, 1960: Proc. Roy. Soc. A257, 534.

P. J. Dickermann and R. W. Deuel, 1964a: J.Quant.Spectr. Rad. Trans. 4, 807.

P. J. Dickermann and R. W. Deuel, 1964b: Rev. Sci. Instru. 35, 978.

A. Eberhagen, 1955: Z. Phys. 143, 392.

B. Edlen, 1964: Handbuch der Physik 27, 80.

U. Fano, 1961: Phys. Rev. 124, 1866.

E. W. Foster, 1964: Rpts. Prog. Phys. 27, 469.

C. Froese, 1963: Can. J. Phys. 41, 1895.

C. Froese, 1964: Ap. J. 140, 361.

C. Froese, 1965a: Ap. J. 141, 1206.

C. Froese, 1965b: Ap. J. 141, 1557.

R. H. Garstang, 1962: Atomic and Molecular Processes (ed., D. R. Bates), Academic Press, New York.

R. H. Garstang, 1962: Ann. D'Ap. 25, 109.

R. H. Garstang, 1964: J. Res. NBS 68A, 61.

W. R. S. Garton, W. H. Parkinson and E. M. Reeves, 1964: Ap. J. 140, 1269.

S. Geltman, 1962: Ap. J. 136, 935.

B. M. Glennon and W. L. Wiese, 1966: NBS Misc. Pub. No. 278.

E. A. Godfredsen, 1966: Ap. J. (in press).

L. Goldberg, E. A. Muller and L. H. Aller, 1960: Ap. J. Supp. 5, 1.

L. C. Green and N. E. Weber, 1950: Ap. J. 111, 582.

L. C. Green, N. E. Weber and E. Krawitz, 1951: Ap. J. 113, 690.

L. C. Green, M. N. Lewis, M. M. Mulder and J. W. Woll, 1954: Phys. Rev. 93, 757.

L. C. Green, P. P. Rush and C. D. Chandler, 1957: Ap. J. Supp. 3, 37.

L. C. Green, E. K. Kolchin and N. C. Johnson, 1965: Phys. Rev. 139A, 373.

L. C. Green, N. C. Johnson and E. K. Kolchin, 1966a: Ap. J. 144, 369.

L. C. Green, N. C. Johnson and E. K. Kolchin, 1966b: IAU Symposium No. 26 (ed., H. Hubenet).

H. R. Griem, 1964: Plasma Spectroscopy, McGraw-Hill, New York.

P. F. Gruzdev, 1962: Proceedings of 13th All-Union Conference on Spectroscopy, Leningrad, 1960: "Physical Problems in Spectroscopy," Moscow, p. 36 (Translation: J. L. Tech, Harvard College Observatory).

G. G. Hall, L. L. Jones and D. I. Rees, 1965: Proc. Roy. Soc. A283, 194.

F. S. Ham, 1955: Solid State Physics 1, 127.

D. R. Hartree, 1927: Proc. Camb. Phil. Soc. 24, 89.

D. R. Hartree, W. Hartree and B. Swirles, 1939: Phil. Trans. Roy. Soc. 238, 229.

D. R. Hartree, 1946: Rev. Mod. Phys. 11, 113.

D. R. Hartree, 1957: The Calculation of Atomic Structures, Wiley, New York.

R. Hefferlin and J. Gearhart, 1964: J.Quant. Spectr. Rad. Trans. 4, 9.

F. Herman and S. Skillmann, 1963: Atomic Structure Calculations, Prentice-Hall, Englewood Cliffs, N.J.

J. O. Hirschfelder, W. Byers Brown and S. T. Epstein, 1964: Advances in Quantum Chemistry 1, 255.

J. O. Hirschfelder and W. A. Sanders, 1965: J. Chem. Phys. 43, S204.

L. Houziaux and M. P. Sadoine, 1961: Bull. Soc. Roy. Sci. Liege 30, 287.

E. A. Hylleraas, 1945: Arch. Math. Naturial (Oslo) B48, 57.

A. V. Ivanova, 1963: Liet. Fiz. Rink. 3, 185.

B. S. Jeffreys, 1961: Quantum Theory I: Elements (ed., D. R. Bates) Academic Press, New York.

L. L. Jones, 1965: J. Chem. Phys. 43, S206.

H. P. Kelly, 1964: Phys. Rev. 136, B896.

P. S. Kelly, 1964a: Ap. J. 140, 1247.

P. S. Kelly, 1964b: J. Quant. Spectr. Rad. Trans. 4, 117.

R. B. King, 1963: J. Quant. Spectr. Rad. Trans. 3, 299.

S. R. LaPaglia and O. Sinawoglu, 1966: J. Chem. Phys. 44, 1888.

G. M. Lawrence, 1965: J. Quant. Spectr. Rad. Trans. 5, 359.

G. M. Lawrence, J. K. Link and R. B. King, 1965: Ap. J 141, 293.

G. M. Lawrence and B. D. Savage, 1966: Phys. Rev. 141, 67.

D. Layzer, 1959: Annals of Physics, N.Y. 8, 271.

D. Layzer, 1961: Mem. Soc. Roy. Sci. Liege 4, 179.

P. O. Lowdin, 1965: J. Chem. Phys. 43, S175.

B. V. Lvov, 1965: Opt. Spect. 19, 282.

W. C. Marlow, 1965: Lockheed Missiles and Space Corp. Report A034392.

F. F. Marmo, 1964: GCA Corporation Quarterly Progress Report No. 1, "Study of Lunar Atmosphere Detection and Monitoring Systems," NAS9-3445.

W. Marshall, 1961: Proc. Phys. Soc. 78, 113.

H. S. W. Massey and D. R. Bates, 1940: Ap. J. 91, 202.

D. F. Mayers and A. J. Hirsh, 1965: Aerospace Research Labs. Rpt. ARL65-62.

M. A. Mazing, 1961: Trudy Fiz. Inst. P.N. Lebedev 15, Part II. (Translation: Consultants Bureau, New York, 1962.)

W. F. Meggers, C. H. Corliss and B. F. Scribner, 1961: NBS Monograph No. 32.

H. Mendlowitz, 1966: Ap. J. 143, 573.

L. N. Mertz, 1966: J. Opt. Soc. Am. (to be published).

A. C. G. Mitchell and M. W. Zemansky, 1934: Resonance Radiation and Excited Atoms, Cambridge University Press.

C. E. Moore, 1949: Atomic Energy Levels, NBS Circular 467.

N. G. Morozova and G. P. Startsev, 1964: Opt. Spect. 17, 174.

N. G. Morozova and G. P. Startsev, 1965: Opt. Spect. 18, 505.

P. Morse, L. Young and E. Haurwitz, 1935: Phys. Rev. 48, 948.

P. Morse and H. Yilmaz, 1956: Tables for the Variational Determination of Atomic Wave Functions, Technology Press, MIT, Cambridge, Mass.

A. Mukherji and M. Karplus, 1963: J. Chem. Phys. 38, 44.

A. M. Naqvi, 1964: J. Quant. Spectr. Rad. Trans. 4, 597.

An. N. Nesmeyanov, 1961: Vapor Pressures of the Chemical Elements, Izd. ANSSSR.

H. N. Olsen, 1959: Phys. Fluids 2, 614.

H. N. Olsen, 1961: Phys. Rev. 124, 1703.

H. N. Olsen, 1963a: J. Quant. Spectr. Rad. Trans. 3, 59.

H. N. Olsen, 1963b: J. Quant. Spectr. Rad. Trans. 3, 305.

P. P. Ostroumenko and V. S. Rossikhin, 1965: Opt. Spect. 19, 365.

Yu. I. Ostrovskii and N. P. Penkin, 1961: Opt. Spect. 11, 1.

C. L. Pekeris, 1959: Phys. Rev. 115, 1216.

C. L. Pekeris, 1962: Phys. Rev. 126, 143.

N. P. Penkin and L. N. Shabanova, 1962: Opt. Spect. 12, 1.

N. P. Penkin and I. Yu. Yu. Slavenas, 1963a: Opt. Spect. 15, 3.

N. P. Penkin and I. Yu. Yu. Slavenas, 1963b: Opt. Spect. 15, 83.

N. P. Penkin, 1964: J. Quant. Spectr. Trans.4, 41. (Translation by J.L. Tech, issued by Smithsonian Astrophys. Observatory, Cambridge, Mass.)

M. I. Petrashen and I. V. Abarenkov, 1954: Vest. Leningrad Univ. 5, 141. OTP II, p. 116.

H. Pfennig, R. Steele and E. Trefftz, 1965: J. Quant. Spectr. Rad. Trans. 5,335.

D. Pines, 1955: Solid State Physics 1, 368.

G. W. Pratt, 1956: Phys. Rev. 102, 1303.

P. D. Robinson, 1965: Proc. Roy. Soc. A283, 229.

C. C. J. Roothaan and P. S. Bagus, 1963: Methods Comp. Phys. 2, 47.

G. O. Sauermann and E. D. Schultz, 1965: GCA Technical Note, "Resonant Scattering Parameters for the Elements."

B. D. Savage and G. M. Lawrence, 1966: Ap. J. (submitted).

B. Schiff and C. L. Pekeris, 1964: Phys. Rev. 134, A638.

M. J. Seaton, 1958: Mon. Nat. Roy. Astr. Soc. 118, 504.

G. W. Series and K. Willis, 1958: Proc. Phys. Soc. 71A, 274.

B. W. Shore, 1965: Ap. J. 142, 94.

A. M. Shukhtin, 1965: Opt. Spect. 19, 457.

J. C. Slater, 1960: Quantum Theory of Atomic Structure, McGraw-Hill, New York.

S. J. Smith and D. S. Burch, 1959: Phys. Rev. 116, 1125.

A. L. Stewart, 1963: Adv. Phys. 12, 299.

J. C. Stewart and M. Rotenberg, 1965: JILA Report No. 48, Boulder, Colorado.

E. Trefftz, 1949: Z. Ap. 26, 240.

E. Trefftz, 1950: Z. Ap. 28, 67.

E. Trefftz, 1951: Z. Ap. 29, 287.

E. Trefftz, A. Schluter, K. H. Dettmar and K. Jorgens, 1957: Z. Ap. 44, 1.

A. Tubis, 1956: Phys. Rev. 102, 1049.

L. A. Vainshtein and B. M. Yavorskii, 1952: Doklady ANSSSR 87(6), 919. OTP I, p. 267.

L. A. Vainshtein, 1961: Trudy Fiz. Inst. P. N. Lebedev 15, 1. (Translation: Consultants Bureau, New York, 1962.)

J. G. Valatin, 1961: Phys. Rev. 122, 1012.

C. M. Varsavsky, 1958: Thesis (unpublished), Harvard University.

C. M. Varsavsky, 1961: Ap. J. Supp. 6, 75.

M. G. Veselov, 1949: ZETF 19, 959.

M. G. Veselov, 1953: Vestnik Leningradskogo Universiteta 8, 181. OTP I, p. 280.

S. I. Vetchinkin, 1963: Liet. Fiz. Rink 3, 107.

Ya. I. Vizbaraite, A. I. Kantserevichyus and A. P. Yustis, 1956: Opt. Spect. 1, 9. OTP I, p. 314.

I. Waller, 1927: Z. Phys. 38, 635.

B. Warner, 1964: Thesis, London University.

A. W. Weiss and J. B. Martin, 1963: Phys. Rev. 132, 2118.

E. B. Wilson, 1965: J. Chem. Phys. 43, S172

W. H. Wurster, 1963: J. Quant. Spectr. Rad. Trans. 3, 355.

A. P. Yutsis, Ya. I. Vizbaraite, T. D. Strotskite and A. A. Bandzaitis, 1962: Opt. Spect. 12, 83.

A. Zwaan, 1929: Thesis, Utrecht.

ACKNOWLEDGMENT

Sincere appreciation is expressed to the staff of the Sacramento Peak Observatory and its Director, Dr. J.W. Evans, for their overall cooperation in the conduct of the field experimental program reported herein. Specific acknowledgment is accorded the following Observatory personnel for their active participation in the field measurement effort: F.L. Warford, L.B. Gilliam, H. Mauter, and A.G. Hullen.